Probing quantum devices with radio-frequency reflectometry

Florian Vigneau,[1] Federico Fedele,[1] Anasua Chatterjee,[2] David Reilly,[3,4] Ferdinand Kuemmeth,[2] M. Fernando Gonzalez-Zalba,[5,a)] Edward Laird,[6,b)] and Natalia Ares[1,c)]
[1]*University of Oxford, Department of Materials, 16 Parks Road, Oxford OX1 3PH, UK*
[2]*Center for Quantum Devices, Niels Bohr Institute, University of Copenhagen, 2100 Copenhagen, Denmark*
[3]*ARC Centre of Excellence for Engineered Quantum Systems, School of Physics, The University of Sydney, NSW 2006, Australia*
[4]*Microsoft Quantum Sydney, The University of Sydney, Sydney, NSW 2006, Australia*
[5]*Quantum Motion Technologies, Windsor House, Cornwall Road, Harrogate, HG1 2PW, United Kingdom*
[6]*Department of Physics, University of Lancaster, Lancaster, LA1 4YB, United Kingdom*

(Dated: 2 November 2022)

Many important phenomena in quantum devices are dynamic, meaning that they cannot be studied using time-averaged measurements alone. Experiments that measure such transient effects are collectively known as fast readout. One of the most useful techniques in fast electrical readout is radio-frequency reflectometry, which can measure changes in impedance (both resistive and reactive) even when their duration is extremely short, down to a microsecond or less. Examples of reflectometry experiments, some of which have been realised and others so far only proposed, include projective measurements of qubits and Majorana devices for quantum computing, real-time measurements of mechanical motion and detection of non-equilibrium temperature fluctuations. However, all of these experiments must overcome the central challenge of fast readout: the large mismatch between the typical impedance of quantum devices (set by the resistance quantum) and of transmission lines (set by the impedance of free space). Here, we review the physical principles of radio-frequency reflectometry and its close cousins, measurements of radio-frequency transmission and emission. We explain how to optimise the speed and sensitivity of a radio-frequency measurement, and how to incorporate new tools such as superconducting circuit elements and quantum-limited amplifiers into advanced radio-frequency experiments. Our aim is three-fold: to introduce the readers to the technique, to review the advances to date and to motivate new experiments in fast quantum device dynamics. Our intended audience includes experimentalists in the field of quantum electronics who want to implement radio-frequency experiments or improve them, together with physicists in related fields who want to understand how the most important radio-frequency measurements work.

CONTENTS

a)fernando@quantummotion.tech
b)e.a.laird@lancaster.ac.uk
c)natalia.ares@eng.ox.ac.uk

I. INTRODUCTION AND MOTIVATION

A. Why use rf measurements?

The bandwidth of standard electrical measurement setups is typically limited by the RC low-pass filter formed by the resistance of the sample, the input impedance of the amplifier and the capacitance of the electrical cables that connect cryogenic devices to the measurement instruments at room temperature. Quantum devices usually have resistances of the order of the quantum of resistance $h/e^2 \approx 25.8$ kΩ and the capacitance of the cables is in the range $C_{\text{line}} = 0.1 - 1$ nF which bring the cut-off frequency to no more than few kilohertz.

An important example of this problem is the single-electron transistor (SET). SET charge sensors[1,2] are the most sensitive electrometers used to measure the charge occupation of quantum dots (QDs) by monitoring the change of resistance of a closely positioned SET. In principle[3], their bandwidth could exceed 10 GHz, intrinsically limited by the RC filtering due to the resistance of the two tunnel junctions in series ($> 2h/e^2$) and the typical capacitance of few femtofarads between the SET's tunnel junctions. However, in practice, the bandwidth is limited to few kilohertz because of the high capacitance of the cabling that connects the output of the device to room temperature electronics (Fig. 1(a)).

There have been some attempts[3,4] to overcome this obstacle by introducing cryogenic amplifiers close to the device. This has the effect of reducing the capacitance of the cable but also produces a substantial amount of heat near the device. It is difficult to reduce the amplifier resistance, R_{AMP}, much below the SET resistance since it would create a voltage divider for the signal. Another approach is to replace the voltage amplifier by a current-to-voltage converter, with a lower input impedance, that measures the current at the output of the SET[5], but the improvement is modest.

In 1998 Schoelkopf *et al.* introduced the radio-frequency SET (rf-SET)[6] which can measure the charge occupation of quantum dots with a bandwidth exceeding 100 MHz. The solution was to place the SET at the end of a transmission line (Fig. 1(b)) while illuminating the device with an rf signal whose reflected phase and amplitude depend on the impedance of the SET. The high resistance of the SET is converted to the $Z_0 = 50\ \Omega$ characteristic impedance of the line by a matching network combining the impedances of an inductor L_{C} and a capacitor C_{P}, in its simplest implementation. Since all the components in the amplification chain, including the amplifier input impedance, are now matched to Z_0 the bandwidth of the measurement is greatly enhanced.

Since then, rf techniques for QDs have flourished, motivated in particular by the emergence of quantum computation using the spin of charged particles confined to real or artificial atoms (QDs) to encode qubits[8]. Practical quantum computation requires error correction schemes that involve fast high-fidelity single-shot readout of qubits[9], much faster than their coherence time. Such sensitive and fast readout could be provided by the rf-SET (or related readout devices such as the rf quantum point contact (rf-QPC)), or dispersive readout.

Radio-frequency techniques are becoming increasingly popular to study other kinds of quantum devices and phenomena. In particular, they have been employed for measuring low-dimensional systems, nanomechanical resonators, superconducting quantum interference devices (SQUIDs), and Majorana devices, and even to perform fast thermometry. Owing to its high bandwidth, rf readout enables measurements of the time evolution of rapid physical effects. In some cases, as we shall see, the input signal induces novel non-equilibrium phenomena, allowing their study.

B. Organisation of the review

In Section II, we introduce the fundamental concepts essential to understand rf measurements and the subsequent sections of this review. This section is particularly important for readers who are new to high-frequency electronics. We present the basic constituents of rf setups and the principles of propagation of high frequency electronic signals along transmission lines, of impedance matching, of signal composition and demodulation.

In Sections III and IV, we present dissipative and reactive readout of quantum devices by focusing on the representative example of charge sensing in QDs. In the case of dissipative readout, the change of the sample resistance due to changes in the electrostatic environment modifies the amplitude of the rf signal. In the case of reactive readout, the phase of the rf signal changes due to variations of the device capacitance or inductance. We describe the examples of charge sensing in QDs as illustration. We explain the working principle of the rf-SET, the rf-QPC and dispersive readout. For each case, we give an overview of the state-of-the-art.

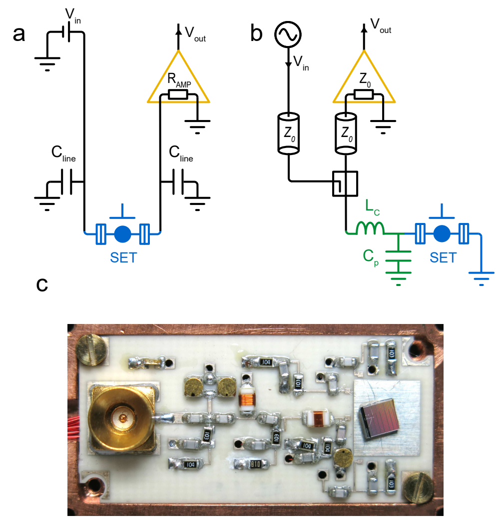

FIG. 1. (a) Conventional dc measurement of a SET. The SET is biased with a dc voltage V_{in} applied to the source electrode. A second line carries the current to the amplifier, which outputs a voltage V_{out}. (b) Radio-frequency measurement of the SET embedded in a combination of impedances L_{C} and C_{P}. The SET is illuminated by an rf ac voltage V_{in} injected via a transmission line of characteristic impedance Z_0. The reflected signal is routed by a directional coupler and a second transmission line to the amplifiers, which outputs V_{out}. (c) Picture of a sample board for radiofrequency measurements mounted on a copper enclosure, reproduced from[7], with the permission of AIP Publishing. The PCB hosts a high frequency SMP connector on the left hand side, a horizontally-positioned wirewound ceramic inductor (part of the matching network), three varicap diodes (gold-coloured circular components) for frequency and matching tuning, RC filters on every bias line and a vertically-positioned shunt inductor to provide attenuation of modulation frequencies on the matching varicaps. Finally on the right hand side, a sample is bonded to the matching network.

Technological developments have greatly improved the sensitivity and bandwidth of high-frequency measurements. The engineering of rf cavities is the subject of Section V. Variable capacitors, for example, allow *in-situ* tuning of the cavity resonant frequency in order to optimize impedance matching to the device to be probed. Superconducting circuit elements and optimized circuit topologies can improve the cavity quality factor of the resonator. Identifying and reducing sources of noise is key to the readout of weak signals. Low-noise amplifiers, including superconducting amplifiers that reach or exceed the standard quantum limit, will be described in Section VI. Different approaches to scale up measurement setups to read multiple quantum devices are presented in Section VII.

Finally, we focus on the many different quantum phenomena that can be studied using fast readout, and on how they are exploited in quantum technologies and other condensed matter physics experiments. In Section VIII, we explain in particular the stimulating application of the fast readout of spin qubits, imperative for fault tolerant quantum computing. Other applications are shown in Section IX. For example, special symmetries in the effective circuit could allow noise-protected superconducting qubits (Section IX A). An interesting adaptation allows probing Majorana modes in nanowire devices and could be the basis for topological qubit readout (Section IX B). The measurement of noise (Section IX C) can reveal fundamental properties of a device such as the charge of the carriers and its temperature. High-frequency measurements of nanomechanical resonators (Section IX D) have proved key for studying fast dynamics and are promising for the generation of quantum states. Rf thermometry (Section IX E) brings a solution for measuring subkelvin temperature and with a speed that could enable to detect out-of-equilibrium phenomena. Rf measurements can also reveal information about the environment of a quantum device (Section IX F). Finally, superconducting quantum interference devices (SQUIDs) allow sensitive magnetic field sensing (Section IX G). We conclude the review with perspectives on future developments.

We also note the boundaries of this review. Here we focus the regime where the photon energy of the rf signal is much smaller than the quantum level separation, such that resonant excitations do not occur and the system can be described using a semiclassical approach: a classical electric field coupled to a quantum system. The situation when these two energies are comparable and quantum mechanical interactions may occur between the two systems is described in the theory of quantum electrodynamics[10].

II. BASICS OF HIGH-FREQUENCY MEASUREMENTS

This section is a high-level overview of high-frequency electronic measurements, covering the main elements of the circuit to the final demodulated signal. To understand how these measurements work, we need to know what the main constituents of an rf setup are (Section II A); how a signal voltage propagates along a transmission line (Section II B); how it is changed when it scatters off a load impedance (Section II C); and how information about the load can be extracted from the signal (Section II D). From these, the reader should gain a self-contained understanding of how a high-frequency measurement works. The later sections of this review provide more comprehensive explanations of how these principles are implemented in experiments.

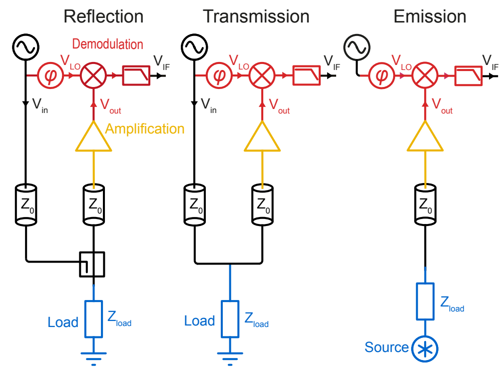

FIG. 2. Reflection, transmission and emission measurement setups. In the first two panels, the input signal V_{in} is generated by an rf source and travels along transmission lines of characteristic impedance Z_0. After illuminating the load the returned signal is amplified into V_{out} and homodyne demodulated into V_{IF}. In the third panel, the source emits a signal by itself that is demodulated using an external signal.

A. High-frequency measurement setups: an overview

Circuit diagrams for the three main types of high-frequency measurement are shown in Fig. 2. In a reflection or transmission measurement (as shown in the first two panels), the aim is to detect changes in the impedance of the device under test by converting them to a voltage. The device, together with the tank circuit in which it is usually embedded, presents a total impedance Z_{load}, so called because it acts as a load on the transmission line. When the device impedance changes, Z_{load} changes. To measure Z_{load}, it is illuminated by injecting a carrier tone $V_{\text{in}}(t)$. The carrier propagates along a transmission line towards the load and is reflected off it (in reflection configuration) or transmitted through or past it (in transmission configuration). The signal propagating away from the load differs from $V_{\text{in}}(t)$ in a way that depends on Z_{load} and therefore on the device impedance.

The outgoing signal is then amplified to boost it well above the noise of subsequent electronics used for analysis. Finally, it is usually demodulated to shift it away from the carrier frequency and towards a lower frequency, which is usually more convenient to work with. This is done by multiplying it with a demodulation tone $V_{\text{LO}}(t)$ and low-pass filtering the product, as explained in Section II D. Often $V_{\text{LO}}(t)$ is derived from the original carrier, as in Fig. 2. The output $V_{\text{IF}}(t)$ of the demodulation circuit carries the required information about the device impedance. This is the signal that is recorded.

The third type of high-frequency measurement does not inject a carrier tone at all. Instead, it treats the device as a voltage source whose emission must be measured. The circuit used in this kind of measurement (third panel of Fig. 2) therefore omits the injection path.

B. Wave propagation along transmission lines, the characteristic impedance Z_0, and why it is important

To couple a voltage source to the load being measured, as in Fig. 3(a), we must provide paths for both signal and ground. This is done using a coaxial cable, or sometimes using coplanar waveguides. The general term for any such connection is a transmission line. The signal propagates as a voltage difference between the inner (or signal) conductor and the outer (or ground).

1. Wave propagation along a transmission line

In dc electronics, two points in a circuit connected by a zero-resistance path will be at the same voltage. However, this is not generally true at high frequency. The reason is that the connecting cable has an inductance which presents a high-frequency impedance between its two ends. Likewise the capacitance between the inner conductor and ground means that the current need not be the same everywhere along the cable.

To describe signal propagation, we must therefore allow the signal voltage $V(x,t)$ and current $I(x,t)$ to depend on location x along the cable as well as on time t. To see how these are related, suppose we have a cable of inductance L_ℓ and capacitance C_ℓ per unit length. We imagine slicing the cable into short segments, each approximated by a single inductor and capacitor as in Fig. 3(b). This is a lumped-element transmission-line model of the cable. By analysing the voltage and current at each node[11], a pair of coupled equations (the telegraph equations) can be derived:

$$\frac{\partial V}{\partial x} = -L_\ell \frac{\partial I}{\partial t} \tag{1}$$

$$\frac{\partial I}{\partial x} = -C_\ell \frac{\partial V}{\partial t}. \tag{2}$$

Their solution is:

$$V(x,t) = \quad V_+\left(t - \frac{x}{c'}\right) + V_-\left(t + \frac{x}{c'}\right) \tag{3}$$

$$I(x,t) = \frac{1}{Z_0}\left[V_+\left(t - \frac{x}{c'}\right) - V_-\left(t + \frac{x}{c'}\right)\right] \tag{4}$$

where $c' = 1/\sqrt{L_\ell C_\ell}$ is the phase speed of transmission line. These solutions correspond to waves propagating in the positive direction (described by $V_+\left(t - \frac{x}{c'}\right)$) and the negative direction (described by $V_-\left(t + \frac{x}{c'}\right)$).

For a wave propagating in a single direction, i.e. either the V_+ or the V_- component, there is a fixed ratio between the signal voltage current and the signal current. This ratio

$$Z_0 \equiv \sqrt{\frac{L_\ell}{C_\ell}} \tag{5}$$

is the characteristic impedance of the line. It is the impedance that a semi-infinite length of line would present at its end, if its internal resistance (which was ignored in the approximation of Fig. 3) could be neglected.

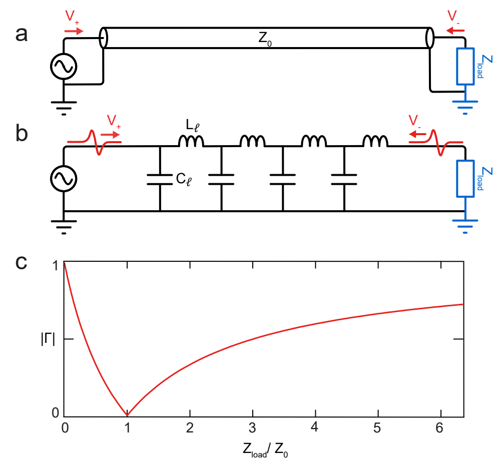

FIG. 3. (a) Transmission line with characteristic impedance Z_0 linking an rf voltage generator to a load impedance. The signal V_+ is output by the generator and transmitted through the line. When it reaches the load, a portion of this signal V_- is reflected back. (b) Lumped-element equivalent of the same circuit. The line is represented by short segments of length $\Delta\ell$, each with inductance $L_\ell\Delta\ell$ and capacitance $C_\ell\Delta\ell$. (c) Magnitude of the reflection coefficient $|\Gamma|$ (Eq. 10) as function of the ratio Z_{load}/Z_0.

2. Scattering at an impedance mismatch

A transmission line's characteristic impedance becomes important when it is connected to a load with a different impedance. The simplest example is a two-terminal device, such as a resistor, with impedance Z_{load} (Fig. 3(a-b)). This imposes the boundary condition at the end of the line:

$$\frac{V(x,\omega)}{I(x,\omega)} = Z_{\mathrm{load}}(\omega), \tag{6}$$

where $V(x,\omega)$ and $I(x,\omega)$ are respectively the time Fourier transforms of $V(x,t)$ and $I(x,t)$ and $Z_{\mathrm{load}}(\omega)$ is the load impedance, which in general depends on the angular frequency ω.

Unless $Z_{\mathrm{load}} = Z_0$, the V_+ component of Eqs. (3-4) cannot satisfy Eq. (6) by itself. This means that if there is a mismatch between the impedances of the line and the load, part of the signal must be reflected back. The amount of reflection can be calculated by defining $x = 0$ to be the end of the line, and then taking the time Fourier transforms of Eqs. (3-4) to give[11]:

$$V(0,\omega) = V_+(\omega) + V_-(\omega) \tag{7}$$

$$I(0,\omega) = \frac{V_+(\omega) - V_-(\omega)}{Z_0}. \tag{8}$$

Substituting into Eq. (6) then gives the reflection coefficient

$\Gamma(\omega)$ for the component of the incident signal at angular frequency ω:

$$\Gamma(\omega) \equiv \frac{V_-(0,\omega)}{V_+(0,\omega)} \tag{9}$$

$$= \frac{Z_{\text{load}}(\omega) - Z_0}{Z_{\text{load}}(\omega) + Z_0}. \tag{10}$$

Figure 3(c) plots Γ for a purely resistive Z_{load}. Similar equations hold for the scattered amplitude in a transmission circuit (see supplementary Section S1).

In one respect, Eq. (10) is good news for measuring an unknown impedance; all we need to do is connect it to a transmission line and see how much power it reflects. However, Eq. (10) and Fig. 3(c) also tell us that if $|Z_{\text{load}}| \gg Z_0$, the reflection barely depends on Z_{load}. Unfortunately, this is almost always the situation when measuring a quantum device. This is because the typical resistance of a quantum device, such as an SET, is set by the resistance quantum, i.e.

$$Z_{\text{load}} \sim \frac{h}{e^2} \approx 25.8\ \text{k}\Omega. \tag{11}$$

However, the typical impedance of a transmission line is of the order of magnitude of the impedance of free space η_0, i.e.

$$Z_0 \sim \eta_0 \equiv \sqrt{\frac{\mu_0}{\varepsilon_0}} \approx 377\ \Omega. \tag{12}$$

For example, a cylindrical coaxial cable has

$$Z_0 = \frac{\eta_0}{2\pi}\sqrt{\frac{\mu_r}{\varepsilon_r}}\ \ln\frac{b}{a}, \tag{13}$$

where μ_r and ε_r are the relativity permeability and permittivity of the coaxial insulation and a and b are the diameters of the inner and outer conductor respectively. For other geometries, similar equations apply[11]. In fact most commercial coaxial cables, and therefore electronics designed to interface with them, use the standard value

$$Z_0 = 50\ \Omega. \tag{14}$$

The mismatch between Eqs. (11) and (12) is the fundamental reason why high-speed measurements of quantum devices are so difficult. One tempting circumvention is to design a transmission line with $Z_0 \approx h/e^2$. Unfortunately, this approach seems doomed to failure[12]. Equation (13) shows that we would need coaxial cable with a diameter ratio of $b/a \approx 10^{187}$, even using vacuum dielectric! The key advance that created the field of radio-refrequency reflectometry for quantum devices was to interpose an impedance transformer between the load and transmission line[6]. This is the topic of Section III.

C. Using an electrical resonator as the load impedance

For reasons that will be explained in Section III, the most useful load is usually an electrical resonator. Near its resonance frequency, such a resonator is well approximated by an

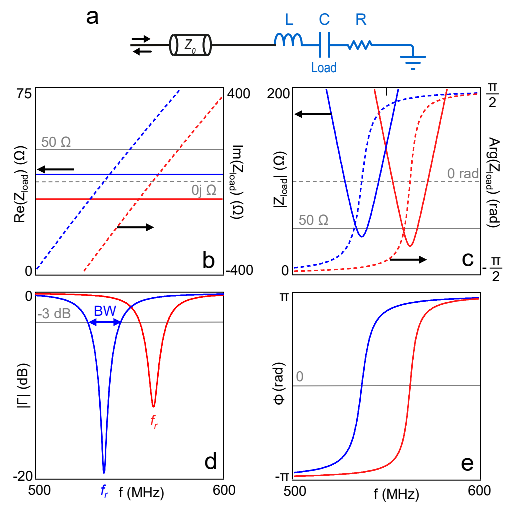

FIG. 4. (a) Schematic of a transmission line connected to a LCR load. (b) Simulation of the real (solid lines) and imaginary part (dashed lines) of Z_{load} as function of the frequency f for two slightly different LCR loads. Blue: $R = 40\ \Omega$, $L = 800$ nH, $C = 0.11$ pF; red: $R = 30\ \Omega$, $L = 800$ nH, $C = 0.1$ pF. (c) Corresponding modulus (solid lines) and phase (dashed lines) of Z_{load}. (d) Corresponding reflection amplitude $|\Gamma|$, with $Z_0 = 50\ \Omega$. The minimum of each dip marks the resonance frequency f_r. The bandwidth B_f lies approximately -3 dB from the top. (e) Corresponding reflection phase.

equivalent LCR circuit with an inductance L, a capacitance C and a resistance R in series (Fig. 4(a)). The equivalent complex impedance is:

$$Z_{\text{load}}(\omega) = j\omega L + \frac{1}{j\omega C} + R \tag{15}$$

where $j = \sqrt{-1}$. In this subsection, we describe the important properties of such a circuit and their effect on the reflection coefficent $\Gamma(f)$, where as usual the frequency is $f = \omega/2\pi$.

1. *Resonance frequency*

Figure 4 shows how the complex impedance Z_{load} (Eq. (15)) and the reflection spectrum depend on frequency. Figure 4(b) plots the real and imaginary parts of $Z_{\text{load}}(f)$, calculated for two different combinations of L, C, and R. Figure 4(c) shows the same quantities plotted as amplitude and phase. The resonance frequency is where $\text{Im}(Z_{\text{load}})$ passes through zero, or equivalently where $\arg(Z_{\text{load}}) = 0$. From Eq. (15), this frequency is

$$f_r = \frac{1}{2\pi\sqrt{LC}}. \tag{16}$$

The resonance also appears clearly in the reflection coefficient $\Gamma(f)$. It leads to a dip in the amplitude $|\Gamma|$, here expressed in decibels ($|\Gamma|_{\mathrm{dB}} = 20\log_{10}(|\Gamma|_{\mathrm{lin}})$) (Fig. 4(d)) and a steep change in the reflection phase spectrum $\phi = \arg(\Gamma)$ (Fig. 4(e)). Clearly this is a favourable frequency at which to illuminate the resonator, since a small change in circuit parameters leads to a large change in the amplitude or phase of the reflected signal. A change of R changes the depth of the dip of the $|\Gamma(f)|$ while a change of C or L changes f_{r} and moves $|\Gamma(f)|$ and $\phi(f)$ horizontally. These two cases are explained in detail in Section III and IV.

2. *Resonator quality factor and bandwidth*

How fast does the reflected signal respond to a change in circuit parameters? This is an important question, because it determines whether a transient change can be followed using reflectometry. The answer is that the reflection will track the circuit parameters provided the rate at which they change is slower than the resonator's bandwidth B_f[13]. The resonance, having an inverse Lorentzian shape, has bandwidth corresponding to the full width at half maximum (FWHM) of the reflected *power*[14]. This approximately corresponds to -3 dB from the top if it is plotted in logarithmic units and the dip is deep (Fig. 4(d)). This bandwidth is determined by the rate at which energy is lost from the resonator, and includes both internal losses (i.e. dissipation) and external losses (i.e. radiation to the transmission line).

Both channels are conveniently described by an associated quality factor, defined in the conventional way as the inverse of the fraction of energy lost per radian of oscillation. For the circuit of Fig. 4(a), the internal and external quality factors are respectively:

$$Q_{\mathrm{int}} = \frac{1}{R}\sqrt{\frac{L}{C}} = \frac{2\pi f_{\mathrm{r}} L}{R} \tag{17}$$

$$Q_{\mathrm{ext}} = \frac{1}{Z_0}\sqrt{\frac{L}{C}} = \frac{2\pi f_{\mathrm{r}} L}{Z_0}. \tag{18}$$

The loaded (or total) quality factor describes the combination of both mechanisms and is

$$Q_{\mathrm{r}} = \left(Q_{\mathrm{int}}^{-1} + Q_{\mathrm{ext}}^{-1}\right)^{-1} \tag{19}$$

$$= \frac{1}{R+Z_0}\sqrt{\frac{L}{C}}. \tag{20}$$

In terms of Q_{r}, the bandwidth is

$$B_f = \frac{f_{\mathrm{r}}}{Q_{\mathrm{r}}} \tag{21}$$

$$= \frac{R+Z_0}{2\pi L}. \tag{22}$$

The quality factor, and hence the bandwidth, is dominated by whichever loss channel is stronger.

As Fig. 4 suggests, designing resonators for fast readout involves a trade-off. A large Q_{r} is desirable to have a sharp resonance and therefore maximise the sensitivity changing circuit parameters. However, Eq. (22) shows that this limits the measurement bandwidth. This tension between sensitivity and speed is quantified by the Bode-Fano criterion, which states the optimum combination that can be achieved with resonators incorporating particular device impedances[11].

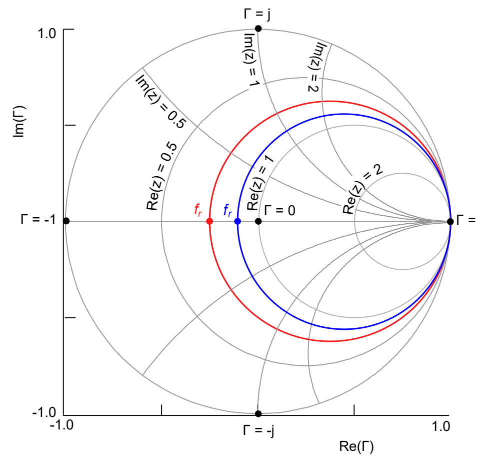

FIG. 5. Smith chart representation of the same curves as in Fig. 4. The grey lines represent particular value of the impedance ratio $z = Z_{\mathrm{load}}/Z_0$. Both curves are in the overcoupled regime since they intercept the horizontal line to the left of the point $\Gamma = 0$.

3. *Matching and coupling*

The coupling constant

$$\beta = \frac{Q_{\mathrm{int}}}{Q_{\mathrm{ext}}} = \frac{Z_0}{R} \tag{23}$$

quantifies the coupling of the load to the line and classifies which part of the circuit dominates the losses. Critical coupling occurs when $\beta = 1$, meaning that equal power is dissipated in the load and towards the line. Usually circuit parameters are chosen to operate near this point because it maximises power transfer between the load and the measurement circuit. The regime where $\beta < 1$, so that internal losses dominate (i.e. $Q_{\mathrm{int}} < Q_{\mathrm{ext}}$ and $R > Z_0$ for an LCR circuit), is called *undercoupled*. The opposite regime $\beta > 1$, illustrated in Fig. 5, is called *overcoupled*.

A useful way to show the reflection from a resonator and analyse the matching is by using a Smith chart[11]. This is a plot of the reflection coefficient Γ in the complex plane. A graph of Γ as a function of frequency, as shown over two panels in Fig. 4(d-e), appears as a single curve on the Smith chart (Fig. 5). The closer this curve passes to the centre of the chart, i.e. the point $\Gamma = 0$, the better the impedance matching. It can easily be measured using a vector network analyser.

Because Eq. (10) imposes a one-to-one mapping between Γ and Z_{load}, each point on the Smith chart also represents a specific value of Z_{load}. The gridlines of Z_{load}, i.e. contours of constant $\mathrm{Re}(Z_{\mathrm{load}})$ and $\mathrm{Im}(Z_{\mathrm{load}})$, appear as circles on the Smith chart. In Fig. 5, these gridlines are plotted in terms of the ratio $z = Z_{\mathrm{load}}/Z_0$. The Smith chart allows the effect of a change in Z_{load} to be seen graphically. For example, increasing R moves the horizontal intercept of the $\Gamma(\omega)$ curve to the right. When the intercept lies to the right of the point $\Gamma = 0$, the circuit is undercoupled while when it lies to the left, the circuit is overcoupled.

D. Introduction to demodulation

We explain here how the information carried by a signal $V(t)$ about the variation of Z_{load} is contained in two quadrature components and introduce the technique of demodulation to extract them.

1. Representing a signal in terms of its quadratures

A periodic signal $V(t)$ of frequency $f = \omega/2\pi$ can be mathematically expressed using two quadrature components. One common quadrature representation is composed of the amplitude R and phase φ:

$$V(t) = V_{\mathrm{R}}\cos(\omega t + \varphi) \tag{24}$$

We can rewrite $V(t)$ as:

$$V(t) = V_{\mathrm{R}}\cos(\varphi)\cos(\omega t) - V_{\mathrm{R}}\sin(\varphi)\sin(\omega t) \tag{25}$$
$$V(t) = V_{\mathrm{I}}\cos(\omega t) - V_{\mathrm{Q}}\sin(\omega t) \tag{26}$$

where we define the quadratures V_{I} and V_{Q} as:

$$V_{\mathrm{I}} = V_{\mathrm{R}}\cos(\varphi) \tag{27}$$
$$V_{\mathrm{Q}} = V_{\mathrm{R}}\sin(\varphi) \tag{28}$$

V_{I} and V_{Q} are also sometimes labelled "X" and "Y" or the "in-phase" and "out-of-phase" components. They correspond to two signals shifted in phase by $\pi/2$. The "IQ" quadrature representation is very useful to generate or analyse signals. The relation between (V_{I},V_{Q}) and (V_{R},φ) is

$$V_{\mathrm{R}} = \sqrt{V_{\mathrm{I}}^2 + V_{\mathrm{Q}}^2} \tag{29}$$

$$\varphi = \arctan\left(\frac{V_{\mathrm{Q}}}{V_{\mathrm{I}}}\right) \tag{30}$$

In Fig. **??**(a) the simulated signal $V(t)$ changes phase and amplitude in the middle of the horizontal axis which give two points in the IQ plane (Fig. 6(b)). This change could be due to a switch between two states of the load impedance Z_{load} with different reflection coefficients Γ.

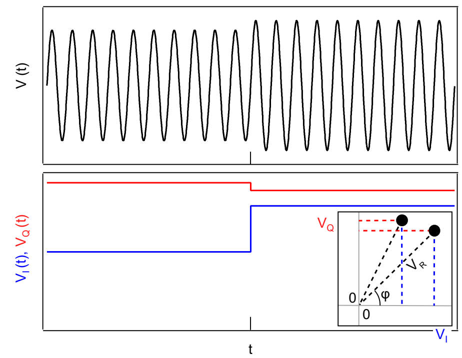

FIG. 6. Top: signal $V(t)$ for a device switching between two states. $V(t)$ changes phase and amplitude in the middle of the horizontal axis representing, for instance, a switch between two states of the load impedance Z_{load} with different reflection coefficients Γ. Bottom: $V(t)$ decomposed in V_{I} and V_{Q} quadratures. Inset: representation of the two states in the IQ plane.

2. Demodulation

We have just seen that the useful information carried by $V(t)$ is embedded in the quadrature components of the signal. A direct measurement of $V(t)$ is complex and inefficient since it would require high-rate acquisition of a huge number of points. A more efficient approach is to demodulate $V(t)$ to an intermediate frequency signal $V_{\mathrm{IF}}(t)$ that has a lower frequency but contains the information in the quadrature components V_{I} and V_{Q}.

To demodulate $V(t) = V_{\mathrm{I}}\cos(\omega t) - V_{\mathrm{Q}}\sin(\omega t)$ we need a mixer and a low pass filter. By mixing $V(t)$ with a demodulating signal $V_{\mathrm{LO}}(t) = \cos(\omega t)$ of the same frequency and phase we obtain the product

$$V_{\mathrm{IF}}(t) = V_{\mathrm{out}}(t)\cdot V_{\mathrm{LO}}(t), \tag{31}$$

which decomposes as

$$V_{\mathrm{I}}\cos(\omega t)\cdot\cos(\omega t) = \frac{V_{\mathrm{I}}}{2} + \frac{V_{\mathrm{I}}}{2}\cos(2\omega t) \tag{32}$$

$$-V_{\mathrm{Q}}\sin(\omega t)\cdot\cos(\omega t) = 0 - \frac{V_{\mathrm{Q}}}{2}\sin(2\omega t). \tag{33}$$

This product gives a low-frequency signal proportional to the V_{I} quadrature ($V_{\mathrm{I}}/2$). The 2ω component of the signal is removed by the low-pass filter. We obtain the V_{Q} quadrature by following the same process using a phase-shifted local oscillator $V_{\mathrm{LO}}(t) = -\sin(\omega t)$:

$$V_{\mathrm{I}}\cos(\omega t)\cdot(-\sin(\omega t)) = 0 - \frac{V_{\mathrm{I}}}{2}\sin(2\omega t) \tag{34}$$

$$-V_{\mathrm{Q}}\sin(\omega t)\cdot(-\sin(\omega t)) = \frac{V_{\mathrm{Q}}}{2} - \frac{V_{\mathrm{Q}}}{2}\cos(2\omega t) \tag{35}$$

If V and V_{LO} are separated by a phase difference φ the demodulated signal is composed of both quadrature components:

$$V_{\mathrm{I}}\cos(\omega t)\cdot\cos(\omega t+\varphi)\rightarrow\frac{V_{\mathrm{I}}}{2}\cos(\varphi) \tag{36}$$

$$-V_{\mathrm{Q}}\sin(\omega t)\cdot\cos(\omega t+\varphi)\rightarrow-\frac{V_{\mathrm{Q}}}{2}\sin(\varphi). \tag{37}$$

We have removed the 2ω contribution from these two expressions.

If $V(t)$ and $V_{\mathrm{LO}}(t)$ are not at the same frequency but $V_{\mathrm{LO}}(t)=\cos(\omega_{\mathrm{LO}}t)$, the demodulated signal is composed of two angular frequencies $\omega_{+}=\omega+\omega_{\mathrm{LO}}$ and $\omega_{-}=\omega-\omega_{\mathrm{LO}}$:

$$V_{\mathrm{I}}\cos(\omega t)\cos(\omega_{\mathrm{LO}}t)=\frac{V_{\mathrm{I}}}{2}\left[\cos(\omega_{-}t)+\cos(\omega_{+}t)\right] \tag{38}$$

$$-V_{\mathrm{Q}}\sin(\omega t)\cos(\omega_{\mathrm{LO}}t)=-\frac{V_{\mathrm{Q}}}{2}\left[\sin(\omega_{-}t)+\sin(\omega_{+}t)\right] \tag{39}$$

The low-pass time constant τ_{int} has to be carefully chosen. A filter with a long time constant passes less noise, but also filters out rapid fluctuations of the signal. The filter is therefore generally chosen to pass all frequency components of interest in the demodulated signal.

3. Homodyne and heterodyne detection

In homodyne detection (as illustrated in Fig. 2), the signal $V_{\mathrm{out}}(t)$ at frequency f_{out} is demodulated using the frequency of the input signal so $f_{\mathrm{LO}}=\omega_{\mathrm{LO}}/2\pi=f_{\mathrm{in}}$. This results in two signals at frequencies $(f_{\mathrm{out}}-f_{\mathrm{in}})=f_{\mathrm{m}}$ and $f_{\mathrm{out}}+f_{\mathrm{in}}$. The second term can be filtered out so only the signal at the frequency f_{m} remains, which represents the modulations of the sample impedance. In heterodyne detection, $V_{\mathrm{out}}(t)$ is demodulated using $f_{\mathrm{LO}}\neq f_{\mathrm{in}}$. The result is two signals at frequencies $f_{\mathrm{out}}-f_{\mathrm{LO}}$ and $f_{\mathrm{out}}+f_{\mathrm{LO}}$, the second term being usually filtered out.

III. MEASURING A RESISTIVE DEVICE

In this section, we detail how radio-frequency measurements are used to probe the resistance of a quantum device. We start by discussing the matching condition between a transmission line (Section III A) and a quantum device and we then focus on two examples which are mostly used in quantum electronic experiments: the quantum point contact (QPC) charge sensor and the single-electron transistor (SET) charge sensor together with its lookalike, the quantum dot (QD) charge sensor (Section III B). Later, we describe how these devices can be used as charge sensors (Section III C) and which applications arise from the combination of radio-frequency measurements with charge sensing techniques (Section III D). Next, we present an exemplary phenomenon of dissipation induced by the rf drive, the Sisyphus resistance, which can be used to study dynamic dissipation in two-level systems (Section III E). We conclude by discussing the difficulty to scale up for measuring numerous quantum devices such as qubits (Section III F)

A. Matching resistive devices with a LC resonator

As shown in Section II, monitoring the reflection coefficient Γ can, in particular, reveal changes in the resistance (real part) of a load impedance. Near the resonant frequency, Γ becomes highly sensitive to the variations of Z_{load}. However, according to Fig. 3, Z_{load} needs to be close to the characteristic impedance of the transmission line, $Z_0=50\ \Omega$, to ensure good sensitivity to sample resistance changes. This poses a problem since the impedance of quantum devices is typically much larger. To match the transmission line impedance, the quantum device must be embedded in a matching network.

L-matching networks, particularly low-pass LC circuits, are widely used because they consist of only two elements. However, more complex matching networks can be employed, especially if independent control of the matching condition and network quality factor is needed. Their main components are an inductor L_{C}, placed between the line and the sample, and a capacitance C_{P} located in parallel to the sample (Fig. 7(a)). The capacitance can be chosen to be a real or parasitic element. We also introduce parasitic resistors to model dissipation in the circuit; here R_{L} models ohmic losses in the inductor, while R_{C} models dielectric losses in the capacitor. As we shall see in Section V, to optimize the sensitivity to resistance changes, a good matching network should usually minimize R_{L} and maximize R_{C}.

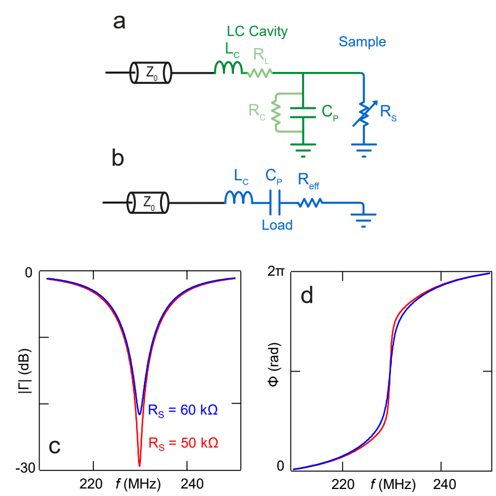

FIG. 7. (a) Schematic of a reflectometry circuit used to measure a variable resistor R_{S}. The sample is embedded in an L-matching network made of an inductance L_{C} and a capacitance C_{P}, to match the characteristic impedance Z_0 of the line. The resistance R_{L} represents dissipation in the inductor and the resistance R_{C}, dielectric losses. (b) Equivalent RLC series circuit at the resonant frequency. Magnitude (c) and phase spectrum (d) of the reflection coefficient $|\Gamma|$ for two values of R_{S}. The other circuit parameters are $L_{\mathrm{C}}=800$ nH, $R_{\mathrm{L}}=20\ \Omega$, $R_{\mathrm{C}}=100$ MΩ and $C_{\mathrm{P}}=0.6$ pF.

The impedance of this circuit, which presents itself as a load on the transmission line, is

$$Z_{\mathrm{load}} = j\omega L_{\mathrm{C}} + R_{\mathrm{L}} + \frac{R_{\mathrm{eq}}}{1 + j\omega R_{\mathrm{eq}} C_{\mathrm{P}}}, \tag{40}$$

where $R_{\mathrm{eq}} = R_{\mathrm{S}}||R_{\mathrm{C}}$ is the parallel combination of R_{S} and R_{C}. On resonance, $\mathrm{Im}(Z_{\mathrm{load}}) = 0$, which leads to an analytical expression for the resonant frequency. For typical circuit parameters such that $L_{\mathrm{C}}/R_{\mathrm{eq}}^2 C_{\mathrm{P}} \ll 1$, it reads

$$\omega_{\mathrm{r}} = \frac{1}{\sqrt{L_{\mathrm{C}} C_{\mathrm{P}}}} \tag{41}$$

where $\omega_{\mathrm{r}} = 2\pi f_{\mathrm{r}}$. Substituting Eq. (41) into Eq. (40), the impedance of the circuit at resonance simplifies to that of a series *LCR* circuit (Fig. 7(b)), similar to the example in Section II, with an overall impedance given by[15]

$$Z_{\mathrm{load}} \approx R_{\mathrm{eff}} + j\omega L_{\mathrm{C}} + \frac{1}{j\omega C_{\mathrm{P}}} \tag{42}$$

$$= R_{\mathrm{eff}} + j2\sqrt{\frac{L_{\mathrm{C}}}{C_{\mathrm{P}}}}\frac{\Delta\omega}{\omega_{\mathrm{r}}}, \tag{43}$$

where $\Delta\omega$ is the difference between the probing angular frequency ω and ω_{r}, and the effective resistance reads

$$R_{\mathrm{eff}} = \frac{L_{\mathrm{C}}}{C_{\mathrm{P}} R_{\mathrm{eq}}} + R_{\mathrm{L}} \tag{44}$$

$$\xrightarrow{\mathrm{ideal}} \frac{L_{\mathrm{C}}}{C_{\mathrm{P}} R_{\mathrm{S}}}. \tag{45}$$

Equation (45) is a key result of this section, showing that an L-matching network transforms the impedance of the device to a new value that can be more easily matched to the impedance of the line. The matching resistance, which is the device resistance for which the tank circuit matches the line, i.e. $R_{\mathrm{eff}} = Z_0$, is thus ideally

$$R_{\mathrm{match}} = \frac{L_{\mathrm{C}}}{C_{\mathrm{P}} Z_0}. \tag{46}$$

Hence an rf designer should carefully choose the values of L_{C} and C_{P} that will make R_{match} equal to the on-state resistance of the device to be measured.

The measurement principle relies on the change of the reflection coefficient Γ induced by a change in R_{S}. This is illustrated in Figure 7(c) in which a change of sample resistance embedded in a matching network manifests as a change in the reflection power near the resonance frequency. Likewise, the reflected phase changes due to the change in loaded quality factor (Fig. 7(d)). The carrier frequency must be chosen at $\omega \approx \omega_{\mathrm{r}}$ to maximise the sensitivity to resistance changes. Guidelines on how to optimise the design of the matching network and improve the sensitivity to resistance changes are developed in Section V.

B. Measuring the charge occupation of quantum dots with charge sensors

The direct measurement of quantum devices, and specifically QDs, is a challenging task due to large time constants associated with their typical high impedance. This has motivated the use charge detectors coupled to the quantum system as local and sensitive electrometers to investigate a variety of phenomena including detection of single charge occupation in QDs[16,17], time domain measurements of tunneling events[18–20], charge and spin single-shot readout and coherent manipulation[21–25]. In this section, we analyse the working principle of the most common type of charge detectors: the QPC, the SET and the QD charge sensor.

1. Quantum point contact charge sensors

A QPC is a constriction in which transport occurs through 1-dimensional subbands[26]. For structures with high mobility and at low temperature, the conductance G_{QPC}, tends to be quantized in plateaus at multiples of the conductance quantum $G_0 = 2e^2/h = 77.5$ μS (or at e^2/h under high magnetic field)[27]. In the ballistic limit,

$$G_{\mathrm{QPC}} = \frac{e^2}{h}\sum_n f_e(E_n) g_n \tag{47}$$

with f_e the Fermi probability distribution and E_n and g_n the energy and degeneracy of the n^{th} subband.

QPCs are easily realised in nanowires whose linear geometry provides a natural one-dimensional confinement, or in two-dimensional electron (hole) gases (2DEGs or 2DHGs) in which the current path is restricted to a narrow channel using depletion gates as in Fig. 8(a). The QPC (in red) is created by just a single additional gate V_{QPC} creating a constriction against the DQD barriers. The two sides of the constriction are connected to contact leads that allow the measurement of the QPC conductance G_{QPC}. As the channel is narrowed using a gate voltage, the conductance decreases (Figs. 8(b) and 9(b)). At gate voltage settings for which the conductance changes steeply, the QPC is highly sensitive to its electrostatic environment.

This property makes the QPC an efficient charge sensor for nearby QDs[16,28]. Each additional charge present on the QDs contributes an effective voltage which shifts the conductance-versus-gate voltage curve of the QPC. Therefore variations in the charge configuration of the QD result in discrete changes in G_{QPC}. The gate voltage is tuned to the point of maximum derivative of the conductance curve for the best sensitivity, which is often midway between the first conductance plateau and pinch-off[29], setting the QPC resistance to around 25.8 kΩ.

2. Single-electron transistor and quantum dot charge sensors

The SET and QD charge sensors are three-terminal devices in which a small region of conducting material (the 'island') is

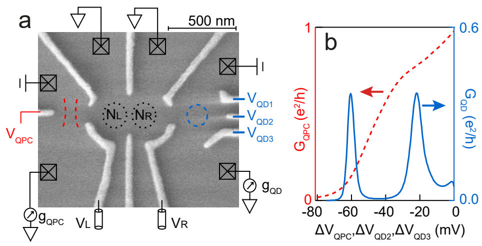

FIG. 8. A GaAs/AlGaAs quantum device incorporating a double quantum dot and two charge sensors. (a) SEM micrograph of the device. Metallic gates define a double quantum dot (black dashed lines) which is capacitively coupled to a QPC charge sensor (red dashed lines) and a QD charge sensor (blue dashed lines). Leads through which these two charge sensors are measured, are marked by crossed squares. (b) dc conductance of the QPC (G_{QPC}) and the QD charge sensor (G_{QD}) as a function of their respective control gate voltages. The most sensitive operation points are typically those with highest transconductance, i.e. those with the steepest dependence of conductance on gate voltage. Reproduced with permission from Phys. Rev. B 81, 161308(R) (2010). Copyright (2010) American Physical Society.

connected via tunnel barriers to two charge reservoirs, source and drain. Furthermore, the island is capacitively coupled to a gate electrode that enables changing the charge occupation in the island by means of gate voltage changes. SETs can be realised in metals[6,30] or semiconductors, whereas QD charge sensors require quantum confinement, which can usually only be achieved in semiconducting nanostructures[31,32]. In Fig. 8(a) a QD charge sensor is realised by the confinement potential of three gates $V_{\mathrm{QD1\text{-}3}}$ (1 and 3 control primarily the tunnel barrier resistance and 2 the QD charge occupation). The sensor is capacitively coupled to a DQD and tunnel-coupled to two (source and drain) reservoirs.

Electronic transport through SETs and QDs is governed by charge quantization in the island, i.e. Coulomb blockade[33]. For Coulomb blockade to be manifest, the charging energy of the island E_{C} needs to be larger than $k_{\mathrm{B}}T$. Besides, the resistance of each of the tunnel barriers, R_{T}, needs to be larger than the von Klitzing resistance $R_{\mathrm{K}} \approx 25.8$ kΩ to ensure that the energy uncertainty of each charge state is smaller than E_{C}. At finite bias, Coulomb blockade gives rise to regular sharp conductance peaks as a function of the gate voltage[34] (Fig. 8(b)).

In an SET, transport is considered through a quasi-continuum of states[35]. The SET conductance as function of the gate voltage V_{G}, close to a charge degeneracy point V_{G}^0, can be described as

$$G_{\mathrm{SET}} = G_{\max} \cosh^{-2}\left[\frac{\alpha(V_{\mathrm{G}} - V_{\mathrm{G}}^0)}{2.5 k_{\mathrm{B}} T}\right]. \tag{48}$$

Here $G_{\max}$ represents the conductance at the charge degeneracy point ($V_{\mathrm{G}} = V_{\mathrm{G}}^0$), and α is the ratio of the gate and total capacitance (lever arm).

If the island is made sufficiently small, quantum confinement can lead to electronic transport through discrete energy levels once the energy level spacing, ΔE is larger than $k_{\mathrm{B}}T$[36–41]. In this case, charge tunnelling occurs through a single level. We refer to these devices as QDs. The QD conductance can be expressed as[35]:

$$G_{\mathrm{QD}} = G_{\max} \frac{\Delta E}{4 k_{\mathrm{B}} T} \cosh^{-2}\left[\frac{\alpha(V_{\mathrm{G}} - V_{\mathrm{G}}^0)}{2 k_{\mathrm{B}} T}\right]. \tag{49}$$

Because QD charge sensors present sharper conductance peaks, they can reach higher sensitivity than SETs. Charge sensing with SETs or QD charge sensors works on the same principle as with QPCs[1,2,42]. Charge sensing is realised by monitoring the conductance of the island at a constant gate voltage, chosen on the flank of a Coulomb peak so that the conductance depends steeply on the electrical potential. When a charge is added to or removed from a nearby device, the small variation of electric field shifts the position of the Coulomb peak on the gate voltage axis resulting in a different current.

Both SETs and QD charge sensors are now commonly used for charge sensing, with the choice of one or the other being mostly dependent on the geometry and the material of the experiment. QDs tend to be used in systems where quantum confinement can be routinely be achieved. Materials with low effective mass like AlGaAs/GaAs heterostructures[43] or nanowires[38], that provide natural confinement, are typical examples. On the other hand, SETs are more common in materials with higher effective mass like silicon[32,44,45]. SETs and QDs are technologically more complex to fabricate than QPCs because of the additional number of gates needed, but provide in general a better sensitivity because of their steeper slope. However, QPCs work over a wider range of gate voltages and often have a greater dynamic range to charge sensing signals than SETs and QD charge sensors whose sensitivities vanish deep inside Coulomb blockade. Voltage cross-talk from neighbouring gates also affects the bias point and hence the conductance of SETs and QD charge sensors, thus requiring re-adjustment of the gate voltages to maintain the sensors at the bias point for maximum sensitivity. This has recently motivated the use of advanced compensation strategies based on fast feedback[46].

3. *Sensitivity and limits of low-frequency charge sensors*

We have just seen that devices such as the QPC and the SET can act as fine electrometers due to their sharp transconductance at low temperatures. However, when measured in the setup Fig. 1(a), their measurement bandwidth is limited to a few tens of kilohertz, due to the *RC* constant formed between the impedance of the current amplifier and the capacitance of the cabling leading to the first amplifier stage ($C_{\mathrm{line}} = 0.1 - 1$ nF), usually sitting at room temperature, ∼ 1.5 m away from the device. This measurement bandwidth is far below the intrinsic maximum bandwidth of the charge sensors, which in the case of the SET is set by the intrinsic *RC* constant of the tunnel barriers ($R \approx R_{\mathrm{K}}$ and $C \approx 1$ fF) and can exceed 10 GHz. The limited bandwidth of conventional low-frequency measurements has a knock-on detrimental effect on the sensor's charge sensitivity. The charge sensitivity of a sensor is not exclusively determined by the sharpness of its transconductance but also by the noise level at the measurement frequency which, as we shall see later, can be substantial at low frequencies.

To quantify the sensitivity of a sensor and discuss its ultimate limits, we resort to the definition of charge sensitivity. The charge sensitivity $\sqrt{S_{QQ}^{\mathrm{N}}}$ of a charge detector tells us the amount of charge Q that can be discerned in a measurement lasting a second. It is defined as

$$\sqrt{S_{QQ}^{\mathrm{N}}}(f) = \frac{\sqrt{S_{II}^{\mathrm{N}}(f)}}{|\partial I/\partial Q|} \tag{50}$$

where $S_{II}^{\mathrm{N}}(f)$ is the current noise spectral density[47] and $\partial I/\partial Q$ is the change in device current I induced due to a change in the charge Q on the device, a magnitude proportional to the transconductance. This figure is the noise-limited charge sensitivity. Charge sensitivities as good as 20 $\mu e/\sqrt{\mathrm{Hz}}$ have been measured for SETs in the normal state at 4.4 kHz[48], outperforming state-of-the-art conventional transistors by three orders of magnitude[49]. However, this number is still far from the theoretical limit of the SET, which is dominated by shot noise (at dilution refrigerator temperatures Johnson-Nyquist noise is typically much smaller). Shot noise has a current noise spectral density given by[50]

$$S_{II}^{\mathrm{N}} = F2eI \tag{51}$$

where F is the Fano factor, which varies between 0.5 and 1 in the Coulomb blockade regime[51] and accounts for the correlation of between charge tunneling events. I is the average current flowing through the device. In this limit, the ultimate charge sensitivity reads[52]

$$\sqrt{S_{QQ}^{\mathrm{N}}} = 1.9e\,(R_{\mathrm{T}}C_{\Sigma})^{1/2}\left(k_{\mathrm{B}}TC_{\Sigma}/e^2\right)^{1/2}. \tag{52}$$

For common experimental values $C_{\Sigma} = 0.45$ fF, $R_{\mathrm{T}} = 100$ kΩ and $T = 100$ mK, Eq. (52) gives 1 $\mu e/\sqrt{\mathrm{Hz}}$. As we can see, experimental values are far from this ultimate limit. The reason for this loss of sensitivity is additional sources of noise that appear at the low frequencies of the measurements. For example $1/f$ noise, which originates from time-dependent occupation of charge trap centres in the neighbourhood of the charge sensor, can be substantial below 10 kHz. Several solutions were proposed to increase the bandwidth such as the use of superconducting SETs that have a lower tunnel barrier resistance[53] and bringing the amplifier closer to the SET. However, these approaches only improved the bandwidth moderately up to 700 kHz[4,54].

The measurement bandwidth limitation can be overcome by the use of rf reflectometry, which removes the effect of C_{line} by impedance matching the device to a high-frequency line. Typical operation frequencies are in the few megahertz to 2 GHz regime (set by the first amplifier stage, see Section VI) and the measurement bandwidth can reach values as high as 100 MHz[6]. This phenomenal increase in operational frequency, closer to the intrinsic limit of the devices, allows operation well above the $1/f$ noise and, as we shall see later, leads to a subsequent improvement of the charge sensitivity and measurement speed.

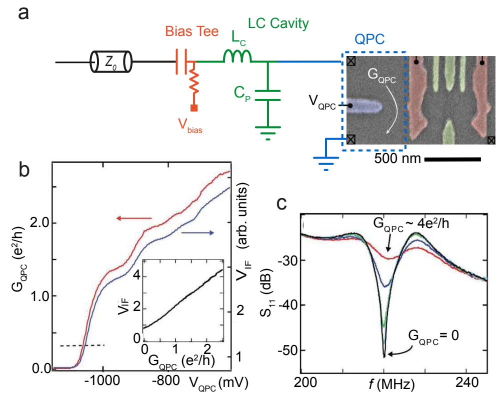

FIG. 9. (a) An LC matching network is attached to one of the contact leads of a QPC. In this example[56], $L_{\mathrm{C}} = 820$ nH and $C_{\mathrm{P}} = 0.63$ pF. The bias tee, made of a 100 pF capacitor in the ac path and a 5 kΩ resistor in series with a 100 nH inductor (not shown) in the dc path, allows a dc bias to be applied across the QPC. (b) Demodulated response V_{IF} (right) and dc conductance of the QPC G_{QPC} (left) versus gate voltage (V_{QPC}). The dashed line indicates the operation point for charge sensing. The inset shows the transfer function: V_{IF} vs conductance. (c) Reflection ratio S_{11} versus frequency for different values of G_{QPC}. Reproduced from[56], with the permission of AIP Publishing.

C. Reflectometry of charge sensors

In this subsection, we present examples from the literature where rf-QPCs and rf-SETs have been used to measure QDs in their periphery.

1. Radio-frequency measurement of a QPC

Radio frequency measurements of a QPC[29,55–61] and of an SET/QD[30,62–66] are similar in principle. The charge sensor is embedded as a resistive element in a matching network at the end of a transmission line in a setup similar to Fig. 7.

The equivalent circuit for an rf-QPC shown in Fig. 9(a) is similar to the one presented in Fig. 7, with $R_{\mathrm{S}} = 1/G_{\mathrm{QPC}}$ being the QPC resistance (Fig. 9). In a reflectometry setup, the matching network is connected to one of the contacts of the charge sensor while the other is grounded. Further, a bias tee allows a dc voltage to be added to the source-drain bias, so that the dc conductance can be measured simultaneously with the rf response. The load impedance can be expressed using Eq. (40) allowing the reflection coefficient to be calculated.

The measurement detects the change of rf reflection induced by variations in R_S. In the example of Fig. 9(c), the reflectance S_{11} shows a trough at the resonance frequency, which is deepest when the QPC is pinched off ($G_{QPC} = 0$). At higher gate voltages the resistance R_S of the QPC decreases and the circuit becomes undercoupled, resulting in a higher reflection. As shown in Fig. 9(b), this allows the QPC conductance to be probed over a wide gate voltage range. When $G_{QPC} \approx 4e^2/h$, the trough at the resonant frequency is barely evident.[67]

2. Radio-frequency measurement of the SET (and QD)

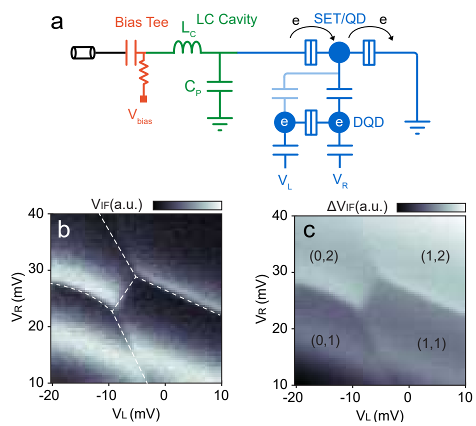

FIG. 10. Radio-frequency charge sensing a DQD with a QD charge sensor[68]. (a) Schematic of an rf-QD/SET charge sensor probing the charge occupation of a DQD. The charge sensor has a strong capacitive coupling with the right QD and a smaller coupling with the left one. (b) Demodulated voltage V_{IF} as a function of QD plunger gates V_L and V_R. Dark regions correspond to the QD Coulomb valley where the sensitivity is low, while the bright regions corresponds to the QD Coulomb peak which is highly sensitive to the DQD charge configuration. Abrupt shifts of the Coulomb peak occur each time the occupation of the DQD changes, giving rise to the honeycomb pattern typical of a DQD charge stability diagram. (c) The same data, plotted with a plane background subtracted to make the honeycomb clearer. The four charge configurations are labelled according to the occupation of the DQD. Federico Fedele, Anasua Chatterjee, Saeed Fallahi, Geoffrey C. Gardner, Michael J. Manfra, and Ferdinand Kuemmeth, PRX Quantum 2, 040306, 2021; licensed under a Creative Commons Attribution (CC BY) license.

Similar to the rf-QPC, the rf-SET and rf-QD charge sensors are connected to an *LC* matching network via one of the contact leads. Readout of the SET (QD) resistance is then accomplished by monitoring the reflected amplitude of a high-frequency signal, see Fig. 10(a). Compared to the rf-QPC, rf-SET and rf-QD are more sensitive[43], but their higher resistance (see Fig. 8(b)) makes them more challenging to match to a 50 Ω line[55].

In Fig. 10(b) we show the demodulated voltage V_{IF}, which is proportional to the sensor conductance, measured as a function of gates voltages V_R and V_L, which control the number of electrons in a DQD device similar to the one shown in Fig. 8. In this plot, the color scale can be directly associated with variations in the absorption of the rf signal by the resonant circuit, where the rf-QD charge sensor is embedded. Dark regions correspond to Coulomb valleys of the charge sensor. Here the charge sensitivity is low, since changes in the charge neighbourhood produce minor changes in the QD resistance. Further, the high QD resistance places the system off the matching condition and most of the rf carrier power gets reflected. Conversely, bright regions correspond to the charge sensor being biased near a Coulomb peak setting the system closer to the matching condition where the sensitivity is best. Further, in this bias condition, the charge sensor's conductance is strongly dependent on the surrounding charge. Sudden jumps in the position of the Coulomb peak are caused by charging and discharging of the neighbouring QDs, which suddenly detune the QD charge sensor and allow the DQD's charge stability diagram (highlighted with white dashed lines) to be mapped down to the very last electrons.

Figure 10(c) shows a common way to present these data, obtained from Fig. 10(b) after the subtraction of a background plane ΔV_{IF}. This measurement reveals four distinct regions associated with four different charge configurations where the number of charges within the dots is stable and described by the numbers in parentheses, corresponding to the left and right dot. Another typical way to present these data in the literature (not shown), is to plot the derivative of the raw data to better highlight the charge transitions. Note how charge sensing allows a clear distinction between the two-electron configurations (0,2) and (1,1). The corresponding interdot transition is primarily of importance for measuring spin states via spin-to-charge conversion[69] and spin qubits in general[23].

D. Readout performance

The first radiofrequency measurement of a SET in 1998[6] obtained a charge sensitivity of 12 $\mu e/\sqrt{\text{Hz}}$ with 1.1 MHz bandwidth. In this case, the charge sensitivity $\sqrt{S_{QQ}^{\text{N}}}$ refers to probing the charge occupation in the SET island itself (see Section V D for more explanation of charge sensitivity and how to measure it.). Since then, devices based on Al/AlO$_x$-based tunnel junctions have demonstrated sensitivities as good as 1 $\mu e/\sqrt{\text{Hz}}$ in the normal state and 0.9 $\mu e/\sqrt{\text{Hz}}$ in the superconducting state[63]. These numbers are more than an order of magnitude better than their low-frequency counterparts but are still not at the theoretical limit, which, for rf-SETs, is only 1.4 times worse than that of Eq. (52)[52]. The reason is that the noise in these experimental demonstrations contains contributions from the first amplifying stage as well as shot noise, as we shall see in Section VI. These charge sensors have been used or proposed for readout of charge qubits[30], lifetime measurements of Cooper-pair box states[15], and real-time measurements of tunneling events in quantum dots[70].

Later, rf-QPC and rf-SET charge sensors made of semiconductor materials were used to measure the charge occupation of DQDs. To date, in semiconductors, the most sensitive dissipative electrometers are the rf-QPC and the rf-SET providing charge sensitivities in the $\mu e/\sqrt{\mathrm{Hz}}$ range. The best reported sensitivity for the rf-QPC is 146 $\mu e/\sqrt{\mathrm{Hz}}$[71] with a bandwidth of at least 1 MHz, demonstrated on a GaAs/AlGaAs heterostructure. In silicon, the best reported sensitivity for an rf-SET is 10 $\mu e/\sqrt{\mathrm{Hz}}$[64]. As we shall discuss in Section V D, the figures for rf-QPCs and rf-SETs are typically reported under different benchmarking conditions: QPC sensitivities are usually specified in terms of charge on the object being sensed, but SET sensitivities are in terms of the charge on their own island, the two being linked by the capacitive coupling ratio to the system to be sensed (see Eq. (129)). Hence a direct comparison can only be made if the ratio is known.

At present, charge sensing via rf-QPCs and rf-SETs is routinely used in, but not limited to, spin-qubit and quantum information processing experiments to achieve rapid spin-to-charge conversion measurements. These are key to spin-qubit readout, ultimately leading to single-shot-readout[72–74], quantum non-demolition measurements[75], and fast qubit-gate operations with demonstrated fidelities above the fault-tolerant threshold[76,77]. Recently, rf-SETs have also been implemented as a fast characterization tool for nanowires[78], nanowires coupled to superconducting resonators[79] and hybrid semiconductor-superconductor nanowire systems (InAs/Al)[80]. The latter example is relevant for the search of Majorana zero modes, (see Section IX B). In Supplementary Table SI, we have summarised the charge sensitivity obtained in various experiments in the literature.

E. The Sisyphus resistance

In the previous subsections, we have learned how rf reflectometry can be used to probe the resistance of nanoelectronic devices on short timescales, for example for fast charge sensing. Beyond this possibility, rf reflectometry offers the opportunity to induce dynamical effects on the sensed nonelectric devices themselves. In this subsection, we deal with a prototypical example of an induced dissipative phenomenon, that of excess dissipation induced by an rf drive: the Sisyphus resistance.

We focus on devices that can be modeled by a two-level system and are driven at a rate comparable to the the their tunneling rate. Under those conditions dynamic power dissipation occurs. Understanding dissipation in these systems is important since two-level systems are the basis of quantum bits and one of the detrimental elements in achieving high quality factors in electrical resonators. We choose the example of a single-charge QD capacitively coupled to a gate electrode and tunnel-coupled to a single charge reservoir to allow particle exchange (Fig. 11). The two energy levels involved correspond to the dot having none (E_0) or one (E_1) excess electron whose energy separation can be controlled by a parameter n_G, the reduced gate voltage, in the following way,

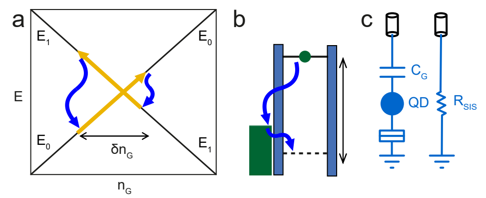

FIG. 11. Process associated with Sisyphus resistance. (a) Energy diagram of an uncoupled two-level system representing an (un)occupied QD $E_1(E_0)$ as a function of the reduced gate voltage. The yellow arrows indicate the work done by the rf voltage source (non-adiabatic transitions) and the blue wiggling arrows indicate phonon emission due to inelastic tunneling. (b) Schematic representation of a QD (green circle) tunnel-coupled to a charge reservoir (in green) in the situation described in panel (a). The rf voltage source varies the relative position of the QD electrochemical level with respect to the Fermi energy of the reservoir (amplitude indicated by the double arrow). The blue arrows indicate the inelastic tunneling events. (c) dc (left) and ac (right) small-signal equivalent circuits of the QD as seen from the gate electrode.

$\Delta E = E_1 - E_0 = E_\mathrm{C}(1-2n_\mathrm{G})$[81]. Here E_C is the charging energy of the device.

To explain the physics, let us assume the system is biased so that it has an equilibrium reduced gate voltage, n_G^0, away from the degeneracy point, and is then driven by an rf gate voltage so that the voltage varies as $n_\mathrm{G}(t) = n_\mathrm{G}^0 + \delta n_\mathrm{G}\sin(\omega t)$, where δn_G is sufficiently large to bring the system past the degeneracy point. In the first half of the cycle, the system is driven past the degeneracy point non-adiabatically. At some point, due to the finite tunneling rates, it relaxes to the ground state, dissipating energy that had been provided by the rf generator. This excitation followed by tunneling occurs indefinitely generating an excess power dissipation in the system that can be modeled by a single resistor, i.e. the Sisyphus resistance R_SIS. The Sisyphus resistance can be calculated by solving the dynamics of the system using a master-equation formalism. The probabilities $P_{0(1)}$ to be in state $E_{0(1)}$ obey

$$\begin{aligned} \dot{P}_0 &= -\gamma_+ P_0 + \gamma_- P_1 \\ \dot{P}_1 &= \quad \gamma_+ P_0 - \gamma_- P_1 \end{aligned} \tag{53}$$

where $\gamma_\pm$ are the tunneling rates. For transitions between a charge reservoir with a 3D density of states and a QD with a discrete density states, the tunnel rates take the following form[82]:

$$\gamma_\pm = \frac{\gamma_0}{1+\exp\left(\pm\Delta E/k_\mathrm{B}T\right)} \tag{54}$$

where γ_0 is the maximum tunneling rate that applies away from the degeneracy point. We solve Eq. (53) to first order in δn_G to obtain the quasi-static probabilities

$$P_{0(1)} = P^0_{0(1)} - (+)\frac{\eta\delta n_G}{\omega^2+\gamma^2_{\text{tot}}}[\gamma_{\text{tot}}\sin(\omega t) - \omega\cos(\omega t)] \quad (55)$$

where $P^0_{0(1)}$ are the thermal probabilities at n^0_G,

$$\gamma_{\text{tot}} = \gamma_+ + \gamma_- \quad (56)$$

is the effective tunnel rate of the system and η is the induced probability oscillation[81]

$$\eta = P^0_1 \left.\frac{\partial\gamma_-}{\partial n_G}\right|_{n^0_G} - P^0_0 \left.\frac{\partial\gamma_+}{\partial n_G}\right|_{n^0_G}. \quad (57)$$

The average power dissipation over one period T can then be calculated as[82–84]

$$P_{\text{Sis}} = \frac{1}{T}\int_0^T [P_1\gamma_-\Delta E - P_0\gamma_+\Delta E]\,dt. \quad (58)$$

By comparing the averaged power dissipation with that of a resistor driven by an oscillatory voltage, we obtain the Sisyphus resistance:

$$R^{0D}_{\text{SIS}} = \frac{2k_BT}{(e\alpha)^2}\left(\frac{1+\gamma_0^2/\omega^2}{\gamma_0}\right)\cosh^2\left(\frac{\Delta E}{2k_BT}\right). \quad (59)$$

Here α is the ratio between the gate capacitance and total capacitance of the device. For the case of a 3D density of states in the island, the tunneling rates present a different expression,

$$\gamma_{\pm} = \frac{R_K}{R_T}\frac{\mp\Delta E/h}{1-\exp(\pm\Delta E/k_BT)} \quad (60)$$

where R_T is the resistance of the tunnel barrier. Hence the Sisyphus resistance reads

$$R^{3D}_{\text{SIS}} = \frac{R_T}{\alpha^2}\frac{2k_BT}{\Delta E}\left(1+\frac{\gamma^2_{\text{tot}}}{\omega^2}\right)\sinh\left(\frac{\Delta E}{k_BT}\right). \quad (61)$$

Radio-frequency reflectometry techniques have been instrumental in detecting excess dissipation in single-electron devices such as superconducting single-electron boxes[85], and silicon QDs[82].

F. Scaling up

Charge sensing has been instrumental in some of the most comprehensive studies of QD static and dynamical properties, however it suffers form a potential downside: It is an indirect measurement, i.e. it requires reading the state of a charge sensor that is placed in close proximity to the quantum device of interest. This becomes especially demanding in spin-qubits devices where the growing complexity of the modern geometries[68,86–88] poses substantial spatial constraints. A possible solution, that leverages the benefits of rf-reflectometry, is to measure the dispersive signal generated by the shifts of the QD's quantum capacitance[85,89]. This allows electron tunneling to be measured with rf reflectometry by embedding the QD in the matching network either via the dot's leads or via one of the existing gate electrodes. The latter is especially convenient to realize a compact sensing technique since it alleviates the need for external electrometers[89]. Due to its relevance and substantial technological development, in Section IV we present the theory and analyse the details about using rf measurements to probe directly the quantum capacitance of quantum devices.

IV. MEASURING A REACTIVE DEVICE

Radio-frequency measurements can be used to detect changes of capacitance or inductance in quantum devices. In this section, we detail the case of variable capacitors (Section IV A), which covers in particular the effective capacitance of gated semiconducting devices. However, this discussion is also applicable to variable effective inductance devices. We explain also the concept of *quantum capacitance* (Section IV B), which offers a means to measure various physical phenomena in quantum devices. Finally we explain the techniques of dispersive readout (Section IV C) to measure the charge occupation of quantum dots.

A. Measuring a capacitance

Consider a sample represented by a capacitance C_S. As with a resistive sample (Section III), LC resonators are used to match the characteristic impedance of a transmission line and translate the change of sample capacitance to a change of the reflection coefficient Γ.

The LC circuit used to measure a device with capacitance C_S is shown in Fig. 12(a). We represent the device as dissipationless (which as we shall see may be the case in some limits) and include in the circuit model sources of external dissipation. Here we assume a resistor R_L in series with the matching inductor L_C and a resistor R_C in parallel with the capacitor C_P. In this approximation, the impedance presented by the resonator to the transmission line is

$$Z_{\text{load}} = j\omega L_C + R_L + \frac{R_C}{1+j\omega R_C(C_P+C_S)}, \quad (62)$$

giving the resonance frequency

$$f_r = \frac{1}{2\pi\sqrt{L_C(C_P+C_S)}}. \quad (63)$$

The main effect of a change of C_S is to shift f_r, which changes the reflected signal as seen in Fig. 12(b-c). The phase change is particularly large near f_r and so it is sometimes used as output of the measurement. In the overcoupled regime $Q_{\text{int}} > Q_{\text{ext}}$ and when $Q_{\text{ext}}\Delta C_S/(C_P+C_S) \ll 1$, the phase change is[82,90]:

$$\Delta\Phi \equiv \Delta\arg(\Gamma(f)) \approx -2Q_{\text{ext}}\frac{\Delta C_S}{(C_P+C_S)}. \quad (64)$$

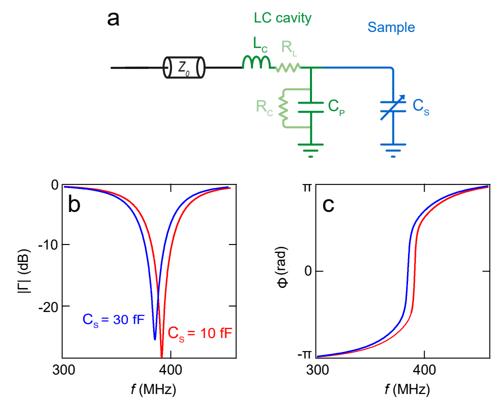

FIG. 12. (a) Schematic of a reflectometry circuit to measure a capacitive device C_{S} using an LC cavity formed by an inductance L_{C} and a capacitance C_{P}. Resistances R_{L} and R_{C} are used to model sources of external dissipation in the circuit. Z_0 is the characteristic impedance of the transmission line. (b) Reflection as function of the frequency f for the circuit in (a) with two different loads: $C_{\mathrm{S}} = 10$ fF (red) and $C_{\mathrm{S}} = 30$ fF (blue). A change in C_{S} results in a change of Z_{load} and a correspondent change in f_{r}. (c) Reflection phase corresponding to $C_{\mathrm{S}} = 10$ fF (red) and $C_{\mathrm{S}} = 30$ fF (blue). A change in C_{S} results in a significant change of phase near f_{r}. Simulation parameters: $L_{\mathrm{C}} = 270$ nH, $R_{\mathrm{L}} = 2\ \Omega$, $C_{\mathrm{P}} = 0.6$ pF, $R_{\mathrm{C}} = 10$ kΩ. The circuit is in the overcoupled regime $Q_{\mathrm{int}} > Q_{\mathrm{ext}}$.

Although the circuit equivalent appears similar to that of the resistive case, the sensitivity optimisation strategies are different and will be explained in Section V.

B. Quantum capacitance

Quantum capacitance is a quantum correction to the capacitance of a system, C_{S}, that arises due to the additional kinetic energy, in excess of the electrostatic energy, required to add charges to a material containing N charged fermions. This additional energy reflects the fact that since the particles are fermions they must enter unique quantum states with corresponding eigenergies as they fill the system.

1. *Quantum capacitance in low-dimensional systems*

The concept of quantum capacitance can be easily understood in the context of a capacitor with a geometrical capacitance C_{GEOM} formed by a metal gate electrode and a mesoscopic conductor separated by a thin dielectric layer, for example a metal-oxide-semiconductor capacitor[91]. Due to its metallic nature, the density of states in the gate is comparatively large compared to the relatively small capacitance in the mesoscopic conductor.

In such systems, a voltage ΔV_{G} applied to the metallic electrode produces an electrostatic ($\Delta V_{\mathrm{ELECT}}$) as well a chemical ($\Delta V_{\mathrm{CHEM}}$) potential change[92]

$$\Delta V_{\mathrm{G}} = \Delta V_{\mathrm{ELECT}} + \Delta V_{\mathrm{CHEM}} \text{ and } \Delta V_{\mathrm{ELECT}} = \frac{e\Delta N}{C_{\mathrm{GEOM}}}. \quad (65)$$

The contribution of the chemical potential μ can be expressed in terms of the induced change in charged particles in the mesoscopic conductor:

$$\Delta V_{\mathrm{CHEM}} = \frac{\Delta\mu}{e} = \frac{1}{e}\frac{d\mu}{dN}\Delta N. \quad (66)$$

Combining the equations above we arrive at the following expression:

$$\Delta V_{\mathrm{G}} = e\Delta N\left(\frac{1}{C_{\mathrm{GEOM}}} + \frac{1}{e^2 dN/d\mu}\right). \quad (67)$$

We see that the total capacitance of the system is composed by the geometrical capacitance in series with a correction that is exclusively dependent on the band structure, the quantum capacitance C_{Q}:

$$C_{\mathrm{S}}^{-1} = C_{\mathrm{GEOM}}^{-1} + C_{\mathrm{Q}}^{-1}, \quad (68)$$

with

$$C_{\mathrm{Q}} = e^2\frac{dN}{d\mu}. \quad (69)$$

To gain more insight into the origin of the quantum capacitance, it is useful to express the definition of the total number of particles in terms of the density of states $\rho(E)$ and the Fermi function $f_e(E)$ at the energy E

$$N = \int \rho(E) f_e(E) dE \quad (70)$$

where

$$f_e(E) = \frac{1}{e^{(E-\mu)/k_{\mathrm{B}}T} + 1}. \quad (71)$$

Because μ appears only in f_e, the quantum capacitance is proportional to the thermal average of the density of states around the chemical potential. In the limit of zero temperature, the quantum capacitance can be expressed as being proportional to the density of states at the Fermi energy, E_{F}:

$$C_{\mathrm{Q}} = e^2\frac{dN}{d\mu} \overset{T\to 0}{=} e^2\rho(E_{\mathrm{F}}). \quad (72)$$

For metallic devices and structures with negligible level spacing, the large density of states means that the quantum capacitance in Eq. (69) can be considered infinite, i.e. the total capacitance is simply equal to the geometric capacitance.

Since quantum capacitance is related to the thermodynamic electron compressibility $K = \frac{1}{N^2}\frac{dN}{d\mu}$, it is sometimes called *electron compressibility* when measured at finite temperatures and *quantum capacitance* strictly at $T = 0$ K[93]. Radio-frequency reflectometry can be an efficient way to measure the quantum capacitance of mesoscopic devices, especially low-dimensional systems where the density of states is low. The quantum capacitance can be computed explicitly according to the dimensionality of the system (2D, 1D or 0D) taking into account the specific density of states $\rho(E)$:

$$\rho_{2D}(E) = \sum_n \frac{gm^*}{2\pi\hbar^2} H(E - E_\mathrm{n}) \tag{73}$$

$$\rho_{1D}(E) = \sum_n \frac{g}{2\pi\hbar} \sqrt{\frac{m^*}{2(E - E_\mathrm{n})}} \tag{74}$$

$$\rho_{0D}(E) = \sum_n g\delta(E - E_\mathrm{n}) \tag{75}$$

where g is the degeneracy (valley, spin, orbital degree of freedom...), m^* is the effective mass, H is the Heaviside step function and E_n are the subband energy offsets. Examples of quantum capacitance measurements performed in 2D systems involve measurements of 2DEGs[94] as well as graphene[95–97] including magic-angle twisted bilayer graphene[98]. In 1D system there are carbon nanotubes[99] and quantum point contacts[100]. Some examples of 0D systems include GaAs QDs[85], InAs QDs [78] and Si QDs[101,102].

2. Quantum and tunneling capacitance in quantum dots

We have seen in Section III E that the ac response of low-dimensional systems may differ from the classical expectation. In this section, we show how the aforementioned ac component, the Sisyphus resistance (see Section III E) and now the quantum capacitance can manifest simultaneously in coupled two-level systems. More particularly, we will be able to make a further distinction about the origin of the capacitance term, and separate it into two components associated with reversible and irreversible charge tunneling[103], i.e. the pure quantum capacitance C_Q[104,105] as strictly defined in Eq. (72) and the tunneling capacitance C_TU[106,107], respectively.

In particular, we consider a tunnel-coupled DQD where the two dots QDi $i = 1, 2$ are connected to an rf gate electrode via gate capacitances $C_{\mathrm{G}i}$ and to grounded charge reservoirs at temperature T via $C_{\mathrm{D}i}$ (Fig. 13(a)). The interdot tunnel barrier has a mutual capacitance C_m and tunnel resistance R_T. The system can be described by an equivalent impedance Z_eq such that $V_\mathrm{G} = Z_\mathrm{eq} I_\mathrm{G}$, where V_G and I_G are the gate voltage and the gate current, respectively. Here, we consider the system driven by a small-amplitude excitation, $V_\mathrm{G} = \delta V_\mathrm{G} \sin(\omega t)$, where the excitation frequency is much smaller than the DQD frequency (i.e. $\omega \ll \Delta_\mathrm{C}/\hbar$), the rate of transit through the anticrossing is small and the DQD is weakly coupled to the reservoirs. In this limit, as we shall see later, the DQD impedance is $Z_\mathrm{eq} = (j\omega C_\mathrm{S} + 1/R_\mathrm{SIS})^{-1}$ where C_S is the total equivalent capacitance of the system and R_SIS is the Sisyphus resistance of the DQD.

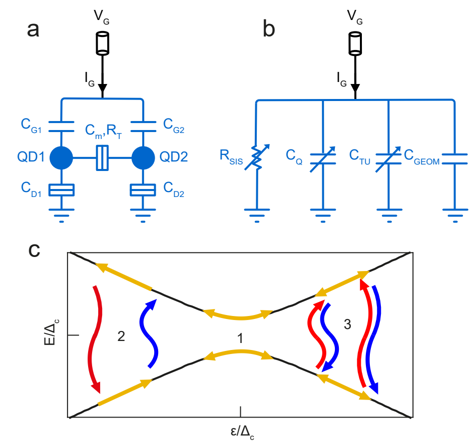

FIG. 13. Double quantum dot equivalent circuit and physical processes. (a) dc equivalent circuit of a DQD. The tunnel barriers, indicated by rectangles, consist of a capacitor in parallel with a resistor. (b) ac small-signal equivalent circuit of the DQD as seen from the gate electrode (G). The arrows indicate variable impedances. (c) Ground state and excited state energy of the DQD as a function of reduced detuning (black lines). The yellow arrows indicate the work done by the ac voltage source and the red and blue wiggling lines indicate phonon emission and absorption. The process associated with quantum capacitance is marked (1); that with Sisyphus resistance is marked (2) and that with tunneling capacitance is marked (3).

To obtain an analytical expression for Z_eq, we take the definition of the gate current

$$I_\mathrm{G} = \frac{d(Q_1 + Q_2)}{dt}, \tag{76}$$

where Q_i is the gate charge on the respective QDi. We expand the total gate charge in the DQD as a function of the gate coupling factors, $\alpha_i = C_{\mathrm{G}i}/(C_{\mathrm{D}i} + C_{\mathrm{G}i} + C_\mathrm{m})$ and the average electron occupation probability in QDi, P_i. We further assume the weak DQD coupling limit $C_\mathrm{m} \ll C_{\mathrm{D}i} + C_{\mathrm{G}i}$ and obtain

$$Q_1 + Q_2 = \sum_i \alpha_i (C_{\mathrm{D}i} V_\mathrm{G} + eP_i). \tag{77}$$

Using Eqs. (76 - 77) for inter-dot charge transitions, and noting that in that case $dP_2/dt = -dP_1/dt$, we obtain

$$I_\mathrm{G} = C_\mathrm{GEOM} \frac{dV_\mathrm{G}}{dt} + e\alpha' \frac{dP_2}{dt}. \tag{78}$$

Here, $C_\mathrm{GEOM} = \sum_i \alpha_i C_{\mathrm{D}i}$ and $\alpha' = \alpha_2 - \alpha_1$. We further note that the gate voltage induces an electrochemical potential energy difference between the QDs, i.e. the detuning $\varepsilon = \mu_2 - \mu_1 = -e\alpha'(V_\mathrm{G} - V_\mathrm{G}^0)$, where V_G^0 is the gate voltage offset at which the difference is zero. Hence, Eq. (78) can be further expanded into:

$$I_{\rm G} = C_{\rm GEOM}\frac{dV_{\rm G}}{dt} + e\alpha'\frac{dP_2}{dt} = \left[C_{\rm GEOM} - (e\alpha')^2\frac{dP_2}{d\varepsilon}\right]\frac{dV_{\rm G}}{dt}. \tag{79}$$

In Eq. (79), the semi-classical nature of our system becomes apparent. The first term is the geometrical capacitance of the DQD, whereas the second term, which appears as if it were a second capacitance in parallel, is related to the electron compressibility as defined below Eq. (72). It is linked to changes in charge occupation caused by time-dependent changes in detuning. However, as we shall see, in-depth investigation of this second term reveals two distinct physical mechanisms leading to charge redistribution. For now, the problem boils down to calculating the time-dependent occupation of QD2.

In order to understand the nature of this second term, we revert to the quantum description of the DQD. In the single-charge regime the DQD is described by the Hamiltonian

$$H = -\frac{\Delta_{\rm C}}{2}\sigma_x - \frac{\varepsilon}{2}\sigma_z, \tag{80}$$

where $\Delta_{\rm C}$ is the tunnel coupling energy and $\sigma_{x(z)}$ are the Pauli matrices. The eigenenergies are

$$E_\pm = \pm\frac{1}{2}\sqrt{\varepsilon^2+\Delta_{\rm C}^2}, \tag{81}$$

and the energy difference between the excited and the ground state is $\Delta E = E_+ - E_-$ (Fig. 13(c)). At large detunings, the eigenstates coincide with the charge states of the DQD. In general, the probability in the charge basis (P_2) can be expressed in terms of the probabilities in the ground (GS) and excited state (ES) energy basis, $P_\pm$,

$$P_2 = P_2^- P_- + P_2^+ P_+ = \frac{1}{2}\left[1 + \frac{\varepsilon}{\Delta E}\chi\right] \tag{82}$$

where $P_2^\pm = (1\mp\varepsilon/\Delta E)/2$[108] and $\chi = P_- - P_+$ is the polarization of the system in the energy basis. If the system is driven at a finite rate $\varepsilon(t) = \varepsilon_0 + \delta\varepsilon\sin(\omega t)$ (where ε_0 is the bias point) and the excitation rate is low $\omega \ll \Delta_{\rm C}^2/(\hbar\delta\varepsilon)$ to avoid Landau-Zener transitions[109], an electron can change its probability distribution in the DQD in two different ways[110]: (i) via adiabatic charge tunneling (process 1 in Fig. 13(c) associated with the derivative of $\varepsilon/\Delta E$), or (ii) irreversibly via phonon absorption and emission (processes 2 and 3, associated with the derivative of χ). By expanding the second term in Eq. (79), we can extract our first conclusion:

$$(e\alpha')^2\frac{dP_2}{d\varepsilon} = \frac{(e\alpha')^2}{2}\left[\frac{\partial^2 E_-}{\partial\varepsilon^2}\chi + \frac{\varepsilon}{\Delta E}\frac{\partial\chi}{\partial\varepsilon}\right]. \tag{83}$$

The first term on the right can be associated with the description of quantum capacitance in QDs in the literature as originating from the second derivative of the eigenenergies with respect to detuning[32,85,111,112]. It coincides with the strict definition of quantum capacitance being the electron compressibility at $T = 0$ K. The second term is linked to irreversible redistribution processes that, as we shall see, lead to Sisyphus dissipation and also to an additional source of capacitance, the tunneling capacitance. To gain further insight into the second term, we calculate changes in χ using the master equation formalism introduced in Section III E to first order approximation in $\delta\varepsilon/\Delta_{\rm C}$ and find

$$\delta\chi = \frac{-2\eta\delta\varepsilon}{\omega^2+\gamma_{\rm tot}^2}[\gamma_{\rm tot}\sin(\omega t) - \omega\cos(\omega t)]. \tag{84}$$

Here, $\gamma_{\rm tot}$ is the characteristic relaxation rate of the system and η relates to the amplitude of the induced probability oscillations. More concretely, $\gamma_{\rm tot} = \gamma_+ + \gamma_-$ where $\gamma_+ = \gamma_{\rm C} n_{\rm p}$ is the phonon absorption rate, $\gamma_- = \gamma_{\rm C}(1+n_{\rm p})$ is the phonon emission rate, $\gamma_{\rm C}$ is a material-dependent charge relaxation rate and $n_{\rm p} = (\exp(\Delta E/k_{\rm B}T)-1)^{-1}$ is the phonon occupation number. Hence, $\gamma_{\rm tot}$ can be expressed as

$$\gamma_{\rm tot} = \gamma_{\rm C}\coth(\Delta E_0/2k_{\rm B}T). \tag{85}$$

Further, η, according to Eq. (57) can be written as

$$\eta = \frac{\gamma_{\rm tot}}{4k_{\rm B}T}\frac{\varepsilon_0}{\Delta E_0}\cosh^{-2}\left(\frac{\Delta E_0}{2k_{\rm B}T}\right). \tag{86}$$

By inserting the detuning derivative of the change in energy polarization into Eq. (83) and averaging over a cycle of the rf signal we get

$$\begin{aligned} I_{\rm G} = {} & C_{\rm GEOM}\frac{dV_{\rm G}}{dt} + \frac{(e\alpha')^2}{2}\frac{\Delta_{\rm C}^2}{(\Delta E_0)^3}\chi^0\frac{dV_{\rm G}}{dt} \\ & + \frac{(e\alpha')^2}{2}\frac{\varepsilon_0}{\Delta E_0}\frac{2\eta\gamma_{\rm tot}}{\omega^2+\gamma_{\rm tot}^2}\frac{dV_{\rm G}}{dt} + \frac{(e\alpha')^2}{2}\frac{\varepsilon_0}{\Delta E_0}\frac{2\eta\omega^2}{\omega^2+\gamma_{\rm tot}^2}V_{\rm G}, \end{aligned} \tag{87}$$

where $\chi^0 = \tanh(\Delta E_0/2k_{\rm B}T)$ is the equilibrium polarization and $\Delta E_0 = \Delta E(\varepsilon = \varepsilon_0)$. From Eq. (87) we find the form of the equivalent impedance of the system, $Z_{\rm eq}$. The prefactors in the terms linear in $dV_{\rm G}/dt$ correspond to capacitances, whereas the prefactor in the linear term in $V_{\rm G}$ is a conductance. The reactive terms add up to a total sample capacitance $C_{\rm S}$, see Fig. 13(b),

$$C_{\rm S} = C_{\rm GEOM} + C_{\rm Q} + C_{\rm TU}. \tag{88}$$

which corresponds to the sum[113] of the geometrical capacitance

$$C_{\rm GEOM} = \sum_i \alpha_i C_{{\rm S}i}, \tag{89}$$

the quantum capacitance

$$C_{\rm Q} = \frac{(e\alpha')^2}{2}\frac{\Delta_{\rm C}^2}{(\Delta E_0)^3}\chi^0, \tag{90}$$

and the tunneling capacitance

$$C_{\rm TU} = \frac{(e\alpha')^2}{2}\frac{1}{2k_{\rm B}T}\left(\frac{\varepsilon_0}{\Delta E_0}\right)^2\frac{\gamma_{\rm tot}^2}{\omega^2+\gamma_{\rm tot}^2}\cosh^{-2}\left(\frac{\Delta E_0}{2k_{\rm B}T}\right). \tag{91}$$

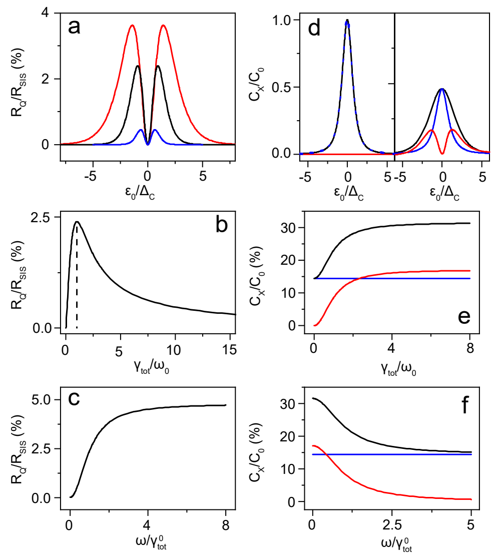

FIG. 14. Parametric impedances. (a) Relative change of the normalized inverse of the Sisyphus resistance versus reduced detuning for $k_\mathrm{B}T/\Delta_\mathrm{C} = 0.25, 0.5$ and 1 (blue, black and red traces respectively) and $\gamma_\mathrm{C} = \omega$. (b) $R_\mathrm{Q}/R_\mathrm{SIS}$ as a function of reduced relaxation rate for a given operation angular frequency ω_0 and (c) as a function of reduced operation angular frequency for $k_\mathrm{B}T/\Delta_\mathrm{C} = 0.5$ for a given relaxation rate γ^0_tot and $\varepsilon_0/\Delta_\mathrm{C} = 1$. (d) Normalized parametric (black), quantum (blue) and tunneling capacitance (red) as a function of reduced detuning for $k_\mathrm{B}T/\Delta_\mathrm{C} = 0.01, 1$ (left and right panels, respectively) and $\gamma_\mathrm{C}/\omega = 10$. Here, $C_0 = (e\alpha')^2/2\Delta_\mathrm{C}$ and we set $\alpha' = 1$. C_x/C_0 as a function of reduced relaxation rate (e) and reduced operation angular frequency (f) for $k_\mathrm{B}T/\Delta_\mathrm{C} = 1$ and $\varepsilon_0/\Delta_\mathrm{C} = 1$.

The dissipative term, which appears in parallel with C_S , is the Sisyphus resistance

$$R_\mathrm{SIS} = \frac{4R_\mathrm{K}}{\alpha'^2}\frac{k_\mathrm{B}T}{h\gamma_\mathrm{tot}}\left(\frac{\Delta E_0}{\varepsilon_0}\right)^2\frac{\omega^2+\gamma_\mathrm{tot}^2}{\omega^2}\cosh^2\left(\frac{\Delta E_0}{2k_\mathrm{B}T}\right). \quad (92)$$

For comparison, the resistance of the inter-dot tunnel barrier is $R_\mathrm{T} = 2R_\mathrm{K}k_\mathrm{B}T/(h\gamma_\mathrm{C})$[82].

In Fig. 14, we show the functional dependence of these different components. We start with the Sisyphus dissipation which is proportional to R^{-1}_SIS and see that it presents two symmetric maxima at finite detuning that increase with temperature (panel (a)). Furthermore, when the system is driven at constant frequency, $\omega = \omega_0$, the dissipation presents a maximum when the effective relaxation rate coincides with the driving frequency (panel (b)). Finally, at a fixed relaxation rate, $\gamma_\mathrm{tot} = \gamma^0_\mathrm{tot}$, the dissipation increases asymptotically as the driving frequency increases. The asymmetry between ω and γ_tot can be understood by noting that although dissipation in each cycle decreases as ω is increased, the overall number of cycles increases, exactly matching the reduction of energy dissipation per cycle. The Sisyphus cycle, as explained in Section III E, is driven by phonon pumping (Fig. 13(c), process 2).

Now, we focus on the quantum and tunneling capacitance and their sum, the parametric capacitance C_par. In panel (d), we show how they depend on detuning in the low and high temperature limits (left and right panels, respectively). In the low-T limit, the parametric capacitance (black) has a single peak centered at $\varepsilon_0 = 0$ and contains exclusively contributions from the quantum capacitance (dashed blue). In the high-T regime, the parametric capacitance (black) still has a single peak, although of reduced height due to the reduced equilibrium polarization in the energy basis. However, the peak now consist of contributions from both C_Q and C_TU in blue and red, respectively, the latter is responsible for the increased linewidth. The lineshape of C_TU coincides with that of the Sisyphus dissipation indicating that the same mechanism, phonon pumping, drives the process. However, when we explore the dependence of the capacitance on $\gamma_\mathrm{tot}/\omega_0$ and $\omega/\gamma^0_\mathrm{tot}$, we observe subtle differences. In panels e and f, we see that C_Q (blue) does not depend on the drive frequency. On the other hand, C_TU (red), and hence C_par, increases with increasing $\gamma_\mathrm{tot}/\omega$ in a symmetric way, see panels (e-f). With these three plots, we can get a comprehensive picture of the dispersive response. The quantum capacitance is linked to isentropic charge polarization due to the nonlinearity of the discrete energy levels of the DQD, whereas the tunneling capacitance is linked to thermal probability redistribution (maximal entropy production). The latter depends strongly on the system dynamics, i.e., it only manifests when γ_tot is comparable to or larger than ω; this is when tunneling occurs either nonadiabatically (as in the case of the Sisyphus heating) or adiabatically. In the specific case that γ_tot and ω are comparable, the Sisyphus and tunneling capacitance processes are linked to phonon pumping[114,115] and lead to net power dissipation.

In short, radio-frequency reflectometry can be used to probe additional components in the high-frequency response of low-dimensional systems. More particularly, we have learned that near the charge degeneracy point, a DQD behaves effectively as a variable capacitor (composed of the parallel sum of the quantum, tunneling capacitance and constant geometrical capacitance) in parallel with a variable resistor (the Sisyphus resistance).

C. Dispersive readout of QDs

Dispersive readout is based on measuring capacitance changes in quantum devices via rf-reflectometry techniques. It is ideal for applications where electrical transport measurements may not be possible. Dispersive techniques can be implemented with fewer electrodes than required for conventional dissipative sensors based on measuring two terminal conductance, such as the rf-QPC or the rf-SET. For that reason, they have gained considerable traction in spin-based quantum computing, where scaling is an important challenge. We note that, although motivated by developments in QD

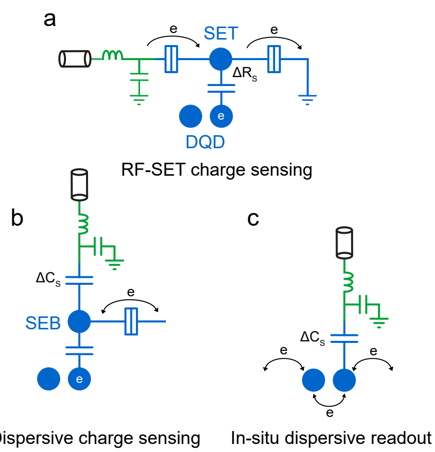

FIG. 15. Schematics of the three main reflectometry sensing techniques to probe the charge occupation of DQDs. (a) An rf-SET charge sensor detects the charge occupation of a DQD by measuring changes in the SET channel resistance ΔR_S. (b) Dispersive charge sensing detects the charge occupation of a DQD by measuring changes in the tunneling capacitance C_{TU} of a SEB induced by changes in the charge configuration of the DQD. (c) *In-situ* dispersive readout measures directly changes in the capacitance of the DQD due to bistable tunneling between QDs or between a QD and charge reservoir.

science and technology, dispersive readout techniques can be used to measure varying capacitance in generic quantum devices. To put dispersive readout techniques in perspectives, we present Fig. 15, summarising the three main techniques used to probe the quantum state in QD systems using rf-reflectometry: dissipative and dispersive charge sensing (panel a and b, respectively) and *in-situ* dispersive readout (panel c). Dissipative charge sensing, exemplified by the rf-SET, utilizes the variable resistance of the SET to detect the charge states of a coupled DQD. The sensor is coupled to two charge reservoirs. Dispersive charge sensing uses the variable capacitance, in this case of a single-electron box (SEB), to detect the charge state of a coupled DQD. In this case, the sensor needs to be coupled only to one charge reservoir. The resonator can be connected to gate or reservoir of the SEB. And finally, *in-situ* dispersive readout detects directly the state-dependent capacitance of the DQD and requires no sensor apart from the coupling gate. In Supplementary Table SI, we have benchmarked the three different methods utilizing available data in the literature. Here, we explain dispersive charge sensing and *in-situ* dispersive readout using some examples from the literature.

1. Dispersive charge sensing

An interesting approach to measure the charge occupation in QD arrays is to combine charge sensing techniques (see Section III B 2) with dispersive readout. This is the case of the single-electron box (SEB)[116–122]. The SEB (or single-lead quantum dot) is a charged island with only one connection to a lead (rather than two for SETs) and is capacitively coupled to one or more gates[65,66]. Cyclic tunneling between the island and the reservoir results in an effective capacitance that can be calculated analytically for the case in which the island and the reservoir present a zero- and three-dimensional density of states, respectively [82,123]

$$C_{\mathrm{TU}}^{0D} = \frac{(e\alpha)^2}{4k_{\mathrm{B}}T}\frac{\gamma_0^2}{\gamma_0^2+\omega^2}\cosh^{-2}\left(\frac{\varepsilon_0}{2k_{\mathrm{B}}T}\right), \tag{93}$$

where γ_0 is the dot-reservoir tunneling rate at the charge degeneracy point, ε_0 is the bias point and ω is the probing angular frequency. Recall the relation, $\varepsilon = \alpha(V_{\mathrm{G}} - V_{\mathrm{G}}^0)$. Equally, the capacitive response of a charged island with a 3D density of states can be calculated analytically,

$$C_{\mathrm{TU}}^{3D} = \frac{(e\alpha)^2}{k_{\mathrm{B}}T}\frac{R_{\mathrm{K}}}{R_{\mathrm{T}}}\frac{\varepsilon_0}{h\gamma}\frac{\gamma^2}{\gamma^2+\omega^2}\sinh^{-1}\left(\frac{\varepsilon_0}{k_{\mathrm{B}}T}\right), \tag{94}$$

where

$$\gamma = \frac{R_{\mathrm{K}}}{R_{\mathrm{T}}}\frac{\varepsilon_0}{h}\coth\left(\frac{\varepsilon_0}{2k_{\mathrm{B}}T}\right). \tag{95}$$

SEBs find applications in QD arrays where for example, the dots at the edge of the array in proximity to contact leads can be used as SEB charge sensors[118–121,124] (Fig. 16(a)). SEB charge sensors are sensitive detectors of the electrostatic environment. When the occupation of a nearby QD changes, the SEB island potential shifts, which in turn produces a change in capacitance that can be detected by gate reflectometry measurements. Whereas QPCs or SETs require two leads, SEB charge sensors require only one. This means they take up less space, which is an advantage in quantum circuits[125–131] and provide an interesting direction forward for scalable quantum electronics circuits.

Figure 16 shows a 2×2 array of QDs in which each dot is primarily controlled by one gate[119]. The readout technique employs the QD tunnel-coupled to the source electrode at the edge of the array, as a SEB charge sensor. The *LC* resonator is coupled to this QD (Fig. 16(b)). Gate reflectometry readout detects a phase change at the dot-to-reservoir transition due to the increased tunneling capacitance (Fig. 16(c)). When the occupation of one of the neighbour dots changes, the dot-to-reservoir transition line shifts by a small amount ΔV in the gate voltage space. By tuning the SEB near a dot-to-reservoir transition, the reflectometry phase signal becomes highly sensitive to the change of occupation of the nearby dot in a similar manner to SET charge sensors (Fig. 16(d)).

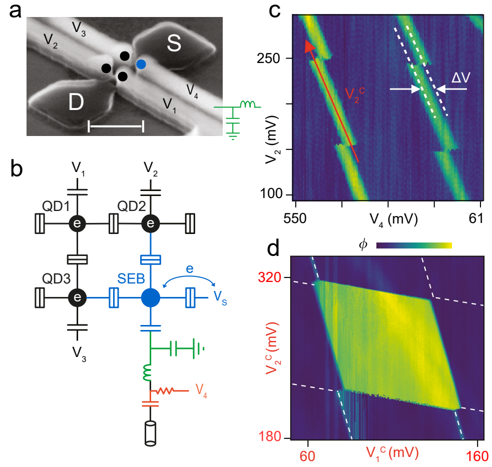

FIG. 16. (a) SEM of a 2×2 QD array in a double split-gate fully-depleted silicon-on-insulator (FD-SOI) transistor[119]. Gate 4 is wire-bonded to an rf resonator. The scale bar is 200 nm. The position of each QD is indicated by circle, with SEB in blue, sensed dots in black. (b) Circuit schematic showing the *LC* resonator attached to the SEB charge sensor and probing the other QDs of the array. The gate voltage V_4 is applied via a bias tee. The arrows represent the tunneling of charges. (c) Phase response ϕ of the gate reflectometry measurement as gates V_2 and V_4 are swept, revealing peaks at the dot-to-reservoir transitions of the SEB[119]. ΔV indicates the shift of the SEB peaks due the change of occupation of QD2. We also indicate the definition of a compensated control voltage, V_2^C, that changes the potential of QD2 without changing the potential of the SEB. (d) Phase response of the SEB as a function of two compensated control voltages V_2^C and V_1^C defined similar to that in panel (c)[119]. In this case, a hexagonal charge-stable region of the QD1-QD2 DQD is clearly visible. Fabio Ansaloni, Anasua Chatterjee, Heorhii Bohuslavskyi, Benoit Bertrand, Louis Hutin, Maud Vinet, Ferdinand Kuemmeth, Nature Communications, 11, 6399 (2020); licensed under a Creative Commons Attribution (CC BY) license.

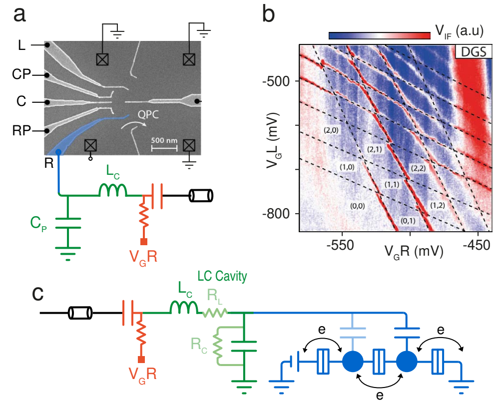

FIG. 17. (a) Micrograph of a GaAs DQD with an *LC* resonator attached to one of its gates. The *LC* resonator is composed of a superconducting inductor ($L_C = 210$ nH) and the parasitic capacitance ($C_P = 0.2$ pF). (b) Reflected voltage V_{out} as a function of voltages V_GL and V_GR applied to gates L and R. The charge occupation of each dot is indicated in brackets. Bright features indicate the regions of charge bistability. Reproduced with permission from Phys. Rev. Lett. 110, 046805 (2013). Copyright 2013 American Physical Society. (c) Circuit equivalent of *LC* resonator attached to one gate of a DQD. The arrows represent the types of tunneling to which the measurement is sensitive: tunneling between to and from the leads, and tunneling between dots.

Going forward, with the number of QDs in arrays increasing, it may become difficult to bring a sizable number of lead electrodes to create SEB charge sensors without disturbing the connectivity of the QD array. An approach that could overcome this challenge in the short term could be the use of floating gates to capacitively couple one of the QDs in an array to a remote sensor[121]. We note that this approach can be applied to any type of charge sensor described in this review.

2. *In-situ* dispersive readout

Figure 17 shows an example of *in-situ* dispersive readout performed on a GaAs gate-defined DQD[89]. The rf resonator is connected directly to one of the gate electrodes that controls the electrostatic potential of a QD. The measurement circuit (Fig. 17(a)), works on the principle explained in Section IV A and can be sensitive to both the capacitive and resistive contributions from the device. Measuring the demodulated signal as a function of the gate voltages that control the energy levels in the two dots shows the characteristic honeycomb pattern of double dot Coulomb blockade (Fig. 17(b)). Each type of charge transition (top dot-to-lead, bottom dot-to-lead, and dot-to-dot; see Fig. 17(c)) appears as a series of high-intensity lines in the plot, with a slope determined by the relative lever arms to the two gates. These lines mark locations in gate space at which electrons can tunnel cyclically in response to the rf gate voltage, which through the combination of C_Q, C_{TU}, and R_{SIS} loads the resonator and therefore changes the reflected voltage. The intensities of different lines arise from the different response of particular transitions to the rf voltage; as expected, the transitions of the bottom dot are stronger because of the larger gate coupling and hence lever arm.

3. Sensitivity and state of the art

The first demonstration of *in-situ* dispersive readout was reported in 2010 with an *LC* resonator attached to a lead of a GaAs DQD[85]. A minimum integration time of $\tau_{int} = 4$ ms was needed to discern the charge of a single electron tunneling between QDs with a signal to noise ratio of 1. Since then, several works have demonstrated a similar methodology[32,90,132,133] showing detection of regions of charge bistability when a tunnel rate, either of a dot-to-lead or dot-to-dot transition, is larger than the overall tunnel rate through the structure.

In 2013, dispersive readout with a *LC* resonator attached to a gate was first demonstrated using a GaAs DQD[89]. To discern dot-to-lead charge transitions, the authors required a minimum integration time of $\tau_{\rm min} = 39$ µs. From these results, it becomes apparent that the lever arm of the sensing gate to the specific transition to be sensed is a primary factor in $\tau_{\rm min}$, as shall be discussed in Section V. The latter work opened the path to more advanced *in-situ* dispersive readout demonstrations based on an enhanced gate lever arm[82] and optimized resonator topologies[134] meaning that a dot-to-lead transition could be discerned within a time $\tau_{\rm min} = 12.5$ ns.

After that, single-shot readout of spin qubits in silicon QDs via *in-situ* dispersive readout[112,135] of dot-to-dot charge transitions was performed. More recently, a DQD was coupled to a superconducting microwave cavity to obtain $\tau_{\rm min} =$ 170 ns[136], see Section VIII. Finally, readout of interdot charge transitions has been further improved to allow $\tau_{\rm min} = 80$ ns[137] and then $\tau_{\rm min} = 10$ ns[138] by using a Josephson parametric amplifier (see Section VI) and by adapting the resonator topology to increase the quality factor (see Section V B), respectively.

With regard to dispersive charge sensing, the SEB's capacitance is read using the same methodology as *in-situ* dispersive readout. It is hence expected that the aforementioned approaches could be used to achieve similar $\tau_{\rm int}$ when charge sensing events shift the sensor from a capacitance peak to the background. So far, SEBs charge sensors have allowed measurements of charge occupation with SNR = 1 in 550 ns integration time[66], charge detection in silicon nanowire QDs[119,139] and single-shot spin readout in less than 1 µs[140].

The recent progress on dispersive readout shows that, with an adequate resonator design, dispersive signals (either for *in-situ* dispersive readout or dispersive charge sensors) can approach the signal levels of dissipative sensors (see Sec V). Under certain conditions, *in-situ* dispersive sensing and SEBs could achieve comparable or even faster readout. One reason is that SETs are intrinsically shot noise-limited with values for typical bias conditions approaching or even exceeding the noise of cryogenic amplifiers (see Section VI). Dispersive readout is Sisyphus noise-limited[82], noise that can be made comparatively smaller than the noise temperature of cryoamps[141] and hence allows quantum-limited amplifiers to achieve lower noise temperatures[137] (see Section VI).

V. OPTIMIZATION OF RADIO-FREQUENCY RESONATORS

The optimization of a radio-frequency resonator has the purpose of reducing the time required to perform a measurement or in other words, of increasing the SNR. In rf reflectometry, the signal corresponds to the difference in reflected voltage between the two states to be measured, so that

$$\begin{aligned}\mathrm{SNR} &= \left|(\Gamma_{\rm b}-\Gamma_{\rm a})\frac{V_0}{V_{\rm N}}\right|^2 \\ &= |\Delta\Gamma|^2\frac{P_0}{P_{\rm N}},\end{aligned} \tag{96}$$

where V_0 (P_0) and $V_{\rm N}$ ($P_{\rm N}$) are the input and noise voltage (power) respectively, and $\Gamma_{\rm a(b)}$ are the reflection coefficients corresponding to the two states to be measured. Maximizing the SNR entails two objectives: (i) maximizing the change in reflection coefficient between states for a given input power, (ii) minimising the noise power.

The task of minimising the noise is discussed in Section VI. In this section, we shall describe strategies to maximise the signal by optimising the radio-frequency circuit. From Eq. (96), it is clear that the SNR can be increased by maximizing $|\Delta\Gamma|$ at a given input power. The strategy that should be followed to optimise $|\Delta\Gamma|$ depends on the type of device to be measured (resistive or reactive) and on the size of the signal change (small or large-signal regime).

A. Optimising for changes in resistance

Figure 18 shows a simulation of $|\Gamma(R_{\rm S})|$ as a function of a variable resistance $R_{\rm S}$ embedded in an ideal *LC* resonator (see Section III). The point $|\Gamma(R_{\rm S})| = 0$ marks the critical coupling condition. Optimising the resonator consists of maximising the change in $\Delta\Gamma$ for a given change in resistance $\Delta R_{\rm S}$. In the analysis of this problem, we need to distinguish two cases: $\Delta R_{\rm S}/R_{\rm S} \ll 1$ (the small-signal regime) and $\Delta R_{\rm S}/Rs \approx 1$ (the large-signal regime).

1. Resistive readout - The small-signal regime

For small resistance changes $\Delta R_{\rm S}$, the change in reflection coefficient can be calculated to first order as

$$\Delta\Gamma = \left.\frac{\partial\Gamma}{\partial R_{\rm S}}\right|_{\omega=\omega_{\rm r}}\Delta R_{\rm S}. \tag{97}$$

For the circuit in Fig. 18, this takes the form:

$$\Delta\Gamma \approx \frac{2Z_{\rm load}Z_0}{(Z_{\rm load}+Z_0)^2}\frac{\Delta R_{\rm S}}{R_{\rm S}}. \tag{98}$$

The first ratio in Eq. (98) relates to the circuit coupling, which is maximal when the equivalent impedance of the circuit at resonance, $Z_{\rm load}$, is equal to the impedance of the line Z_0. The second ratio, $\Delta R_{\rm S}/R_{\rm S}$ is maximal when the fractional changes in resistance are maximised. Figure 18 illustrates that $\Delta\Gamma$ is maximal near the critical coupling condition, as expected from Eq. (98).

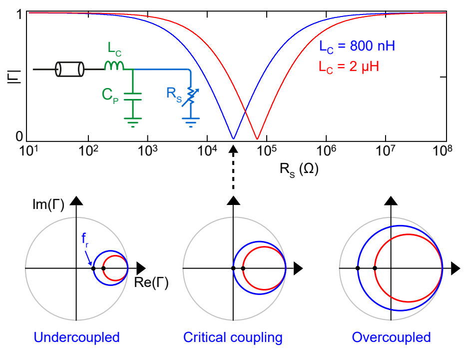

FIG. 18. Top: Reflection coefficient amplitude $|\Gamma(R_S)|$ simulated for the LC circuit in the inset with $L_C = 800$ nH and $f = 229.4$ MHz (blue trace), and with $L_C = 2$ μH and $f = 145.2$ MHz (red trace); $C_P = 0.6$ pF. Critical coupling is reached at a specific value of R_S that depends on the circuit parameters. Bottom: Smith charts of the reflection coefficient spectrum (see Fig. 5). The black dots indicate the resonance frequency. The resonator is undercoupled for low values of R_S (left) and overcoupled for high values (right). At critical coupling (blue curve middle), the curve runs through the origin.

2. *The matching capacitor and in-situ tuneable resonators to achieve critical coupling*

As explained in Section III, critical coupling for an LC resonator attached to a resistive device is achieved when $R_S = R_{\text{match}} = L_C/C_P Z_0$ (Eq. (46)). If R_S and C_P are known, a user can choose L_C to obtain the best sensitivity. However, in practice it is not easy to know these values precisely because they depend on temperature and because the parasitic capacitance is uncertain. Moroever, Eq. (46) implies that a large L_C is required to match samples with large resistances and parasitic capacitances. Increasing of L_C reduces the readout bandwidth ((22)); more problematically, large surface-mounted inductors introduce self-resonances near the operating frequency[142]. This is a difficulty for many quantum devices, which typically have resistance $R_S \gtrsim 100$ kΩ. Even with careful engineering, sample wiring typically contributes a sample capacitance $\gtrsim 0.3$ pF in parallel with the device[143]. A matching capacitor C_M, in parallel with the circuit, allows us to shift the critical coupling to a higher value of R_S to enable $Z_{\text{load}} = Z_0$.

Voltage-tunable capacitors (varactors) allow for *in situ* tuning of the matching condition[59]. Varactors in parallel with the sample can also be used to tune the resonance frequency. An example of *in situ* tunable resonator with a matching capacitor[144] is illustrated in Fig. 19(a). This circuit incorporates two varactors: one primarily for impedance matching (C_M) and one primarily for frequency tuning (C_t). The varactors allow the capacitance to be tuned with a dc voltage. Fig. 19(b) shows a simulation of the reflection coefficient Γ as a function of frequency for typical device parameters with no matching capacitor ($C_M = 0$). Tuning C_t allows changing the resonance frequency

$$f_r = \frac{1}{2\pi\sqrt{L_C(C_t + C_P)}} \tag{99}$$

as well as modifying the coupling. In this example, critical coupling is achieved at $C_t + C_P = 0.14$ pF which is below the typical parasitic capacitance of the measurement set up. Hence C_t on its own does not allow for critical coupling to be achieved. However, by increasing the capacitance of the matching capacitor C_M, critical coupling can be achieved for a larger range of C_t and R_S values. The matching capacitor has little effect on the resonance frequency, but modifies the resonator's impedance and thus the circuit coupling in the circuit of Fig. 19 as follows:

$$Z_{\text{load}} = \frac{C_{\text{tot}}^2 L_C R_S}{C_M^2 L + C_{\text{tot}}^3 R_S^2} \tag{100}$$

where $C_{\text{tot}} = C_M + C_t + C_P$. Controllable perfect matching with resistive devices such as rf-QPCs[59–61,145] and rf-SETs[144] is thus possible. Typically GaAs varactors are used[7,144] because they are widely tuneable down to 1 K. However, at lower temperature the tuning range is drastically less[7]. A list of components used in various studies cited in this review is available as Supplementary Table SII.

3. *The large-signal regime*

For large resistive changes, for example when a charge sensing event shifts an SET from a Coulomb peak to a valley, the first order approximation of Eq. (97) breaks down. Instead we must consider $\Delta\Gamma = \Gamma(R_b) - \Gamma(R_a)$, the change in the reflection coefficient given a resistance change from R_b to R_a. Circuit losses are generally detrimental, but become particularly important in the large-signal regime.

Losses in the inductor (caused by its resistance R_L) reduce $|\Gamma|$ when the device is in a highly resistive state (Fig. 20). As a result, the maximum $|\Delta\Gamma|$ when the device resistance increases above the match value is reduced to

$$|\Delta\Gamma|_{\max} = \left|\frac{R_L - Z_0}{R_L + Z_0}\right| \tag{101}$$

for $R_L < Z_0$. For $R_L > Z_0$ achieving critical coupling is not possible. The goal is thus to minimize R_L. Superconducting inductors are a way forward (see Section V B 3).

Capacitive losses (R_C) have a similar effect (Fig. 20). These losses, as they are in parallel with the device resistance, reduce the maximum achievable $|\Delta\Gamma|$ between the two resistive states to

$$|\Delta\Gamma|_{\max} = \left|\frac{\frac{L_C}{C_p R_C} - Z_0}{\frac{L_C}{C_p R_C} + Z_0}\right| \tag{102}$$

for $R_C > R_{\text{match}}$. For $R_C < R_{\text{match}}$, critical coupling is not achievable. In order to minimize R_C, low-loss dielectrics and high-resistance device gate oxides can be used[146].

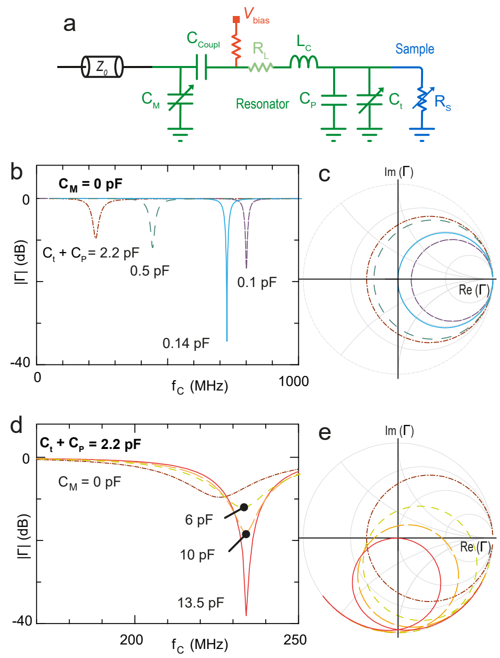

FIG. 19. (a) A device is coupled to an impedance matching network formed from an inductor, variable capacitors C_t and C_M, and fixed capacitor. Parasitic losses are parameterized by an effective resistance R_L. (b,c) Simulation with no matching capacitor ($C_M = 0$)[144]. Voltage reflection coefficient Γ is plotted as a function of frequency for different values of sample capacitance C_P, as magnitude (b) , and as a Smith chart (c). $R_L = 20\ \Omega$ takes into account the losses in the resonator. The sample resistance is $R_S = 1$ GΩ, and the capacitance of the device is included in C_P. The inductor value is $L_C = 223$ nH and C_{Coupl} is 87 pF. (d,e) Simulated reflection for varying the matching capacitor C_M[144]. Reproduced with permission from Phys. Rev. Applied 5, 034011 (2016). Copyright 2016 American Physical Society.

4. *Measurement back-action: Relaxation and dephasing*

Using rf-SETs to measure the state of a qubit causes two types of back-action: relaxation (i.e. random transitions between eigenstates) and dephasing (i.e. randomisation of the phase in superpositions)[42]. Various processes contribute to measurement-induced relaxation but the most widely considered in the literature are shot noise in the SET and quantum fluctuations in the qubit's environment[30]. The measurement-induced relaxation rate Γ_1 is proportional to the spectral density $S_{VV}(f)$ of the voltage fluctuations on the SET island at the qubit frequency[147]:

$$\Gamma_1 = \frac{1}{8}\left(\frac{e}{\hbar}\right)^2 \kappa^2 \frac{\Delta_C^2}{\Delta E^2}\, S_{VV}\left(\frac{\Delta E}{h}\right), \tag{103}$$

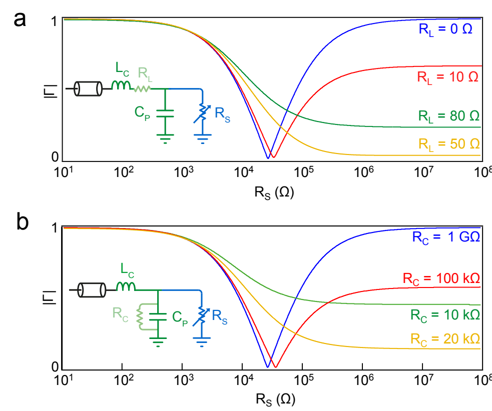

FIG. 20. Reflection amplitude $|\Gamma|$ as a function of sample resistance R_S considering losses in the inductor R_L (a) or in an effective resistance to ground R_C (b). The simulation parameters are $C_P = 0.6$ pF, $L_C = 800$ nH and $f = 229.4$ MHz. The blue curves correspond to an ideal LC resonator $R_L = 0$, $R_C = \infty$. The red curves correspond to modest losses that reduce the sensitivity of the circuit while the green and orange curves correspond to losses so high that the circuit is always undercoupled. Changes in $|\Delta\Gamma|$ as a function of R_S are reduced when the losses in the circuit increase. Note that values used for the green and orange curves, in both panels, are exaggeratedly bad compared to current experiments but are included for pedagogical purpose.

where the qubit Hamiltonian is Eq. (80) and the lever arm κ is the ratio between the qubit-SET capacitance and the total capacitance of the qubit, which determines how strongly the SET island voltage fluctuations couple to the qubit.

The shot-noise relaxation process dominates for low qubit frequencies, i.e. when $\Delta E/\hbar \ll I/e$ where I is the current through the SET. Using "orthodox" SET theory[148], the corresponding spectral density is

$$S_{VV}^{o}(f) = 4\frac{E_C^2}{e^2}\frac{4\omega_I}{(2\pi f)^2 + 16\omega_I^2} \tag{104}$$

where $\omega_I = I/e$ is the tunneling rate through the SET and E_C the SET charging energy. Equation (104) assumes a symmetric SET with no cotunneling.

The quantum-fluctuation process dominates at high frequency where $\Delta E \gg E_C$. This process is driven by the fact that every electromagnetic mode containing the SET has associated quantum fluctuations. Their total spectral density can be modelled by considering the impedance of the SET island to ground as two parallel tunnel junctions each with resistance R_T, giving

$$S_{VV}^{e}(f) = hf\frac{R_T}{1+\left(\frac{hf}{E_C}\frac{\pi R_T}{2R_K}\right)^2}. \tag{105}$$

To evaluate the noise spectral density of the SET island in all frequency regimes, a full quantum mechanical calculation is necessary[50].

The other type of back-action is measurement-induced dephasing, caused when voltage fluctuations modify the energy splitting between qubit states without driving transitions between them. The general expression for the dephasing rate is

$$\Gamma_\phi = \frac{1}{4}\left(\frac{e}{\hbar}\right)^2 \kappa^2 \frac{\varepsilon^2}{\Delta E^2} S_{VV}(0). \tag{106}$$

The SET approaches the quantum limit for qubit readout (given by the equality in the Heisenberg uncertainty principle, $\Gamma_\phi \tau_{\min} \geq 1/2$) but so far has not reached it[149]. Here $\tau_{\min}$ is the measurement time needed to discern the state of the qubit with a signal-to-noise ratio of 1.

B. Optimising for changes in capacitance

In this subsection, we describe analytically the SNR optimization problem for changes in device capacitance ΔC_S and provide experimental strategies to improve SNR. We show that the strategy depends on whether one is in the small-signal limit ($Q_\mathrm{r}\Delta C_\mathrm{S}/C_\mathrm{tot} \ll 1$) or the large-signal limit ($Q_\mathrm{r}\Delta C_\mathrm{S}/C_\mathrm{tot} \approx 1$).

1. Capacitive readout - The small-signal regime

In the small-signal regime, we consider capacitance changes only to first order by writing

$$\Delta\Gamma = \left.\frac{\partial \Gamma}{\partial C_\mathrm{S}}\right|_{\omega=\omega_\mathrm{r}} \Delta C_\mathrm{S}, \tag{107}$$

where ΔC_S is the change in the device capacitance. For the circuit topology of Fig. 21(a), we obtain

$$\Delta\Gamma \approx j\frac{2Z_\mathrm{load}Z_0}{(Z_\mathrm{load}+Z_0)^2} Q_\mathrm{int}\frac{\Delta C_\mathrm{S}}{C_\mathrm{tot}}, \tag{108}$$

where $Z_\mathrm{load} = L_\mathrm{C}/(C_\mathrm{tot}R_\mathrm{C})$ is the equivalent impedance of the circuit at resonance and $C_\mathrm{tot} = C_\mathrm{P} + C_\mathrm{S}$ is the total capacitance. The first ratio corresponds to the matching condition and is maximal when $Z_\mathrm{load} = Z_0$, as in the resistive case. The second factor is the internal quality factor of the resonator $Q_\mathrm{int} = R_\mathrm{C}\sqrt{C_\mathrm{tot}/L_\mathrm{C}}$ and the third is the fractional change in capacitance. In contrast to resistive readout (Eq. (98)), the internal quality factor plays a significant role[134]. Equation (108) sets the first guidelines for SNR optimization to capacitance changes: (i) good matching to the line, (ii) high internal quality factor and (iii) large fractional changes in capacitance. In other words, both the parasitic capacitance and the internal circuit losses need to be minimised (increase R_C) while achieving good coupling to the line. This can be equivalently seen as designing a high-Q, high impedance resonator. In the following, we explain possible strategies to achieve those goals.

2. Resonator topology

Considering the critical coupling condition $Q_\mathrm{int} = Q_\mathrm{ext}$ and the requirement to achieve high internal quality factors, improving the SNR to capacitance changes requires increasing Q_ext. The standard LC resonators used to couple to resistive devices have $Q_\mathrm{ext} = \sqrt{L_\mathrm{C}/C_\mathrm{tot}}/Z_0$, which is typically[150] well below 100. A new circuit topology is needed with the necessary degrees of freedom to achieve critical coupling while maintaining high quality factors. In one such design[134,137], the inductor is placed in parallel with the sample and coupled though a coupling capacitor C_Coupl to a coplanar waveguide (Fig. 21(c)). In this configuration, the external and internal quality factors are:

$$Q_\mathrm{ext} = \left(\frac{C_\mathrm{Coupl}+C_\mathrm{tot}}{C_\mathrm{Coupl}}\right)\frac{1}{Z_0}\sqrt{\frac{L_\mathrm{C}(C_\mathrm{Coupl}+C_\mathrm{tot})}{C_\mathrm{Coupl}^2}} \tag{109}$$

$$Q_\mathrm{int} = \sqrt{\frac{C_\mathrm{Coupl}+C_\mathrm{tot}}{L_\mathrm{C}}}R_\mathrm{C}. \tag{110}$$

By introducing the extra degree of freedom of C_Coupl, this topology enables Q_ext to be increased while maintaining similar Q_int. A circuit that introduced this design reached $Q_\mathrm{ext} = 680$ and $Q_\mathrm{int} = 943$ ($Q_\mathrm{r} \approx 400$) using a superconducting inductor [134]. The same paper reports $Q_\mathrm{r} = 790$ with another resonator. Later, a loaded quality factor of $Q_\mathrm{r} = 966$ was obtained[137], with a consequent improvement of the sensitivity. Further improvements have been achieved by using inductive coupling rather than capacitive coupling as demonstrated in Ref. 138. Inductive coupling removes the need to add C_Coupl, further increasing the fractional changes in capacitance.

3. Reducing the parasitic capacitance with superconducting inductors

The analysis of the SNR to capacitance changes concluded that is necessary to reduce both parasitic losses and capacitance. Superconducting inductors have two main advantages. Firstly, they minimise dissipative losses. Secondly, their planar geometry allows significantly smaller parasitic capacitance than in wire-wound surface-mount inductors. These advantages increase the internal quality factor Q_int and increase the fractional changes in capacitance. Conventional wirewound surface-mount inductors[135] do not exceed quality factors of 100 while air-core inductors go just above[7].

Typical superconducting inductors are planar spirals with a bonding pad at each end (Fig. 21(a,b)). They can be fabricated on a dedicated chip separate from the sample in order to allow for different fabrication strategies for each chip. They are typically made from thin films of the Type II superconductors Nb[89], NbN[135] or NbTiN[137]. Important considerations are the critical temperature and critical magnetic field of the thin film. For experiments requiring high magnetic fields, such as for spin qubits, NbN and NbTiN are suitable provided the field is in the plane of the film[134].

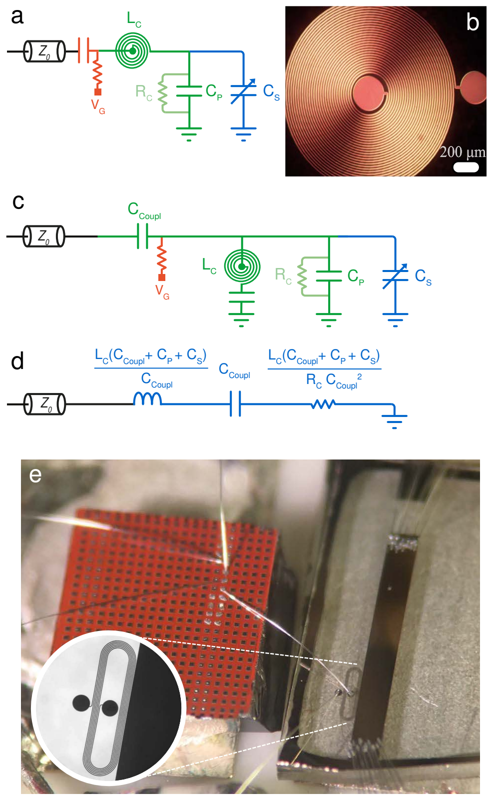

FIG. 21. (a) Conventional LC resonator circuit to measure a capacitance, similar to Fig. 12(a) but using a superconducting inductor L_C. (b) Photograph of a superconducting planar inductor. Reprinted figure with permission from 134. Copyright (2022) by the American Physical Society. (c) Schematic of a resonator with superconducting inductor in the parallel configuration. (d) Equivalent circuit at resonance. The resistance R_C represents the losses in the resonator. (e) Photograph of a multi-module set-up[138]. The silicon chip with an array of square bond-pads is seen to the left, and to the right is the NbN-on-sapphire substrate. The two modules are positioned on a printed circuit board. The inductor, an elongated spiral (magnified in inset), is inductively coupled to a 50 Ω waveguide. This circuit provided an inductance $L_C = 47$ nH and a parasitic capacitance $C_P = 0.15$ pF. David J. Ibberson, Theodor Lundberg, James A. Haigh, Louis Hutin, Benoit Bertrand, Sylvain Barraud, Chang-Min Lee, Nadia A. Stelmashenko, Giovanni A. Oakes, Laurence Cochrane, Jason W.A. Robinson, Maud Vinet, M. Fernando Gonzalez-Zalba, and Lisa A. Ibberson, PRX Quantum 2, 020315, 2021; licensed under a Creative Commons Attribution (CC BY) license.

Multi-module assemblies in which a semiconductor and superconducting chip are connected via wirebonds have been demonstrated (Fig. 21(d)). For example, in Refs. 138 and 151 the superconducting chip contains an elongated spiral inductor that is inductively coupled to a 50 Ω microstrip waveguide fabricated using optical lithography from 80 nm of sputtered NbN on a sapphire substrate.

To reduce parasitic capacitance further, careful rf engineering of the circuit board is essential. High-frequency signals should be delivered by PCB waveguides with 50 Ω characteristic impedance. Parasitic capacitances can be further reduced by fabricating the PCB board from low-loss dielectrics such as the RT/duroid 4000 and 5000 families[146].

4. On-chip superconducting microwave resonators

The quality factors of resonators mounted on a printed circuit board are ultimately limited by dielectric losses and by parasitic capacitance to the ground, which in turn is set by the size of the components and of wirebonds. To reduce C_P further, one must mount the resonator on the chip itself. This adds fabrication and integration complexity. Ultimately this approach is limited by the internal quality factor. For superconducting on-chip microwave resonators, the quality factor can be as large as a million[152,153], but when such resonators are incorporated into a spin qubit device, the quality factor is smaller because of losses in the semiconductor substrate ($Q_r \approx 2000$)[79,136,154,155]. However, on-chip resonators generally have substantially lower parasitic capacitance than in multi-module assemblies. As well as for spin qubits, they have also been used to measure nanomechanical resonators[156–159]. The reduction in parasitic capacitance allows operation in the microwave range, i.e. $f_r > 1$ GHz, where resonant interactions between the resonator and the device can occur. This regime where the energy of the resonator photons and the system to be probed are similar (also known as the resonant regime of circuit QED) is out of the scope of this review, but interested readers can find information in Ref. 10.

5. Device capacitance

In Section IV, we discussed the origin of quantum capacitance (Eq. (72)) and its manifestation in DQDs (Eq. (90)). The reader can see that the device capacitance depends on the lever arm α, which quantifies the efficiency of a gate in modifying the electrochemical potential. In semiconductor devices, α can be increased by: (i) using small equivalent gate oxide thicknesses, i.e. by using thin high-k dielectrics, (ii) using devices with a thin active region, such as on-insulator substrates[160] and (iii) using non-planar gate geometries as in carbon nanotubes[90], InAs nanowires[154], or silicon nanowire transistors[161]. Finally, quantum capacitance changes can be made more pronounced in low-dimensional devices by decreasing the temperature. Lower temperatures result in larger changes in the number of states with respect to changes in the chemical potential (in 1D and 2D systems).

6. Capacitive readout - The large-signal regime

Once the above strategies have been implemented, $Q_r\Delta C_S/C_{tot}$ may approach 1. This means we cannot apply Eq. (107) and must instead consider $\Delta\Gamma = \Gamma(C_b) - \Gamma(C_a)$, the change in reflection coefficient when the capacitance changes from state C_b to C_a. To calculate this difference, we consider the reflection coefficient of a parallel resonator geometry (Fig. 21(c)):

$$\Gamma = \frac{\Gamma_{min} + 2jQ_r\Delta\omega/\omega_r}{1 + 2jQ_r\Delta\omega/\omega_r}, \quad (111)$$

where ω_r is the resonance angular frequency, $\Delta\omega$ is the difference from the resonance frequency and Γ_{min} is the minimum value of the reflection coefficient. It can be shown that the difference in Γ between two capacitance states is maximal when $\mathrm{Re}(\Delta\Gamma) = 0$ and that this condition occurs when the operation frequency is mid-way between the resonant frequencies corresponding to the two states[138]. In this case

$$\Delta\Gamma = j\frac{Q_r\frac{\Delta\omega}{\omega_r}(1-\Gamma_{min})}{1+\left(2Q_r\frac{\Delta\omega}{\omega_r}\right)^2}. \quad (112)$$

Taking into account that $Q_r = Q_{int}/(1+\beta)$, $1-\Gamma_{min} = 2\beta/(1+\beta)$ and $\Delta\omega/\omega_r = \Delta C_S/C_{tot}$ where β is the coupling coefficient and C_{tot} now includes C_{Coupl}, we arrive at the general expression for $\Delta\Gamma$:

$$\Delta\Gamma = j\frac{\frac{2\beta}{(1+\beta)^2}Q_{int}\frac{\Delta C_S}{C_{tot}}}{1+\left(Q_r\frac{\Delta C_S}{C_{tot}}\right)^2}. \quad (113)$$

In the small-signal limit $Q_r\Delta C_S \ll 1$, we recover Eq. (108). Furthermore, we see that $\Delta\Gamma$ becomes maximal when $Q_r\Delta C_S = 1$. This condition translates into

$$\Delta\omega = \frac{\omega_r}{Q_r} = 2\pi B_f, \quad (114)$$

where we have to consider that the system is probed at the average resonant frequency of the two measurement outcomes[138]. For a given device-induced frequency shift, the best strategy is to couple the resonator such that its bandwidth will match this frequency shift. This is known as the condition for maximum state visibility. Under these circumstances

$$\Delta\Gamma = j\frac{2\beta}{1+\beta}, \quad (115)$$

and hence, if a large enough frequency shift is available, overcoupling the resonator to the line will result in higher $\Delta\Gamma$ compared to the small-signal regime, where critical coupling is optimal.

7. Optimal SNR and back action

From Eq. (96), one might conclude that increasing the input power P_0 results in an indefinite increase in SNR. However, P_0 cannot be arbitrarily large since eventually the large voltage swing across the device will broaden the lineshape of the feature under study, i.e. create back-action by over-driving the system. This voltage scale might correspond, for example, to an energy swing equivalent to an energy-level splitting in a DQD, or to the energy associated with the tunneling rate or the electron temperature for a SEB. To study this problem, we divide the task in two: (i) understanding the effect of the voltage drop at the device V_{dev} on the observable capacitance ΔC_S and (ii) determining V_{dev} given an input power P_0.

Point (i) has been considered in literature for charge, spin and Majorana devices using the adiabatic approximation[162]. Here, we use the simplest example: a charge qubit, i.e. a coupled DQD as in Section IV B 2. In the adiabatic limit, where probe-induced excitations and inelastic relaxation processes can be neglected, the charge on QD2 (the dot which we take as a reference) can be expressed as:

$$n_2 = \frac{1}{2}\left(1+\frac{\varepsilon}{\Delta E}\right) \quad (116)$$

where ε is the energy detuning between QDs and ΔE the DQD energy difference. The effective parametric capacitance of the DQD is the ratio between the in-phase Fourier component of the charge response and the Fourier component of the probing voltage during the time T, both taken at the probe frequency and weighted by the probing gate lever arm α:

$$C_Q = \frac{\frac{1}{T}\int_0^T \alpha e n_2(t)\sin(\omega t)dt}{\frac{1}{T}\int_0^T V_{dev}\sin(\omega t)\sin(\omega t)dt}. \quad (117)$$

The denominator is readily found to equal $V_{dev}/2$. Considering that $n_2(t)$ is periodic in time, we find

$$C_Q = \frac{2\alpha e}{V_{dev}}\frac{1}{T}\int_0^T n_2(t)\sin(\omega t)dt. \quad (118)$$

Equation (118) can be solved analytically after inserting Eq. (116) to yield

$$C_Q = \frac{2\alpha e}{\pi V_{dev}} f_C(x). \quad (119)$$

Here the dimensionless function characterizing the capacitance is defined as

$$f_C(x) = \frac{(1+x^2)\,E\left(\frac{x^2}{1+x^2}\right) - K\left(\frac{x^2}{1+x^2}\right)}{x\sqrt{1+x^2}}, \quad (120)$$

where $x = \alpha e V_{dev}/\Delta_C$ and $K(x)$ and $E(x)$ are complete elliptic integrals of the first and second sides respectively. We can now evaluate the effect of increasing V_{dev} on the capacitance amplitude. At low voltages, $f_C(x) \to \frac{\pi}{4}x$ and we recover the expected function for the ground state capacitance in the small excitation regime (see Eq. (90))

$$C_Q = \frac{(\alpha e)^2}{2\Delta_C} \quad (121)$$

whereas for large voltages, $f_C(x) \to 1$, and the capacitance becomes a decreasing function of V_{dev}. We can see how overdriving leads to back-action by reducing the measured capacitance.

Next, we move to point (ii), which requires calculating the relationship between P_0 and $V_{\rm dev}$. We consider the parallel circuit configuration (see Section V B 2). Suppose that all the power dissipated in the tank circuit is dissipated across the effective resistance $R_{\rm C}$ (i.e. that $R_{\rm L}$ is negligible). By energy conservation, we have

$$\frac{V_{\rm dev}^2}{R_{\rm C}} = (1-|\Gamma|^2)P_0 \tag{122}$$

where P_0 is the incident power and $V_{\rm dev}$ is the voltage across the device. Substituting from Eq. (10) and rearranging gives

$$P_0 = \frac{V_{\rm dev}^2}{R_{\rm C}}\frac{(Z_{\rm load}+Z_0)^2}{4Z_{\rm load}Z_0}. \tag{123}$$

We can now go back to our definition of SNR (Eq. (96)) and insert Eqs. (108), (119), and (123) to find:

$$\mathrm{SNR} = \frac{8}{\pi^2}\frac{\beta}{(1+\beta)^2}\frac{(\alpha e)^2}{k_{\rm B}T_{\rm N}}\frac{Q_{\rm int}\omega_{\rm r}}{C_{\rm tot}} f_{\rm C}^2\left(\frac{\alpha e V_{\rm dev}}{\Delta_{\rm C}}\right)\tau_{\rm int}, \tag{124}$$

where we have used the fact that $P_{\rm N} = k_{\rm B}T_{\rm N}/2\tau_{\rm int}$, with $\tau_{\rm int}$ being the effective integration time. Equation (124) provides clear guidelines on the optimal steps to maximise the SNR: (i) Achieve critical coupling, (ii) increase the internal quality factor i.e. reduce internal losses, (iii) reduce parasitic capacitance, (iv) operate at high frequency, (v) maximise the lever arm α, (vi) reduce the noise temperature and obviously (vii) increase the illumination level $V_{\rm in}$ and (viii) increase the integration time. One should keep in mind that some of these parameters affect the voltage drop across the device, i.e. $V_{\rm dev} = 2C_{\rm Coupl}Q_{\rm r}V_{\rm in}/(C_{\rm Coupl}+C_{\rm P})$, and $V_{\rm in}$ may need to be readjusted to avoid overdriving the system.

For singlet-triplet spin qubits (Section IX), Ref. 162 shows that the SNR in a dispersive readout experiment also saturates as $V_{\rm in}$ is increased. For Majorana qubits (see Section IX), the model predicts an optimal $V_{\rm in}$, with a decreasing readout fidelity as $V_{\rm in}$ is increased beyond this optimum.

8. Resonator-induced dephasing

Any readout method is bound by the Heisenberg uncertainty principle that poses constraints on sensitivity and back-action. For qubit readout, the measurement time needed to acquire the state of a qubit with a signal-to-noise ratio of 1, $\tau_{\rm min}$, is related to the induced rate of dephasing Γ_ϕ by the following relation

$$\Gamma_\phi\tau_{\rm min} \geq 1/2, \tag{125}$$

meaning that a measurement completely dephases the qubit and the rate at which it does so is at least $1/(2\tau_{\rm min})$. If the readout method follows the equality, it is said to have a quantum efficiency of 1. The problem of induced dephasing using dispersive readout has been analysed in Ref. 163 for a slow oscillator ($\omega_{\rm r}$ much smaller than the characteristic discrete energy level spacing in the qubit) which is the common case for rf reflectometry. For a wide range of parameters, dispersive readout is found to have unit quantum efficiency.

Another important consideration is the rate of dephasing induced by the measurement system when it is not measuring $\Gamma_\phi^{\rm off}$, i.e. not being driven by an external rf tone. The rate of induced dephasing for a thermally occupied oscillator is

$$\Gamma_\phi^{\rm off} = n(\omega_{\rm r})\left[1+n(\omega_{\rm r})\right]Q_{\rm r}\frac{\Delta C_{\rm S}^2}{C_{\rm tot}^2}\omega_{\rm r}, \tag{126}$$

where $n(\omega_{\rm r}) = 1/\left(e^{\hbar\omega_{\rm r}/k_{\rm B}T}-1\right)$ is the thermal occupation number at the resonator frequency. To minimize off-state dephasing, it is advantageous to cool down the resonator – either by increasing the frequency or lowering its physical temperature – but it also to reduce the fractional change in capacitance and to use a low-Q resonator. Since some of these conditions compete against the SNR optimization strategies presented above, SNR and $\Gamma_\phi^{\rm off}$ need to be evaluated simultaneously to reduce the readout time while maintaining low dephasing rates.

C. Large gated semiconductor devices

Large gated semiconductor devices are difficult to match because of their large capacitance, but nevertheless, dissipative rf measurement measurements of 2D systems have been achieved[142]. However, accumulation-mode quantum dots remain a challenge because the resistance of the contact leads and capacitance of the large accumulation gate form an RC filter that prevent the signal from reaching the quantum dot[164]. This problem can be mitigated with device designs that minimise the accumulation region[74] or by using doping instead of gates to fabricate the leads[165].

Another approach, which requires less optimisation, is to connect the resonator to an accumulation gate. Thanks to the high gate capacitance, the reflected signal is sensitive to the resistance of the quantum dot rather than only its capacitance[164,166]. In this configurations the path that would allow the signal to leak directly from the contact lead to ground needs to be blocked by a resistor[166] or using gates[164].

In dispersive measurements, the accumulation of charges in the surroundings of the quantum dot creates a voltage-dependent change of $C_{\rm P}$ that degrades the sensitivity[167,168]. This unwanted accumulation of charge in the areas surrounding the quantum dot can be reduced by using depletion gates[168].

D. The charge sensitivity

Comparing the performance of different sensing devices including dissipative and dispersive methodologies is essential in assessing the quality of a particular readout technology. Different figures of merit have been used in the literature to benchmark readout sensors but all can be related to a single magnitude, the minimum measurement time $\tau_{\rm min}$, defined as the integration time needed to discern two states with a SNR of 1.

For charge sensors, the most commonly used figure of merit is the charge sensitivity $\sqrt{S_{QQ}^{\mathrm{N}}}$, which can be understood as the amount of charge that can be discerned in a measurement lasting a second (see Eq. 50). In this case, the minimum measurement time corresponds to

$$\tau_{\min} = \frac{S_{QQ}^{\mathrm{N}}}{2e^2}. \tag{127}$$

In radio-frequency mode, the charge sensitivity of a sensor can be extracted in two ways:

(i) In the frequency domain (see Fig. 22(a,b)), by applying to a device electrode a small sinusoidal signal of frequency f_{m} and calibrated charge rms amplitude (typically $\Delta q_{\mathrm{rms}} = 0.01e$ or less to guarantee that the sensor operates in the linear regime). This method is particularly useful for SETs where the gate voltage period is a direct measurement of the addition of one unit of charge. If the device is biased at a point of finite transconductance, the ac signal modulates the carrier frequency f_{in} producing sidebands in the power spectrum of the reflected signal at $f_{\mathrm{in}} \pm f_{\mathrm{m}}$ (Fig. 22(c)). The sensitivity is then calculated from the SNR of the sidebands[169,170] (Fig. 22(d)) (see Supplementary for a derivation) using:

$$\sqrt{S_{QQ}^{\mathrm{N}}} = \frac{\Delta q_{\mathrm{rms}}}{\sqrt{2\Delta_f} \times 10^{\mathrm{SNR_{dB}}/20}} \tag{128}$$

where Δ_f is the resolution bandwidth of the measurement and $\mathrm{SNR_{dB}}$ is the sideband signal-to-noise ratio in decibels[171]. The factor of $\sqrt{2}$ takes into account that information can be extracted from both sidebands by homodyne detection.

It is important to distinguish between sensitivity to charge on the charge sensor (for example on the island of an SET) and on the target (i.e. the object being sensed, such as a qubit). The sensitivity to charge on the target is generally worse, because one electron on the target induces less than one electron on the sensor. If Δq_{rms} is a charge induced on the sensor, then Eq. (128) gives the sensitivity to charge on this sensor, and can be used to compare sensors without any need to measure a target. However, the time taken to resolve a charge of one electron on the target is:

$$\tau_{\min} = \frac{S_{QQ}^{\mathrm{N}}}{2e^2}\left(\frac{C_\Sigma}{C_{\mathrm{m}}}\right)^2 \tag{129}$$

where C_{m} is the mutual capacitance and C_Σ is the total capacitance of the system to be sensed[169].

(ii) In the time domain, by monitoring the sensor response with and averaging it over bins of duration τ_{int} while the target system to be sensed changes state (either actively driven by voltage pulses, or passively when it fluctuates between states). Then the data is collected in a 2D histogram over the IQ plane and the SNR$= (S/\sigma)^2$ is calculated from the voltage distance between centers of the clusters (S) and their average standard deviation (σ) along the axis that joints the two centres (see Fig. 23(a)). The charge sensitivity is

$$\sqrt{S_{QQ}^{\mathrm{N}}} = \frac{\sqrt{2\tau_{\mathrm{int}}}\,e}{\sqrt{\mathrm{SNR}}} \tag{130}$$

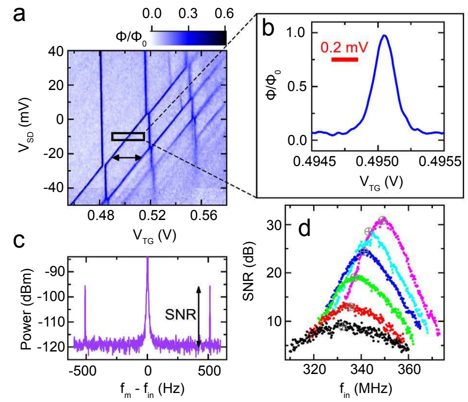

FIG. 22. Charge sensitivity in the frequency domain. (a) Reduced phase response of the resonator as a function of source-drain V_{SD} and top-gate voltage V_{TG} at 50 mK, measured with rf power of -93 dBm. The black box indicates the dot-to-reservoir transition used to measure sensitivity and the arrow the gate voltage period. (b) The same transition as indicated in (a), measured at $V_{\mathrm{SD}} = -10$ mV. The input rf power here is -103 dBm. The red line indicates the peak-to-peak amplitude of the top-gate modulation signal. (c) Spectrum of the reflected power, showing sidebands at the gate modulation frequency of 511 Hz. (d) SNR as a function of carrier frequency f_{in} for a frequency tunable resonator including a variable capacitor as in Fig. 19(a). Black, red, green, blue, cyan and pink correspond to voltages across C_{t} equal to 0, 1.5, 3, 4.6, 6.5, 15 V, respectively. The maximum SNR is marked for each data set with a grey circle. Reproduced from[7], with the permission of AIP Publishing.

For dispersive sensing, the readout resonator probes directly the system to be sensed instead of detecting it via an intermediate charge sensor. For that reason, the preferred figure of merit has been the SNR of the two possible outcomes of the measured system with given measurement duration τ_{int} (Fig. 23(b)). The methodology followed to extract the SNR is identical to the time-domain case (ii) above. Given the relation

$$\mathrm{SNR} = \frac{\tau_{\mathrm{int}}}{\tau_{\min}}, \tag{131}$$

the SNR measured at any value of τ_{int} implies a value for $\tau_{\min}$ (Fig. 23(b,c)), enabling a direct comparison between the measurement time for charge sensors and dispersive readout.

Typically, the effective integration time is given by the integration time of the digitizer if it is chosen much larger than the intrinsic integration time associated with the analog demodulation setup. (For short digitizing times, the intrinsic integration time contributes to τ_{int}, and can be taken into account when analyzing SNR(τ_{int}) data[43,165].)

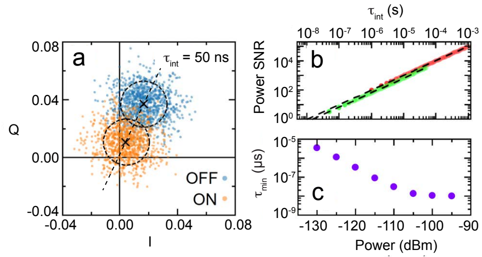

FIG. 23. Signal-to-noise ratio in the IQ plane[138]. (a) Distribution of the reflected signal in quadrature space, collected at gate settings on and off an interdot charge transition. Each point is collected with an integration time $\tau_{\text{int}} = 50$ ns. For each distribution, the black cross marks the centre (mean) and the dashed circle indicates the standard deviation of distance to the centre. The dashed line marks the axis that joints the two centres. (b) SNR dependence on τ_{int} for input power $= -100$ dBm. Red points are taken with a 1 MHz low-pass filter and green points are taken with a 20 MHz low-pass filter. The dashed lines extrapolate the data to SNR = 1, from which the minimum integration time τ_{min} can be extracted. (c) Decrease in τ_{min} with increasing input power, showing saturation due to power broadening at approximately -100 dBm. David J. Ibberson, Theodor Lundberg, James A. Haigh, Louis Hutin, Benoit Bertrand, Sylvain Barraud, Chang-Min Lee, Nadia A. Stelmashenko, Giovanni A. Oakes, Laurence Cochrane, Jason W.A. Robinson, Maud Vinet, M. Fernando Gonzalez-Zalba, and Lisa A. Ibberson, PRX Quantum 2, 020315, 2021; licensed under a Creative Commons Attribution (CC BY) license.

E. Opportunities and challenges

In Section V A 2 we discussed how voltage-controlled capacitors can be used to optimise the impedance matching *in situ*. However, semiconductor-based varactors are lossy, degrading the quality factor of the circuit and thus its sensitivity. Another challenge is the small tuning range at cryogenic temperatures[7,144]. To overcome these limitations, we could use varactors based on ferroelectric materials, such as the lead titanate and barium strontium titanate families of solid solutions. The highly non-linear dielectric permittivity enables control of the capacitance via an electric field and, at temperatures at which the material is in its paraelectric state, low dissipation can be achieved. However, at low temperatures, ferroelectricity affects the tunability and loss tangent of these varactors. Opportunities are therefore open for the improvement of varactors.

Coplanar waveguide architectures can also benefit from tunable capacitances. Quantum paraelectric materials, such as $SrTiO_3$, $KTaO_3$, and $CaTiO_3$, allow for such capability. In these materials, quantum fluctuations suppress ferroelectricity at low temperatures. In particular, $SrTiO_3$ has a very high relative permittivity at mK temperatures[172–176], which is tunable using electric fields. A $SrTiO_3$ varactor was integrated in an rf circuit, allowing for perfect impedance matching down to 6 mK[177]. Other quantum paraelectrics, such as $KTaO_3$, may reduce losses further, at the cost of less tunability[178]. Tunable microwave impedance matching can also be achieved using a coplanar resonator whose inner conductor contains a high kinetic inductance metamaterial, in this case a series array of SQUIDs[179]. The matching frequency of such circuits was demonstrated to be tunable between 4 and 6 GHz. This approach has not been yet applied to the rf readout of quantum devices.

A potential avenue for improving the readout of resistive devices is to design impedance matching networks with a matching resistance larger than the on-state resistance of the device. In that scenario, by moving from the overcoupled (high resistance state) to the undercoupled regime (low resistance state), $|\Delta\Gamma| > 1$ could be achieved. Note that $|\Delta\Gamma| = 1$ for the case where the inductive and dielectric losses are negligible and critical coupling is achieved for the on-state of the device.

Going beyond varactors, which are essential elements for optimal readout of resistive devices, dispersive readout of reactive devices will benefit from further improvements. At the device level, structures with high lever arm are desirable since they result in higher quantum capacitance changes (see Eq. 121). Using thin gate oxides or high-k dielectrics will facilitate that goal. Also thin layers of material, like thin silicon-on-insulator or wrap-around gates can increase the lever arm further.

At the resonator level, the directions to go are towards high-impedance, high-Q and high-frequency resonators. High-frequency, high-impedance resonators can be achieved by minimising the effect of parasitic capacitance. Planar circuit elements, either capacitors or inductors, have less parasitic capacitance than surface mount components. On-chip resonators reduce the effect of parasitics further[180]. Besides, inductive coupling results in even lower total capacitance than capacitive coupling[138]. High-frequency operation is also favourable for minimising back-action due to the reduced thermal photon shot noise (Eq. 126). A potential drawback of operating at higher frequencies is that quantum capacitance effects are governed by charge reconfiguration due to the high-frequency electric field excitation. If the characteristic charge tunneling times are comparable or slower that the probe frequency, the magnitude of the quantum capacitance change is reduced[104]. To reduce non-radiative losses in the resonator and hence increase the internal quality factor, resonators will need to be manufactured using superconducting materials on low-loss substrates with high-quality interfaces such as sapphire or quartz. Even further advances may be possible by changing paradigm to longitudinal coupling, by modulating the resonator-qubit coupling at the frequency of the resonator, an approach considered to be generally quantum-limited[181].

VI. AMPLIFIERS AND NOISE

In a typical quantum electronic experiment, the signal of interest is tiny, with the useful information often contained within a total signal amplitude of 1 μV or less[144]. Inevitably, this signal is accompanied by noise. To extract the information, the signal must usually be increased to a level where it can be analysed by digital electronics, which typically operates at logic levels above 1 V. A central challenge in quantum electronics is to do this with as little noise as possible. Unfortunately, on top of noise intrinsic to the experimental device, there are noise contributions (which are often much larger) from almost every component in the measurement chain. The topic of this section is how to quantify and reduce these, in order to minimise the effects of noise in an experiment.

A. Quantifying noise in an electrical measurement

Suppose we want to measure the voltage being reflected from a radio-frequency resonator as in Section II. The signal that we want to measure is $V_S(t)$. For example, Fig. 24(a) shows a simulated voltage trace from a device that is switching regularly between two states. Instead, we measure something like Fig. 24(b). Our measured signal is

$$V(t) = V_S(t) + V_N(t). \tag{132}$$

The second term, which by assumption carries no information about the signal, is the noise.

To understand the effect of the noise on our experiment, we need to answer two questions:

1. How should we describe the noise contained in a voltage trace $V(t)$? This question is answered in Sections VI A 1 and VI A 2.

2. What uncertainty will this noise introduce in an estimate of $V_S(t)$, or of a quantity derived from it? This question is answered in Section VI A 3.

1. *Quantifying noise using the spectral density*

How should we characterise a noisy voltage trace $V(t)$? Since on average the noise is zero, we should quantify the variance. Suppose that we construct a filter that passes only those components within a frequency bandwidth B_f centered at frequency f. The magnitude of the filtered signal $\mathbb{V}(t)$ depends on which components are passed, i.e. on how wide we choose B_f. We therefore quantify it by means of the one-sided voltage spectral density $S_{VV}(f)$, which in almost all circumstances is given by

$$S_{VV}(f) = \lim_{B_f \to 0} \frac{\lceil \langle \mathbb{V}^2(t) \rangle \rceil}{B_f} \tag{133}$$

where $\langle \cdot \rangle$ denotes an expectation value and $\lceil \cdot \rceil$ is a time average. The voltage spectral density is a measure of how strongly $V(t)$ fluctuates near frequency f. Its units are V^2/Hz and it can be measured using a spectrum analyser. For a precise definition of $S_{VV}(f)$ and instructions how to calculate it, see Supplementary Information S3.

If the signal and the noise are uncorrelated, which is usually the case, the spectral density can be separated into a signal contribution $S^{\mathrm{S}}_{VV}(f)$ and a noise contribution $S^{\mathrm{N}}_{VV}(f)$:

$$S_{VV}(f) = S^{\mathrm{S}}_{VV}(f) + S^{\mathrm{N}}_{VV}(f). \tag{134}$$

We therefore describe the noise quantitatively by specifying the noise spectral density $S^{\mathrm{N}}_{VV}(f)$, which is the spectral density in the absence of signal, i.e. when $V_S = 0$. Generally we want $S^{\mathrm{S}}_{VV}(f)$ to be large and $S^{\mathrm{N}}_{VV}(f)$ to be small.

To allow comparison between measurements, S^{N}_{VV} is usually quoted as an input-referred noise, which means that it is based on the inferred signal $V(t)$ at the input to the first amplifier encountered by the signal. To calculate the input-referred voltage $V(t)$ from a voltage record such as an oscilloscope trace, you should divide the recorded voltage by the total gain of the amplifier chain before the recording device.

2. *Other ways to specify noise: Noise power, noise temperature, and noise quanta*

The noise spectral density can be expressed in three equivalent ways. Firstly, it can be written as a noise power density $p_N(f)$, which is the power per unit bandwidth that the noise delivers to a matched load:

$$p_N(f) \equiv \frac{S^{\mathrm{N}}_{VV}(f)}{Z_0} \tag{135}$$

where Z_0 is the input impedance of the measurement circuit. The power density has units of W/Hz, or equivalently dBm/Hz.

Secondly, it can be written as a noise temperature

$$T_N(f) \equiv \frac{p_N(f)}{k_B} = \frac{S^{\mathrm{N}}_{VV}(f)}{k_B Z_0}. \tag{136}$$

This is the temperature of a fictitious classical resistor[182] with resistance equal to the amplifier's input impedance, that when connected to the amplifier would generate a thermal noise spectrum equal to $S^{\mathrm{N}}_{VV}(f)$.

Thirdly, a noise spectrum is occasionally[183,184] expressed as a number of noise quanta

$$N_N(f) \equiv \frac{p_N(f)}{hf} = \frac{k_B T_N}{hf}. \tag{137}$$

The physical interpretation[185] is that a measurement with bandwidth B_f detects a noise power equivalent to quanta incident at a rate $N_N B_f$.

3. *Predicting measurement uncertainty; sensitivity*

As seen from Fig. 24, the noise voltage $V_N(t)$ obscures the signal $V_S(t)$. In an experiment, we must try to estimate what $V(t)$ would have been had the noise not been present. To be concrete, suppose the signal is

$$V_S(t) = V_m \cos(2\pi f_m t). \tag{138}$$

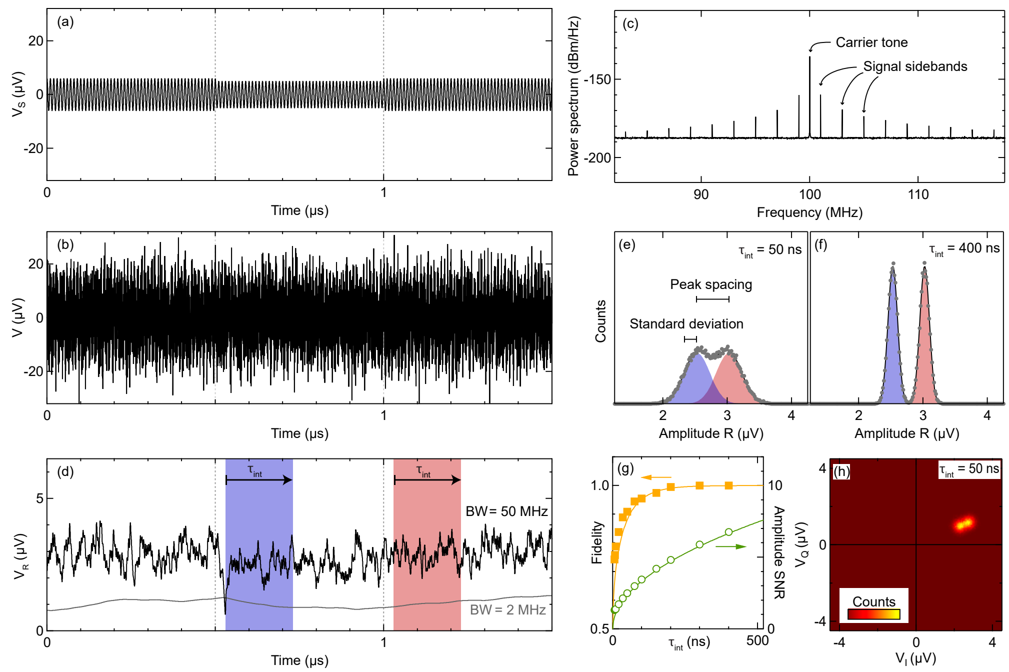

FIG. 24. Simulation of the effect of noise on raw data and on the processed signal. (a) Reflected signal $V_{\mathrm{S}}(t)$ switching regularly between two amplitude levels, as caused by a device switching between two states. (b) The same signal with added white noise of spectral density $S_{VV}^{\mathrm{N}} = 10^{-20}\ \mathrm{V}^2/\mathrm{Hz}$, corresponding to a noise temperature of 14.5 K. (c) The corresponding power spectral density $S_{VV}(f)/Z_0$ (from Eq. (S21)).(d) Upper trace: Signal amplitude $V_{\mathrm{R}}(t)$, defined by Eq. (30) and obtained by demodulating the trace in (a) and applying a 50 MHz low-pass filter. The shaded regions mark two intervals, each of duration τ_{int}, during which $V_{\mathrm{R}}(t)$ is averaged in order to determine whether it is high or low. Each interval begins shortly after the transition, with a short delay to cut out the response time of the filter. Lower trace: the same data, with the filter bandwidth set to 2 MHz (and vertically shifted for clarity). This filter eliminates most of the noise, but means that averaging overlaps with the rise time of the filter. It is therefore a bad choice. (e,f) Symbols: Histogram of amplitude measurements obtained from many averages as in (d). Shaded areas: inferred gaussian contributions from the low and high portions of the signal. (g) Right axis: Signal-to-noise ratio (SNR) as a function of averaging time τ_{int}, extracted from histograms as above. Signal is defined as the spacing between peaks, noise as the standard deviation. Left axis: Fidelity, defined as the probability of deducing the correct amplitude level based on a single averaging interval. In both cases, symbols are values extracted from the simulation and curves are analytical predictions, using Eq. (139(b)) for SNR and Eq. (174) for fidelity. (h) Similar averaged data as in (e), represented as a two-dimensional histogram over in-phase and quadrature voltages.

For example, V_{m} might take one value if a qubit has state 0 and a different value if the qubit has state 1. After acquiring a voltage record of duration τ_{int}, which necessarily includes the noise, we want to estimate V_{m} by taking the average (if $f_{\mathrm{m}} = 0$) or a Fourier integral (if $f_{\mathrm{m}} \neq 0$). What error do we expect in this estimate?

To answer this, we must calculate the variance in our estimate over different random values of the noise. This calculation (see Supplementary Section S3 B 1) gives for the expected error, i.e. the standard deviation in the estimate of V_{m}:

$$\sigma(V_{\mathrm{m}}) = \begin{cases} \sqrt{\dfrac{S_{VV}^{\mathrm{N}}(0)}{2\tau_{\mathrm{int}}}} & \text{if } f_{\mathrm{m}} = 0 \qquad (139\mathrm{a}) \\ \sqrt{\dfrac{S_{VV}^{\mathrm{N}}(f_{\mathrm{m}})}{\tau_{\mathrm{int}}}} & \text{if } f_{\mathrm{m}}\tau_{\mathrm{int}} \gg 1 \qquad (139\mathrm{b}) \end{cases}$$

This is the minimum uncertainty in our estimate of V_{m}. It is the reason why it is important to suppress the noise spectral density at the frequency of the signal.

Because Eqs. (139a-139b) determine the smallest signal that can be resolved in a measurement of duration τ_{int},

$\sqrt{S_{VV}^{\mathrm{N}}(f)}$ is called the sensitivity of the voltage measurement. In an experiment in which another quantity X is transduced to a voltage, the sensitivity of the measurement of X is

$$\sqrt{S_{XX}^{\mathrm{N}}(f)} = \left|\frac{\partial X}{\partial V}\right| \sqrt{S_{VV}^{\mathrm{N}}(f)}. \tag{140}$$

provided that $\partial X/\partial V$ is constant over the range of the noise.

B. The effects of noise

1. How noise appears in different types of measurement

Let us now see how noise affects the data recorded in a reflectometry experiment, and how this changes when the data are represented in different ways. Suppose we have a device, for example a qubit, which changes regularly between two states in such a way that the reflected signal switches between two amplitudes, ideally as in Fig. 24(a). A more realistic simulation must include noise (Fig. 24(b)). Here this is taken as white noise, meaning that $S_{VV}^{\mathrm{N}}(f)$ is independent of f within the frequency range to which the experiment is sensitive. In the time domain, the effect of noise is to increase the scatter of the data points. In the frequency domain (Fig 24(c)), the noise appears as a nearly uniform background in the power density, between the sharp signal sidebands which contain the useful information.

Our typical task is to deduce the device state based on a segment of the time trace. As explained in Section II D, we begin by demodulating the signal and low-pass filtering it to keep only the spectral range of interest. The top trace in Fig. 24(d) shows the amplitude of such a demodulated filtered signal. The two levels are barely evident, and obscured by noise near the carrier frequency that has been shifted downwards by demodulation and survives the filter. To identify the device state, the trace is therefore averaged over an interval τ_{int}, beginning just after the switching event.

When the averaged data are plotted as a histogram (Fig. 24(e-f)), the two levels become evident. With sufficiently long τ_{int}, the distribution separates clearly into two peaks, whose width is set by Eq. (139b). To assign the device state based on the record from a single measurement interval, the criterion is obvious: if the average signal is above the midpoint threshold, the device is in the high-reflection state, otherwise it is in the low-reflection state. The probability to assign the state correctly is called the fidelity[186] and is plotted in Fig. 24(g). Increasing the integration time or decreasing the noise allows higher-fidelity readout. The ability to distinguish the two states can also be expressed as the amplitude signal-to-noise ratio (SNR), which here is defined as the ratio between the peak spacing and the standard deviation[187] . Once the two histograms become distinct, i.e. SNR $\gtrsim 2$, the error probability depends exponentially on SNR, meaning that even small improvements in SNR lead to valuable improvements in the fidelity.

Sometimes it useful to plot similar data as a two-dimensional histogram in the $(V_{\mathrm{I}}, V_{\mathrm{Q}})$ plane (Fig. 24(h)) so that the two device states appear as two spots. This makes it clear if the phase as well as the amplitude is changing. In this figure, only the amplitude is varied, so the two spots lie on the same bearing from the origin.

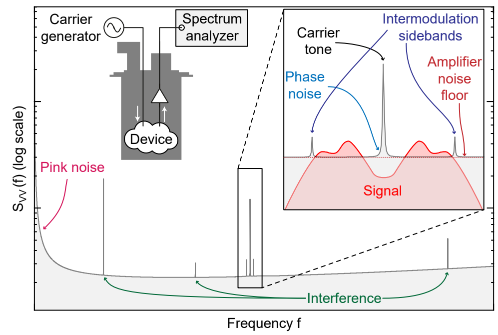

FIG. 25. Cartoon showing different contributions to the spectral density in a reflectometry experiment. Left inset: experimental schematic. The device is illuminated by a carrier tone, and the emitted spectrum is measured. Right inset: Zoom-in near the carrier frequency. Also shown is a possible spectrum for the signal being measured. The smaller the overlap of this signal with the noise spectrum, the easier it will be to identify.

2. Sources of noise in realistic circuits

Here are some types of noise encountered in an RF measurement, how you identify them, and what to do about them[188]. Figure 25 illustrates how some of them appear in the spectral density. In general the system noise is a combination of contributions from the device, the tank circuit, and the amplifier chain[61].

1. *Interference* from electronic instruments, power supplies, and radio transmitters appears as sharp peaks in the spectral density. It can be minimised by avoiding ground loops, by electromagnetic shielding, and by measuring at a frequency away from interference peaks. Often the most insidious interference comes from low-frequency signals, such as vibrations and power-line pickup, that create intermodulation sidebands near the carrier frequency.

2. *Pink noise* is a generic term for noise that is most intense at low frequency. Phenomenologically it is often found that $S_{VV}^{\mathrm{N}}(f) \propto 1/f$. A common cause is charge switchers in the device being measured. The cure for pink noise is to shift your signal away from zero frequency by using a carrier frequency above the relevant frequency band, scanning quickly, and/or making a lock-in measurement.

   Similar effects can also create a pair of spectral wings near the carrier frequency. These are often called phase noise[189]. Again, the cure is to make your signal vary in a way that puts its frequency components outside the noisy range.

3. *Thermal noise* is the black-body radiation emitted by any dissipative circuit element. In cryogenic experiments, electromagnetic thermal noise coming away from the device is rarely a problem; thermal noise going towards the device must be suppressed with attenuators, filters, and circulators (Fig. 31). The spectral density of thermal noise into a matched load is
$$S_{VV}^{\mathrm{N}}(f) = \frac{hfZ_0}{e^{hf/k_\mathrm{B}T}-1}. \tag{141}$$
If $hf \ll k_\mathrm{B}T$, which is often the case, then
$$S_{VV}^{\mathrm{N}}(f) \approx k_\mathrm{B}TZ_0, \tag{142}$$
which is where Eq. (136) comes from (but see Footnote[182]).

4. *Shot noise* is broadband noise caused by a current flowing through a tunnel barrier. The spectral density of this current noise is given by Eq. (51). This current noise transforms to voltage noise at the amplifier input. Being fundamental, shot noise is generally unavoidable, but it is also usually small.

5. *Quantum noise* is the result of quantum fluctuations. Under most conditions, an amplifier's noise temperature must satisfy the *standard quantum limit* (SQL) for continuous measurements, which means[185]
$$T_\mathrm{N} \geq \frac{hf}{2k_\mathrm{B}}. \tag{143}$$
In electronic experiments it is very hard to reach this limit, let alone surpass it. It is discussed further in Section VI D 1.

6. *Amplifier noise* is the noise added by the amplifiers. It includes the effects listed above, but also contributions from other physical processes inside the amplifiers, which are generically called technical noise. The noise from a commercial RF amplifier usually varies smoothly with frequency (Fig. 30), leading to a nearly uniform spectral background which is hard to evade. In optimised experiments, technical amplifier noise usually dominates other sources. It can often be mitigated by buying a high-end amplifier and cooling it down.

C. Suppressing noise using cryogenic amplifiers

To suppress noise, often the greatest single improvement is to cool down the primary amplifier. Low temperature suppresses thermal noise and switching noise in semiconducting components. It also makes it possible to use superconductors. Since quantum electronic experiments are usually carried out in a dilution refrigerator, the required cold space is readily available. Virtually all advanced high-frequency measurements in this field use cryogenic semiconductor amplifiers, and many now use superconducting amplifiers as well.

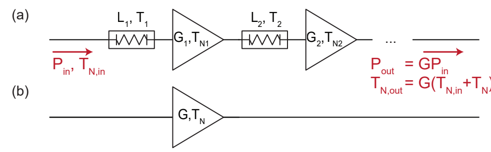

FIG. 26. (a) An amplifier chain, consisting of a series of amplifiers, each with gain G_i and noise temperature $T_{\mathrm{N}i}$, connected by transmission lines each with loss L_i and at temperature T_i. (b) The corresponding equivalent amplifier, with gain and noise given by Eqs. (144) - (145). If the chain receives a signal power P_in superimposed on thermal noise at temperature $T_{\mathrm{N,in}}$, it will output signal power P_out superimposed on thermal noise at temperature $T_{\mathrm{N,out}}$.

1. Amplifier chains

To appreciate the benefit of a cryogenic primary amplifier, we need to know how the noise of a measurement changes when a series of amplifiers is cascaded as in Fig. 26. Each amplifier has a power gain ratio G_i and a noise temperature $T_{\mathrm{N}i}$. Furthermore we should take account of losses in the transmission lines leading to the amplifier inputs, each of which transmits a fraction $1/L_i$ of the power and is at physical temperature T_i. Assuming there are no impedance mismatches, the entire chain behaves as a single amplifier[11] with gain
$$G = \frac{G_1G_2\cdots}{L_1L_2\cdots} \tag{144}$$
and noise temperature
$$T_\mathrm{N} = [(L_1-1)T_1 + L_1T_{\mathrm{N}1}] + \frac{L_1}{G_1}[(L_2-1)T_2 + L_2T_{\mathrm{N}2}] + \frac{L_1L_2}{G_1G_2}[(L_3-1)T_3 + L_3T_{\mathrm{N}3}]\cdots. \tag{145}$$

The first term in each square bracket can usually be neglected, giving a noise temperature:
$$T_\mathrm{N} = L_1T_{\mathrm{N}1} + \frac{L_1L_2}{G_1}T_{\mathrm{N}2} + \frac{L_1L_2L_3}{G_1G_2}T_{\mathrm{N}3} + \cdots. \tag{146}$$

Since all of the gains appearing in Eq. (145) are usually much greater than unity, it is clear that the overall noise is dominated by the first amplifier in the chain. This is why a low-noise primary amplifier is so important. Later amplifiers still contribute noise, but to a lesser extent. Equation (146) also tells us that transmission loss before the amplifier should be minimised. This points to another advantage of cryogenic amplifiers; they can be connected to the device by a short length of superconducting cable, which has extremely low loss.

2. Semiconductor amplifiers

Packaged cryogenic semiconductor amplifiers (Fig. 27) are commercially available and easy to use. The active elements are usually SiGe bipolar junction transistors

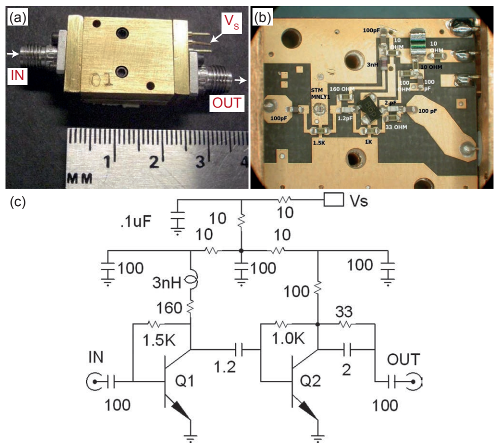

FIG. 27. (a) A cryogenic semiconductor amplifier in its package, intended to be mounted on the 4K plate of a dilution refrigerator. Typically, SMA connectors are used as input (IN) and output (OUT) ports, and low frequency connector pins provide the dc power supply voltage V_S. (b) Photograph of amplifier circuit board, which is based on bipolar junction transistors (BJT) and other low-temperature compatible surface mount components. (c) Circuit diagram of panel (b). Reproduced from[190], with the permission of AIP Publishing.

(BJTs)[190] or InGaAs/InAlAs/InP high-electron-mobility transistors (HEMTs)[191]. Optimum amplifier design is a trade-off between noise, impedance, and stability. For example, decreasing transistor size improves the high-frequency response by increasing the bandwidth, but also increases switching noise. At present it appears that at microwave frequencies (above about 4 GHz), HEMTs generally work better. At lower frequencies, BJTs are often preferred despite a sub-optimal noise temperature because of their good wideband input impedance matching, which prevents unwanted standing waves or, even worse, self-oscillations. In both cases, the amplifier should be mounted at the 4 K stage of the refrigerator.

3. *Superconductor amplifiers*

The very quietest RF amplifiers are based on superconductors. The active elements are Josephson junctions. The simplest superconducting amplifier is the superconducting quantum interference device (SQUID) amplifier (Fig. 28). This exploits the fact that the critical current of a dc SQUID[193] depends on the magnetic flux Φ enclosed between its two junctions[192]. When the SQUID is biased above its critical current, changes in critical current lead to changes in the voltage across the terminals. A small flux generated by the input signal therefore leads to a comparatively large output voltage. To maximise the oscillating flux, the input coil is usually engineered as a resonator, for example the microstrip resonator shown in Fig. 28(b).

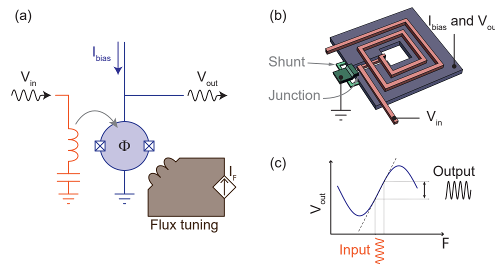

FIG. 28. The SQUID microstrip amplifier[192] (a) Working principle. The active element is a SQUID (center) biased by a dc current I_{bias} greater than the critical current, which leads to voltage V_{out} at the output port. When a voltage V_{in} is applied at the amplifier input, it excites a current in the microstrip resonator. This modulates the flux Φ through the SQUID washer, which in turn modulates the critical current and therefore V_{out}. A flux tuning loop adjusts the dc flux to the point of maximum response. (b) Geometry of washer (blue and green) and microstrip coil (pink), which is separated from the washer by an insulating layer (not shown). A pair of shunt resistors, not drawn in the circuit diagram, suppresses hysteresis. (c) Solid curve: $V_{\text{out}}(\Phi)$ characteristic of an ideal SQUID. The modulation of the flux by the input signal and its effect on the output are sketched.

SQUID amplifiers achieve better sensitivity than semiconductor amplifiers, but are more difficult to operate. The working bandwidth is small and not easily tunable, because it is set by the properties of the resonant coil. The power handling is poor because of the SQUID's non-linearity, although this can be mitigated by injecting a cancellation tone to null out the carrier tone[194]. SQUIDs must also be well-shielded from magnetic fields, even nominally constant ones such as from superconducting magnets in the same room. Nevertheless, SQUID amplifiers hold the record for voltage sensitivity at low RF frequency (Fig. 30) and have successfully been used for reflectometry[195,196].

Another type of superconducting amplifier is the Josephson parametric amplifier (JPA)[197–199] To understand the principle of parametric amplification, consider the LC resonator shown in the inset of Fig. 29(a). The energy stored in the inductor depends quadratically on the instantaneous current $I(t)$ (Fig. 29(a-b)). Now suppose the inductance is changed twice per oscillation cycle, being increased when $I(t)$ is maximal and decreased when $I(t)$ is zero. The effect is to increase the stored energy in each repetition, thus amplifying the current (Fig. 29(c)). In practice the inductance does not need to jump abruptly, but is modulated sinusoidally at twice the resonator frequency as shown[200]

The simplest implementation of a JPA is shown in Fig. 29(d). The variable inductance is provided by a Josephson junction, whose inductance depends on the current according to[197,201]

$$L_J(I) = \frac{\hbar}{2eI_0}\frac{1}{\sqrt{1-I^2/I_0^2}} \tag{147}$$

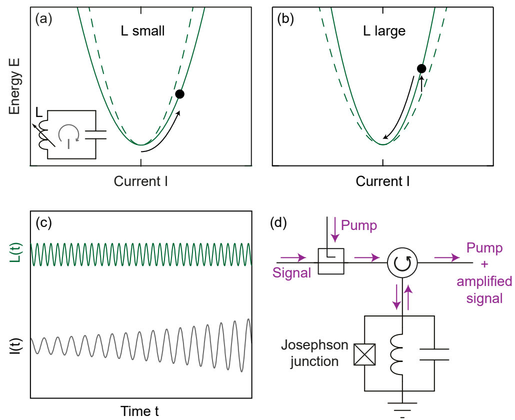

FIG. 29. Parametric amplification. Panels (a) and (b) show energy as a function of current in an LC resonator, whose circuit is shown in the inset. The state of the resonator is indicated by a dot. Twice per cycle, the resonator is switched between its high-L and low-L condition, so that the current increases under the low-L condition (a) and decreases under the high-L condition (b). In this way, the energy in the resonator increases in each cycle. (c) Sketch showing how L is modulated at twice the resonance frequency causing the amplitude of I to increase. (d) Simple Josephson parametric amplifier. The Josephson junction embedded in the LC resonator is a non-linear element whose effective inductance is modulated by a pump tone. To operate the amplifier, a circulator feeds the pump and the signal to the resonator, and routes the reflection containing the amplified signal towards a semiconductor postamplifier.[197]

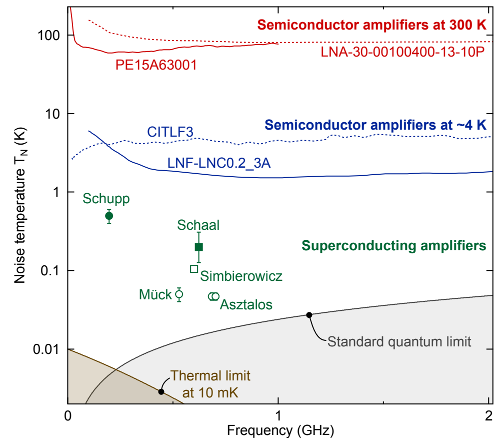

FIG. 30. Noise temperature as a function of frequency for selected state-of-the-art amplifiers. Lines are examples of low-noise commercial amplifiers operating near room temperature and near 4 K. Symbols are superconducting amplifiers operating in dilution refrigerators. Amplifiers used in a reflectometry configuration are Schupp *et al.*[196] using a SQUID, and Schaal *et al.*[203], using a JPA. Lower-noise amplifiers not yet used for reflectometry include SQUID amplifiers (Mück *et al.*[205], Asztalos *et al.*[206]) and JPAs (Simbierowicz *et al.*[207]). The shaded regions lie beyond the standard quantum limit (Eq. (143)) and the thermal limit at 10 mK (Eq. (168)). Footnote 182 explains why the thermal limit is not equal to the physical temperature.

where I_0 is the critical current[202]. To modulate the inductance, $I(t)$ should be driven by an intense pump tone. Since $L_J(I)$ is an even function, pumping at the resonator frequency f_{LC} generates the modulation at $2f_{LC}$ that Fig. 29(c) requires. More complex implementations of the JPA principle distribute the amplifier's non-linearity over a series of junctions. Advanced JPAs, typically working at around 7 GHz, can reduce all other noise sources to the extent that intrinsic quantum noise given by Eq. (143) is the dominant remaining contribution[184]. In a reflectometry experiment[203], a JPA has attained a noise temperature of ~ 200 mK at 622 MHz, an order of magnitude better than a semiconductor amplifier.

Among the most advanced JPAs are travelling-wave parametric amplifiers (TWPAs), which replace the single resonator of Fig. 29(d) by an array of cells through which the signal passes once[204]. As well as the convenience of operating in transmission instead of reflection, TWPAs allow good bandwidth and power handling compared with reflective JPAs, although fabrication is more difficult and the sensitivity is so far not quite as good. To our knowledge no TWPA has yet been operated below about 4 GHz. The advantages of different kinds of parametric amplifiers were recently reviewed by Aumentado[197].

Although JPAs of various kinds now have excellent performance at microwave frequency and many experiments have operated close to the bounds set by quantum mechanics, radio-frequency JPAs are less well-developed. This is illustrated by Fig. 30, which compares the noise performance of different radio-frequency amplifiers. The quietest amplifiers in this frequency range are SQUIDs, although both SQUIDs and JPAs are still some way from the standard quantum limit.

All cryogenic amplifier chains require careful engineering to operate with the best performance. Figure 31 shows a typical wiring scheme.

D. Opportunities and challenges

1. *The standard quantum limit*

How quiet can an amplifier be? Quantum uncertainty limits the sensitivity of any continuous measurement, because the back-action induced at one time disturbs the observable's state a short time later. To be precise, for an electromagnetic mode associated with a voltage

$$V(t) = V_I \cos(2\pi f t) + V_Q \sin(2\pi f t), \qquad (148)$$

a measurement of V_I perturbs V_Q and vice versa. If an amplifier has large gain and is phase-preserving, meaning that it is

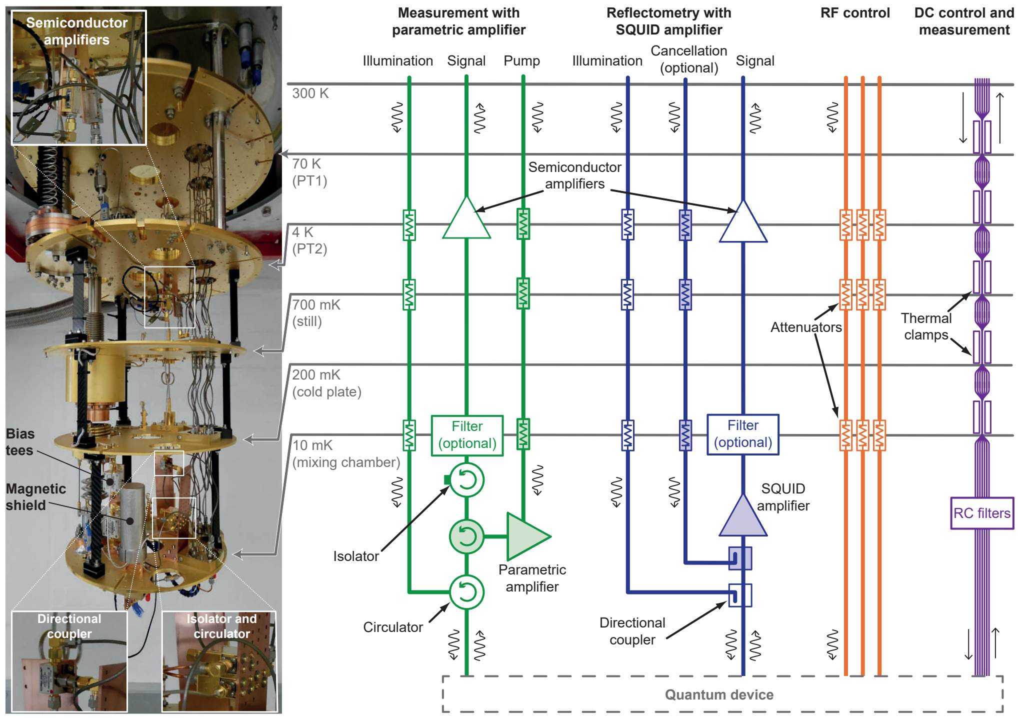

FIG. 31. Right: Typical refrigerator wiring for high-frequency measurements. This setup includes (left to right): Measurement chain using reflection-mode parametric amplifier (based on Ref. 203); measurement chain using SQUID amplifier (based on Ref. 196); high-frequency control lines using coaxial cable; quasi-dc control and measurement lines using cryogenic loom. Such a setup can also be operated without superconducting amplifiers by omitting the shaded components. To protect the quantum device from thermal radiation, all lines are attenuated and/or filtered at various stages inside the refrigerator, and thermally clamped to minimise the heat load on the mixing chamber. Components drawn below the 10 mK line are in thermal contact with the mixing chamber plate, but not necessarily below it. Left: A Triton 200 refrigerator wired in a similar arrangement. This refrigerator is equipped with a flux-pumped parametric amplifier[207], and therefore contains two bias tees (not drawn in the circuit diagram) through which the amplifier is biased. Selected components are labelled.

equally sensitive to V_I and V_Q (which is the usual situation) this imposes a minimum noise given by Eq. (143). This is the standard quantum limit (SQL).

Most electronic amplifiers work far from this limit. However, if an experiment is so sensitive that the SQL becomes a problem, then there is a way to evade it by combining two tricks. The first trick is to make the observable of interest appear in only one quadrature of Eq. (148). For example, to measure the reflected amplitude as in Fig. 24, the phase can be defined so that the signal is entirely in the V_I quadrature. The second trick is that the parametric scheme shown in Fig. 29 only amplifies a signal with the correct phase relative to the pump; the complementary phase is attenuated. By pumping in a way that amplifies only V_I, the observable can therefore be measured with arbitrary precision. In the $(V_\mathrm{I}, V_\mathrm{Q})$ plane (Fig. 24(h)), the noise spots are squeezed along one axis at the price of spreading out along the other. Squeezing measurements have been applied for precise measurements of microwave electromagnetic fields[184] and thereby to electron spins[208] and superconducting qubits[209]; the same strategy should work for spin qubits.

In a reflectometry experiment, this is possible because the axis of squeezing can be controlled by the phase between the carrier tone and the amplifier pump. Remarkably, squeezing sometimes also helps measure incoherent emission, which has no defined phase. In a measurement without squeezing, the sensitivity to such a signal is maximal at a cavity resonance but declines for frequencies on either side. By injecting a squeezed signal into the cavity, the optimum frequency range can be extended while the optimal sensitivity stays the same[210]. This strategy is therefore useful when the possible frequency range of the target signal is greater than the linewidth of the cavity. It was invented to search for dark matter, for which the frequency scan range must be very large[211].

The subject of quantum limits on continuous measurements is an intricate one, reviewed in detail by Clerk *et al.*[185]. There is probably room for future circumventions of the SQL, both by applying known schemes in new experiments and by devising even more ingenious ones.

2. New types of quantum amplifier

The first radio-frequency SET used a cryogenic HEMT amplifier with a noise temperature of $T_N = 10$ K at 1.7 GHz, which at the time was the state of the art[6]. As Fig. 30 shows, amplifiers have improved greatly, but there is still room to do better. In the next few years, we hope that rf superconductor amplifiers become as widely available and user-friendly as semiconductor amplifiers are today. As well as having low noise, they will also need to operate across a wide frequency range and handle comparatively large signals without saturating. This will be particularly important when measuring many devices using frequency multiplexing, since the total input power scales with the number of devices.

As seen from Fig. 30, there is still a need to extend the technology of quantum-limited microwave amplifiers down to rf frequencies. However, at the lowest frequencies the SQL becomes less important than thermal noise. In a 10 mK dilution refrigerator, thermal noise overtakes the SQL below 229 MHz. While there is scope for much quieter amplifiers than exist today, there will be no particular benefit from reaching the SQL at this frequency unless there are equal advances in ultra-low-temperature electronics[212].

Another need is for quantum-limited amplifiers that can operate in a magnetic field. In spin quantum computing and for magnetic resonance, the device being measured necessarily operates in a field between a few tens of mT and a few T. Any amplifier based on alumina Josephson junctions must therefore be placed some distance away, which costs space and sacrifices part of the signal to transmission losses. Interesting recent approaches that may one day overcome this problem include TWPAs based on kinetic inductance instead of Josephson inductance[213], and new Josephson junctions based on nanowires[214] and graphene[215] which can tolerate in-plane magnetic fields up to 1 T. Alternatively, a parametric amplifier could be based on a different degree of freedom, such as mechanical motion[216] or quantum capacitance[217]. Eventually a single resonator, with many devices embedded within it, might serve as a readout cavity and a parametric amplifier cavity simultaneously[218]. Such a device would be the ultimate combination of sensitivity and density in future large-scale quantum circuits.

VII. READING OUT MULTIPLE CHANNELS: THE CHALLENGE OF SCALING UP

Many experiments at the frontier of nanoscale electronics require fast concurrent impedance measurements, for instance in quantum computers where the execution of error correcting codes potentially amounts to the correlated readout of a

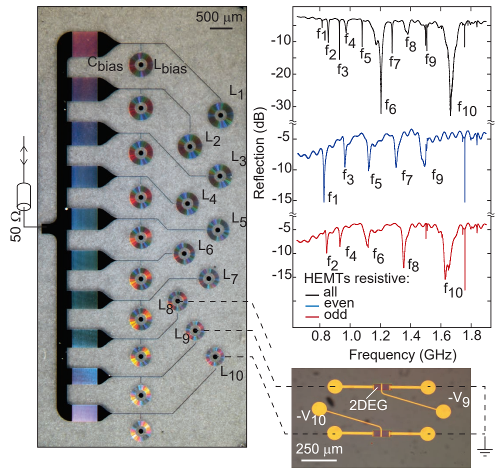

FIG. 32. Frequency division multiplexing makes use of a bank of lithographically defined resonators and bias tees. Here, the resonators are lumped element circuits fabricated using niobium superconductor on a sapphire substrate. The frequency domain response of the resonators is shown on the right, using HEMT devices (shown lower right) as resistors to modulate the Q-factor of each resonator. Reproduced from[143], with the permission of AIP Publishing.

large number of qubits. However, addressing this challenge via brute force duplication of a measurement setup quickly becomes unwieldy, in terms of the physical footprint of the duplicate sub-systems, of their power dissipation, and of unwanted interaction between them[219]. Duplicating all the necessary readout hardware for every parallel measurement is hardly a scalable approach. Multiplexing readout signals can dramatically improve the efficiency of these sub-systems by making use of total available bandwidth or duty cycle in the time domain. For measurements that must be performed simultaneously, frequency multiplexing is possible but requires a means of generating, amplifying, separating, and measuring signals across multiple frequencies. Conversely, time-domain multiplexing can be used for parallel-to-serial translation of measurement data. Both techniques can be combined[220] to enable hardware-efficient readout of multiple devices at high frequencies.

A. Frequency multiplexing

The rf reflectometry technique is immediately amenable to the parallel readout of multiple devices or sensors by encoding each device with a unique frequency or channel. Such an approach, which is usually termed *frequency division multiplexing (FDM)* at rf frequencies or equivalently, *wavelength division multiplexing (WDM)* in the optics and photonics communities, is the mainstay of modern communication systems.

Owing to the orthogonality of signals at different frequencies, the FDM technique enables the transmission of multiple frequency channels using a single transmission-line and amplification chain. Here we review the sub-components that make up a multi-channel system and describe how this approach enables efficient simultaneous readout of a large number of devices, for instance in the operation of a scaled-up qubit array.

1. Multiplexed resonators

Frequency multiplexing brings several new challenges in the design of the physical resonator structures used in an rf reflectometry setup. Most importantly, the footprint of the *LC* network can become critical since the signal feedline must branch into parallel lines that couple to each resonator simultaneously. At the frequency of one resonator the splitting of the feedline creates a 'stub' in which a parallel length of line is terminated with an open circuit, i.e., it is terminated with an *LC* network that is off-resonance. The stub allows interference of the standing wave reflected from the off-resonant open end of the parallel line with the signal feeding the resonator[11]. The phase accumulated by the parallel path, which depends on the length of the line, modifies the effective impedance of the network since it alters the ratio of current to voltage. This complication can be accounted for (or even exploited) in a few-channel system[221] but becomes increasingly challenging to address as the number of resonators and number of stubs is scaled up.

A potential solution is to minaturize the entire network so that the total path length l of any section is far smaller than the wavelength λ of the signal[143]. A rule of thumb is to set $l < \lambda/20$, ensuring that the entire network is in the 'near-field' regime where the inductive and capacitive contributions can be considered as lumped elements rather than a distributed circuit.

Defining the entire network lithographically enables a large number of resonators and feedlines to be integrated on a chip far smaller than the signal wavelength (recall, 1 GHz $\sim$ 25 cm). However, this requires superconducting materials, since miniaturised planar inductors made from normal metals such as copper have appreciable resistance. An implementation of the on-chip superconducting approach, including both resonators and bias tees, is shown in Fig. 32. It is worth noting that the use of superconducting materials makes operation in large magnetic fields challenging. The need for magnetic field-compatible resonators has motivated recent approaches to mitigate adverse effects such as the penetration of flux into the superconductor[222].

A further consideration with frequency multiplexing is that each resonator must operate at a unique frequency, lifting the freedom to choose the frequency where sensitivity is maximized. Rather than a narrowband system where each component has been selected to operate at a sweet spot, a multiplexed setup requires wideband sensitivity for the hardware components. In some instances the underlying device physics limits the possible operating frequencies. Examples include limits on tunnel rates, or energy scales at which high frequencies lead to back-action. Ultimately this limits the number of available channels owing to frequency crowding[143].

Finally, we draw attention to the additional challenges caused by inductive or capacitive crosstalk between resonators. One challenge is that nearby resonators can shift each other's frequencies, necessitating careful design of the entire network. A second challenge is that an excitation applied to one resonator can leak to another resonator at a nearby frequency. One mitigation is to design nearby resonators to have well-separated frequencies (i.e. allowing a guard band between their resonances). Another is to include on-chip ground planes and grounding rings. Fortunately such approaches are already widely used in the rf integrated circuit community.

2. Heterodyne techniques for frequency multiplexing

Heterodyne detection is yet another mitigation strategy, where the up- and down-conversion process has a character inherently amenable to multiplexing. The process can proceed as follows, utilizing the notation of Section II, where we have already discussed the principle of heterodyne detection, where the signal is demodulated using $f_{\mathrm{LO}} \neq f_{\mathrm{in}}$, the input signal frequency. This results in two signals at frequencies $f_{\mathrm{out}} - f_{\mathrm{LO}}$ and $f_{\mathrm{out}} + f_{\mathrm{LO}}$, where the second term is usually filtered out.

In the case of modulation, or up-conversion, we mix a local oscillator signal $\cos(\omega_{\mathrm{LO}}t)$ and its quarter-phase shifted copy $-\sin(\omega_{\mathrm{LO}}t)$ with a the modulating signals $I^i_{\mathrm{in}}(t) = I^i_{\mathrm{in}}\cos(\omega_i t)$ and $Q^i_{\mathrm{in}}(t) = Q^i_{\mathrm{in}}\sin(\omega_i t)$ respectively (for our purposes, we consider a signal from an arbitrary waveform generator (AWG)) and add them to form the input signal[223]

$$V_{\mathrm{in}}(t) = \cos((\omega_{\mathrm{LO}} + \omega_i)t + \phi). \tag{149}$$

at the up-converted angular frequency $\omega_{\mathrm{LO}} + \omega_i$ (Fig. 33). We ignore here the amplitude of the wave to focus on the frequency conversion. This can be trivially extended to multiple frequencies, by asking the AWG to output modulation signals of the form ω_1, ω_2 and so on, such that we arrive at the desired number of upconverted frequencies, for example for N qubits.

In the reverse process, during readout at multiple frequencies, the reflected signal

$$V_{\mathrm{out}}(t) = \cos((\omega_{\mathrm{LO}} + \omega_i)t + \phi) \tag{150}$$

is mixed with the LO signal of frequency ω_{LO} and phase δ for demodulation or down-conversion. This gives two outputs $I^i_{\mathrm{IF}}(t)$ and $Q^i_{\mathrm{IF}}(t)$ for the two quadratures[223]. We can represent these two signal as the real and imaginary parts of the complex signal

$$V^i_{\mathrm{IF}}(t) = e^{i(\omega_i t + \phi - \delta)} \tag{151}$$

$$I^i_{\mathrm{IF}}(t) = \frac{1}{2}\mathrm{Re}(V^i_{\mathrm{IF}}(t)) \quad Q^i_{\mathrm{IF}}(t) = \frac{1}{2}\mathrm{Im}(V^i_{\mathrm{IF}}(t)). \tag{152}$$

This process therefore now results in the original ω_i term, which now carries the amplitude and phase information stemming from the physical phenomena we are measuring, for that

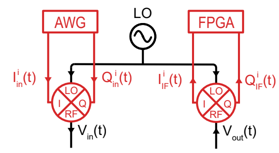

FIG. 33. Up and down conversion using IQ mixers[223]. A radiofrequency signal from a local oscillator LO is mixed with two waveforms $I^i_{\text{in}}(t)$ and $Q^i_{\text{in}}(t)$ generated by an Arbitrary Waveform Generation (AWG) for each multiplexed frequency i to obtain a signal $V_{\text{in}}(t)$. The output signal $V_{\text{out}}(t)$ is then down converted back with the reversed process resulting in two signals I^i_{IF} and Q^i_{IF} at each multiplexed frequency that are digitalised using a field-programmable gate array (FPGA).

particular subsystem, excited at that ω_i, by the AWG. Both the up- and down-conversion process can be repeated for an arbitrary number of ω_i, mixed into the same signal.

Readout of such a mixed signal, which resides at ω_i and not at DC, is typically accomplished via numerical post-processing, on-board on a field-programmable gate array (FPGA)[223]. The reflected and downconverted $I^i(t)$ and $Q^i(t)$, which contain ω_i components, are numerically mixed with the relevant ω_i, which results in the I^i and Q^i information of each ω_i signal. For a particular ω_i, this is done by multiplying the complex signal by $e^{-i\omega t}$

$$\begin{aligned} V^i_{\text{IF}}(t)e^{-i\omega t} &= I^i_{\text{IF}}(t)\cos(\omega_i t) + Q^i_{\text{IF}}(t)\sin(\omega_i t) \\ &\quad + i(-I^i_{\text{IF}}(t)\sin(\omega_i t) + Q^i_{\text{IF}}(t)\cos(\omega_i t)) \end{aligned} \tag{153}$$

and integrating, as follows:

$$I^i = \sum_n I^i_{\text{IF}}(t)\cos(\omega_i t) + \sum_n Q^i_{\text{IF}}(t)\sin(\omega_i t) \tag{154}$$

$$Q^i = \sum_n Q^i_{\text{IF}}(t)\cos(\omega_i t) - \sum_n I^i_{\text{IF}}(t)\sin(\omega_i t) \tag{155}$$

where consecutive samples n are digitally summed by the FPGA to remove the $2\omega_i$ components. The above equation means that four integrals have to be performed numerically to find the result in the IQ plane. In practice, the same lookup table can be used to generate only two signals, a sine and a cosine, by offsetting the lookup by a quarter cycle in the table. These can then quickly be multiplied and summed with the signal to give the result, for each of our ω_i.

3. Constraints on amplifiers and related components

Most cryogenic amplifiers used in rf reflectometry are designed to minimize the noise, maximise the gain, and achieve reasonable impedance matching. Optimizing all three parameters is difficult across a wide bandwidth. Semiconductor amplifiers that leverage feedback, for instance those based on SiGe transistors (see Section VI), achieve wideband operation at the price of increased noise from the feedback resistor. In comparison, amplifiers based on high electron mobility transistors (HEMTs) are typically configured to be open-loop and 'noise matched', i.e., the *LC* networks on the input and output of the transistor present an impedance that achieves the lowest noise and reasonable match. This is usually only possible across a narrow band. Frequency multiplexing is thus challenging for measurement setups that also require the lowest noise since encoding multiple parallel readout channels as a 'comb' of frequencies is inherently wideband. Potentially, this limitation may be overcome by making use of wideband superconducting amplifiers such as the traveling wave parametric amplifiers discussed in Section VI.

Beyond the bandwidth requirements, FDM brings two additional challenges for the amplification chain. Firstly, the total power of signals at all frequency tones must be considered. If a system is to support 10 frequency channels, for instance, then the amplifier compression power must support an input power that is 10 times higher than for a single channel. Secondly, non-linearities in the transfer characteristics of the readout chain can lead to intermodular distortion in which signals at different frequencies are mixed (multiplied) to produce new frequency components, often overlapping other channels.

It is also worth mentioning the challenges associated with broadband transmission. Although cryogenic measurement setups are usually configured with substantial microwave filtering and attenuation to block radiation, FDM requires wideband transmission in order to accommodate all channels. Thus, experiments requiring the lowest electron temperature can be particularly difficult to combine with wideband frequency-multiplexing readout.

4. Digital approaches to signal generation and acquisition

A key motivation for frequency division multiplexing is its potential to alleviate the burden posed by brute-force duplication of readout hardware. Although a single amplification chain can handle multiple frequency channels, demodulation hardware is still needed to create the baseband signals from which the device states are inferred. Conventional demodulation requires a separate frequency generator for each channel, as well as mixers, directional couplers, splitters, attenuators, and filters (see Fig. 34). Using analog hardware for this purpose is cumbersome when the setup requires even a handful of frequency tones and quickly becomes unworkable for the large channel counts needed for scalable quantum computing. (Figure 34 shows the analog hardware required for demodulating four frequency channels.)

Modern high-speed data converters and digital signal processing (DSP) can dramatically improve hardware efficiency when generating and detecting large numbers of frequency tones. Common approaches make use of a digital-to-analog converter (DAC) and an analog-to-digital converter (ADC), integrated with an FPGA that is accessible via a high-speed bus (such as the widely used PCIe platform).

This digital architecture first synthesizes a comb of frequencies in the digital domain, encoding frequency, phase, and am-

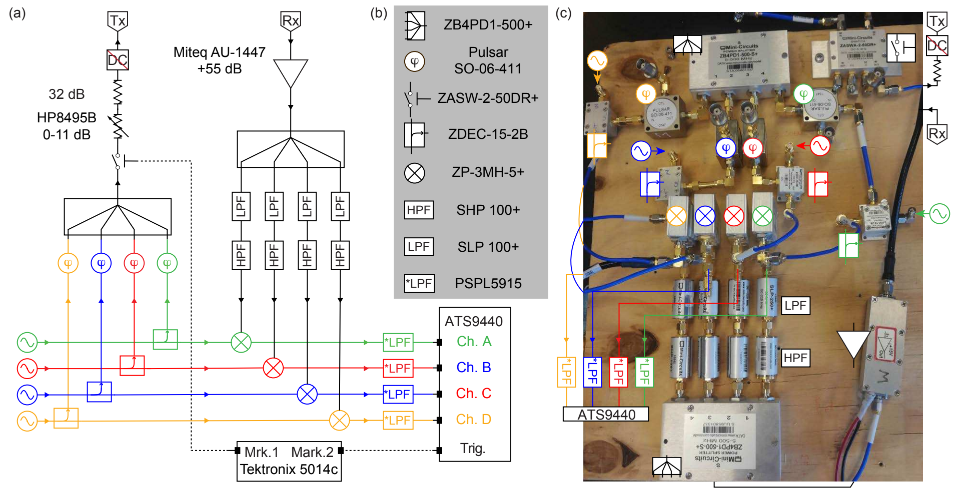

FIG. 34. A typical modulation / demodulation setup built from analog components to enable frequency multiplexed readout, here for the simultaneous readout of four spin qubits[68]. (a) Schematic of the circuit layout. (b) Legend of specific components. (c) Photograph of the circuit layout. SMA cable "Rx" provides the undemodulated RF signals from the cryostat to an amplifier, before the signal is divided into four paths, each with its own filtering (LPF, HPF) and mixing with a local tone. Local tones (provided via directional couplers) carry the same frequency as the carriers (homodyne detection), thereby resulting in four dc signals that are detected by four independent channels of the digitizer (ATS9440). Federico Fedele, Anasua Chatterjee, Saeed Fallahi, Geoffrey C. Gardner, Michael J. Manfra, and Ferdinand Kuemmeth, PRX Quantum 2, 040306, 2021; licensed under a Creative Commons Attribution (CC BY) license.

plitude of each tone. A wideband DAC then takes this stream of bits as input and generates the analog tones for transmission in a technique termed direct digital synthesis (DDS). On the receiver side, the collection of tones are amplified and then sampled at giga-sample per second clock rates using a wideband ADC. The digital output bit stream from the ADC generally feeds a bank of digital filters implemented in the FPGA, essentially performing a discrete Fourier transform. The platform writes to memory changes in amplitude and phase of carrier tones, referenced to the transmit signals generated via DDS. Adding or configuring new frequency tones is straightforward using a digital architecture for demodulation, in so far as the FPGA contains sufficient logic gates (and clock rate).

Finally, we note that hybrid digital and analog architectures are now in widespread use. High-speed digitizers (ADCs) paired with analog mixers or frequency sources are particularly common.

B. Time-division multiplexing

For many applications, the need for truly simultaneous measurements can be relaxed so that readout hardware can be used efficiently, switching between multiple devices sequentially or in an interleaved manner[224–228]. The potential to share readout resources in this way is generally referred to as time-division multiplexing (TDM). Such schemes can be configured so that a subset of devices (or qubits) are being measured while others are being manipulated or prepared. In general however, measurement is usually the slowest task.

Switches for implementing TDM are also not easy to come by. They need to operate at deep cryogenic temperatures, usually at the same temperature as the quantum devices, ($\lesssim$ 100 mK), dissipating microwatts of power or less. For readout applications, such switches must also have extremely low insertion loss, since attenuation before the first stage amplifier degrades the SNR. A further requirement is a large on-off ratio (or isolation), which is important to minimize crosstalk. Finally, the impedance of the switch is critically important.

Wide-band switches can be inserted in the readout chain in two places, depending on their attributes. For impedance-matched switches that have low insertion loss in the on state, it is possible to build switching networks that select distinct *LC* resonators for the readout of a targeted device.

An alternative and more scalable approach is to 'recycle' the resonator by using the switch to connect it to each measured device in turn[226]. This approach can dramatically reduce the footprint, since a single resonator structure reads out many devices. For such a configuration to be useful however, the switch should add minimal capacitance so as not to load the resonator.

C. A look ahead: Limits to multiplexing approaches

Multiplexing techniques provide a means to efficiently use all the available bandwidth or available time window to carry readout signals from multiple quantum devices and are key to the scale-up of quantum computing. However, it remains an open question how far these techniques can be extended and what new developments will be needed to enable parallel readout of millions of qubits. Below we discuss some of the likely constraints to scale-up and identify areas where new work is needed.

Above we discussed the requirements for low-noise amplifiers. Here we extend our discussion to include the entire readout chain. A scaled-up readout system must have ultra-wide bandwidth while preserving the noise, linearity, and power-handling capabilities of the state-of-the-art single-channel systems. To estimate some rough bandwidth requirements we note that applications of fast reflectometry typically require single-channel bandwidths of order a few MHz. Considering resonators constructed from lumped elements, a reasonable estimate is that 100 channels might occupy a total system bandwidth of 2 GHz, including frequency guard bands to suppress crosstalk.

In addition to the cryo-amplifiers, this estimate suggests that non-reciprocal elements such as circulators or isolators must also exhibit wideband performance. Traditionally, non-reciprocal elements are implemented using interference of microwave signals confined to bulky ferrite resonators, a mechanism that is inherently narrowband. Alternative means of realizing non-reciprocity[229,230] will likely be required to enable scale-up of frequency multiplexing.

With the need for each quantum device to be paired with a resonator operating at a particular frequency, the physical dimensions of the resonators also pose a challenge to scale-up. As is well known from the development of monolithic microwave ICs, creating large inductors on a chip is difficult due to the significant loop areas required. For quantum applications, however, the use of cryogenic temperatures opens the prospect of leveraging the kinetic inductance associated with superconductors to create small-footprint inductors. Indeed, this is a well established technique in the astronomy community[231].

Finally, we draw attention to requirements of the digital demodulation platform in a scaled-up system. Already, implementing the realtime digital synthesis and filtering sub-blocks of a handful of carriers requires some of the largest FPGAs available commercially. Likely, both the required algorithms and hardware can be optimized (effectively implementing the demodulation of highly multiplexed signals using optimized ASICs). Improvements in the performance of DACs and ADCs are also vital to enable multiplexed readout at scale. Again, the noise, linearity, and power-handling capability are key parameters that determine the suitability of data converters for readout applications. Recently, there have been several demonstrations of integrated circuits that provide a compact alternative to distributed readout chains[232,233].

VIII. SPIN QUBITS

A leading application of radio-frequency reflectometry for quantum information processing is readout of spin qubits in QDs. Semiconducting spin qubits comprise different qubit encodings (most commonly single-spin single-dot[234], singlet-triplet double-dot[23], and exchange-only triple-dot encodings[25]) and implementations in various semiconducting materials (most prominently GaAs, Si and Ge structures). A recent review of spin qubits is given by Ref. 235, whereas details of GaAs and silicon spin qubits were previously reviewed in Ref. 34 and Ref. 236–238, respectively. In the following, we explain the main rf techniques (Section VIII A) to detect spin in QDs, how to perform and interpret single-shot readout (Section VIII B) and we highlight the state-of-the-art experiments involving high-frequency singlet-triplet measurements (Section VIII C).

A. rf readout of spin qubit

The first step to reading out a spin qubit is to create an electrical signal that depends on the qubit state. The most common way to do it relies on spin-dependent tunneling mechanisms known as spin-to-charge conversion[21,23,239]. The qubit state can then be deduced either from the measurement of a charge sensor or by dispersive readout.

1. *Qubit readout using a charge sensor*

Fig. 35 shows two main mechanisms for accomplishing spin-to-charge conversion, which rely respectively on energy-selective and on spin-selective tunneling. In both cases the information about the spin is correlated with a specific charge-tunneling event or a static dot charge occupation that can be detected using a nearby charge sensor.

To perform energy selective spin readout, or Zeeman readout[21], the $\{\uparrow,\downarrow\}$-spin states of a charge confined in a QD are separated in energy using a large magnetic field, and the QD potential is tuned such that only spin-$\downarrow$ electrons are allowed to tunnel off the QD, whereas spin-$\uparrow$ electrons will remain confined within the QD potential (Fig. 35(a)). Due the large energy separation between the two spin-states, when a tunneling event occurs the charge in the QD is quickly replaced by a charge with the opposite spin. A fast charge sensor can therefore detect the interval between these two tunnelling events during which the QD is empty, and thereby identify the initial spin state.

Although conceptually simple, this readout method presents some challenges. First, it requires the energy splitting of the spin states to be larger than the electron thermal energy, which demands low temperatures and large magnetic fields. Second, the precise tuning of the QD energy levels can be very sensitive to charge noise and fluctuations of the dot-electrostatic potential. However, as demonstrated by Ref. 240, if the tunneling rates of the two spin states with the electron

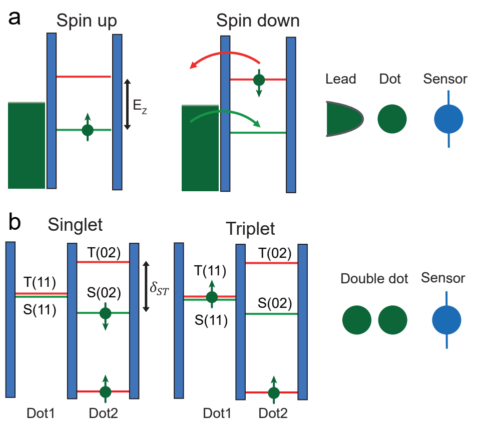

FIG. 35. Schemes for spin-to-charge conversion. (a) Single-spin readout using a charge sensor. In a magnetic field, the spin levels in a QD are separated by Zeeman energy E_Z. (This figure is drawn assuming a negative g-factor, as in GaAs.) If these two levels straddle the Fermi level in a nearby lead, the higher-energy state can decay by electron tunneling. This gives rise to a transient change in the electric field seen by the sensor, and therefore in its resistance. (b) Singlet-triplet readout using a charge sensor. For two electrons in the same dot, there is a splitting δ_{ST} between the singlet and triplet levels. In a DQD with the level alignment shown, a singlet spin state therefore favors a (02) charge occupation while a triplet state favors (11).These two configurations are distinguished by the sensor.

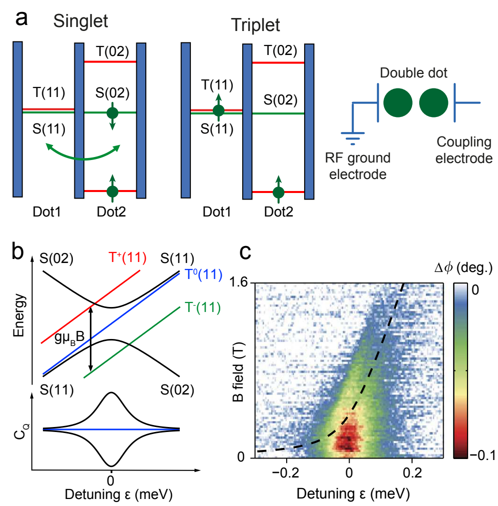

FIG. 36. Dispersive singlet-triplet readout. (a) Energy diagram of the four charge-spin configurations of two electrons in a DQD at $B = 0$. The brackets (left, right) give the charge occupation of each QD for each state. The green arrows symbolise the tunneling between the singlet states. The polarizability of a DQD depends on whether a charge can tunnel in response to a small electric field. With the level alignment shown, this only happens for the singlet state. This gives rise to a spin-dependent admittance across the DQD, which can be measured using an rf resonator attached to a coupling electrode (sketched on the right). (b) Top: Energy levels of the two-electron configurations as a function of detuning ε (top). The magnetic field separates the three triplet states $\mathrm{T}^-(11)$, $\mathrm{T}^0(11)$ and $\mathrm{T}^+(11)$ (We ignore the higher-energy T(02) states for simplicity.). Bottom: Corresponding quantum capacitance C_Q. The quantum capacitances of $\mathrm{T}^-(11)$, $\mathrm{T}^0(11)$ and $\mathrm{T}^+(11)$ overlap. (c) Dispersive measurement of a double quantum dot in Pauli spin blockade as a function of detuning ε and magnetic field B.[32]. The dashed line indicates the degeneracy of the lowest energy singlet and triplet states. M. G. House, T. Kobayashi, B. Weber, S. J. Hile, T. F. Watson, J. van der Heijden, S. Rogge, M. Y. Simmons, Nature Communications, 6, 8848, 2015; licensed under a Creative Commons Attribution (CC BY) license.

reservoir are very different, both these conditions can be relaxed resulting in a more robust readout-mechanism.

Another popular method for spin-to-charge conversion, typically used in DQD systems, uses current rectification due to Pauli spin blockade (Fig. 35(b)). Consider two electrons confined in a DQD. The combination of two-particle charge and spin degrees of freedom can be classified respectively as separated and joint singlets, S(11) and S(02), and separated and joint triplets, T(11) and T(02). The latter two each has a degeneracy of three which is broken by a magnetic field. Pauli selection rules forbid the existence of two fermions with the same quantum numbers, forcing the second electron to a higher orbital state in the T(02) configuration which is separated from S(02) by an energy δ_{ST}[241]. On the other hand, S(11) and T(11) are quasi-degenerate since the spatial separation of the participant spins results in a vanishing small δ_{ST}.

Because Pauli exclusion raises the energy of the T(02) state compared to the T(11) and S(11) states, spin conservation requires the T(11) state to remain blocked while the singlet S(11) is allowed to tunnel to the state S(02). A charge sensor can then detect the difference between these two static charge configurations, either T(11) or S(02). Note how the spin state is now correlated to the charge configuration.

2. *Dispersive qubit readout*

Spin readout via Pauli spin blockade can also be measured dispersively without a charge sensor. In this case, the DQD is configured so that the S(11) and S(02) configurations are degenerate (Fig. 36(a)), with the weighting of these two configurations depending on the electric field. As long as the singlet (triplet) coupling $\Delta_{\mathrm{S(T)}} < \delta_{\mathrm{ST}}$, the system is free to tunnel between the S(11) and S(02) charge states, whereas a system in the T(11) cannot tunnel to the T(02) state unless extra energy is provided.

As we saw in Section IV C, a double quantum dot presents a quantum capacitance

$$C_{\mathrm{Q}} = (e\alpha')^2 \frac{dP_2}{d\varepsilon}, \tag{156}$$

which depends on how the charge distribution among QDs reacts to a change in detuning induced by the rf signal. Hence, tunneling between singlets manifests itself as a quantum capacitance, allowing these the singlet and triplet spin configurations to be distinguished. In Fig. 36(b), we plot the two-electron spectrum as a function of detuning. The plot includes the singlet eigenenergies (Eq. 81) and the uncoupled triplet energies $E_{\mathrm{T0}} = \varepsilon/2$, $E_{\mathrm{T}\pm} = \varepsilon/2 \pm g\mu_{\mathrm{B}}B$ where μ_{B} is the Bohr magneton, g the electron g-factor and B the external magnetic field. In the low temperature limit, Eq. (156) can be conveniently generalized t[101],

$$C_{\mathrm{Q}} = -(e\alpha')^2 \sum_{\mathrm{i}} \frac{\partial^2 E_i}{\partial \varepsilon^2} P_i \tag{157}$$

where E_i and P_i are the eigenenergies and their occupation probabilities, respectively. As we see, at zero detuning, the singlet ground (S-) and excited states (S+) present a quantum capacitance

$$C_{\mathrm{Q,S\pm}} = \pm \frac{(e\alpha')^2}{2\Delta_{\mathrm{S}}}, \tag{158}$$

whereas the triplets have zero quantum capacitance. The difference in quantum capacitance can be determined using reflectometry when the system is biased at zero detuning. At $B = 0$ T, the overall ground state is a singlet ground state and electrons are free to tunnel between the S(11) and S(02) states, resulting in a net phase shift of the resonator, see Fig 36(c). For magnetic fields $g\mu_{\mathrm{B}}B > \Delta_{\mathrm{S}}/2$, $\mathrm{T}^-(11)$ becomes the ground state and the phase shift tends to zero. The signal vanishes asymmetrically from the (11) side tracking the position in $\varepsilon - B$ space of the singlet-triplet crossing.

In-situ dispersive spin readout has been achieved in double quantum dots in InAs[242], GaAs[85] and Si[111,146,243,244]. Furthermore, dispersive Pauli spin blockade has been used for single-shot spin readout[112,135,180].

B. Single-shot readout

Fault-tolerant quantum computing requires the state of individual qubits to be read out in single-shot mode, meaning that the state of a single qubit, i.e. 0 or 1, must be determined from one iteration of the measurement. For error correction to be scalable, the fidelity of this process, i.e. the probability to correctly identify the qubit state, must be well above a threshold determined by the error-correction protocol[245]. The acceptable error rate for measurements (so-called 'class-1 errors'[245]) depends on the fidelity of other gate operations but is likely to be around 0.1%, meaning that fast readout needs to attain a fidelity of 99.9% or better. Furthermore, this process should happen within a single repetition time of the error-correction cycle, which means within the qubit coherence time. This is one of the most demanding and important applications of fast readout, and requires sufficient sensitivity to detect a small signal and sufficient bandwidth to respond within the qubit coherence time.

Unfortunately, the short relaxation lifetime T_1 of the state being measured often makes single-shot measurements challenging, and if the signal-to-noise ratio is too small, the state cannot accurately be determined within this time. Electron spin lifetimes can be greater than 1 s in gate-defined quantum dots[24,122] or 30 s in donor-based devices[246], but are typically of the order of 1 ms or less in qubit devices[112,139,180,247].

An example of a single-shot spin qubit measurement is shown in Fig. 37[72]. The qubit in this case is a singlet-triplet qubit[23] measured using an rf-QPC charge sensor in the scheme of Fig. 35(b). The qubit is controlled by rapidly adjusting the detuning $\varepsilon(t)$ in a cycle that generates an approximately equal mixture of the two states (Fig. 37(a)). To read out the state at the end of each cycle, ε is held constant and the illumination tone V_{in} is turned on. This leads to a demodulated signal $V_{\mathrm{I}}(t)$ whose average value during the readout step is low or high depending which state was generated.

The optimum integration time τ_{int} is long enough to minimise electrical noise but short enough that the qubit usually has not decayed during the measurement. Figure 37(b) illustrates this trade-off by plotting a histogram of averaged V_{I} values for different choices of τ_{int}. Similar to Fig. 24(e-f), the distribution shows two peaks at $V_{\mathrm{IF}}^{\mathrm{T}}$ and $V_{\mathrm{IF}}^{\mathrm{S}}$ corresponding to the two qubit states, with each becoming narrower as the integration time increases. However, unlike in Fig. 24, the two peaks do not have equal weighting; the right-hand peak becomes weaker as T states are given more time to decay, leading them to be misidentified as S.

The optimum value of τ_{int} is chosen by maximising the fidelity (see Eq. (171))

$$\mathscr{F} \equiv \frac{F_{\mathrm{S}}}{2} + \frac{F_{\mathrm{T}}}{2} \tag{159}$$

where F_{S} and F_{T} are the fidelity associated with identifying with success the S or T states, respectively. It leads to the histogram in Fig. 37(c). Typically, a threshold voltage V_T is chosen between the two peaks, with outcomes below threshold interpreted as S and outomes above threshold as T. F_{S} and F_{T} are

$$F_{\mathrm{S}} = 1 - \int_{V_T}^{\infty} n_{\mathrm{S}}(V)dV, \quad F_{\mathrm{T}} = 1 - \int_{-\infty}^{V_T} n_{\mathrm{T}}(V)dV \tag{160}$$

where n_{S} and n_{T} are respectively the Singlet and Triplet probability density. Here n_{S} can modeled as a noise-broadened Gaussian[72] with standard deviation σ and centered on $V_{\mathrm{IF}}^{\mathrm{S}}$:

$$n_{\mathrm{S}}(V_{\mathrm{IF}}) = (1 - \langle P_{\mathrm{T}} \rangle) e^{-\frac{(V_{\mathrm{IF}} - V_{\mathrm{IF}}^{\mathrm{S}})^2}{2\sigma^2}} \frac{1}{\sqrt{2\pi}\sigma} \tag{161}$$

where $\langle P_{\mathrm{T}} \rangle$ is the Triplet probability over all the experiment. The Triplet outcomes n_{T}, need to take into account relaxation

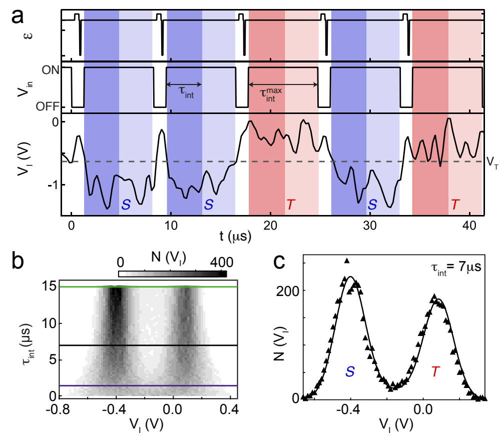

FIG. 37. (a) Series of single-shot measurements of a spin qubit. The unshaded portion of each cycle marks the interval during which a spin superposition is generated and projectively converted to a charge state; the shaded portion marks when the qubit is measured. Top: Detuning ε as a function of time. The cycle shown generates an approximately equal mixture of the two states. Middle: Level of the illumination signal. Bottom: Demodulated reflected signal V_I. Each iteration is identified as singlet S or triplet T depending whether the average level is below or above the threshold V_T. The integration time τ_int is adjusted up to a maximum value $\tau_\mathrm{M}^\mathrm{max}$. (b) Histogram of average readout signal for different choices of τ_int. Here $N(V_\mathrm{I})$ is the number of counts in each bin of the histogram. The purple line at $\tau_\mathrm{int} = 1.5~\mu$s marks a choice for which the two states are insufficiently distinct; the green line at $\tau_\mathrm{int} = 15~\mu$s marks a choice for which decay from T to S has significantly degraded the fidelity. (c) Histogram at $\tau_\mathrm{int} = 7~\mu$s (black line in (b)), for which the fidelity is maximal. Reproduced with permission from Phys. Rev. Lett. 103, 160503 (2009). Copyright 2009 American Physical Society.

during τ_int:

$$n_\mathrm{T}(V_\mathrm{IF}) = e^{-\frac{\tau_\mathrm{int}}{T_1}} \langle P_\mathrm{T}\rangle e^{-\frac{(V_\mathrm{IF}-V_\mathrm{IF}^\mathrm{T})^2}{2\sigma^2}} \frac{1}{\sqrt{2\pi}\sigma} + \int_{V_\mathrm{IF}^\mathrm{S}}^{V_\mathrm{IF}^\mathrm{T}} \frac{\tau_\mathrm{int}}{T_1} \frac{\langle P_\mathrm{T}\rangle}{\Delta V_\mathrm{IF}} e^{-\frac{(V-V_\mathrm{IF}^\mathrm{S})}{\Delta V_\mathrm{IF}}\frac{\tau_\mathrm{int}}{T_1}} e^{-\frac{(V_\mathrm{IF}-V)^2}{2\sigma^2}} \frac{dV}{\sqrt{2\pi}\sigma}, \tag{162}$$

where $\Delta V_\mathrm{IF} = V_\mathrm{IF}^\mathrm{T} - V_\mathrm{IF}^\mathrm{S}$.

In this experiment with a qubit relaxation time $T_1 = 34~\mu$s, the maximum fidelity is $\mathscr{F} \approx 95\%$ for $\tau_\mathrm{int} = 7~\mu$s. Experiments since then have reached higher values (see Supplementary Table SI). The optimum strategy for identifying the qubit state from the voltage record, which is more sophisticated than the simple average used in Fig. 37, is discussed in Supplementary Section S3 B 4. Currently the record fidelity for reading out a singlet-triplet qubit is 99.86%[248], or 99.5 % in a short array[76].

Single-shot measurements of a single spin using energy-selective readout, require a different fidelity analysis. For energy-selective readout, charge sensors are necessary. The experiment needs to detect the reflected voltage signal (or current if dc charge sensors are used) occurring between the two charge-tunneling events in Fig. 35(a). The bandwidth needs to be sufficiently large to resolve the transient during which the electron resides outside the QD. The important parameters are therefore the tunneling in and out times, the integration time per point, the relaxation time and the voltage threshold to define whether a measurement outcome is called a spin up or down. The optimization of these parameters and the evaluation of the corresponding readout fidelity are now commonly performed using Monte Carlo simulations[249]. Currently the highest fidelity reported for single-spin qubits using energy-selective readout is 99.8 % in 65 ms for a p-donor in silicon[246], and 97 % in 1.5 μs using an rf-SET[250].

C. Examples of state-of-the art experiments

1. Readout of four qubits with charge sensors

While in state-of-the-art silicon devices most qubits are operated one at a time, GaAs devices have recently allowed the simultaneous operation (and readout) of up to four singlet-triplet qubits[68]. The device shown in Fig. 38(a) employs a multi-electron coupler (elongated QD highlighted in green) to space four DQDs sufficiently far apart to allow individual qubit manipulation with minimal cross-talk between electrodes. Each DQD implements one singlet-triplet qubit, with proximal charge-sensing QDs that are read out simultaneously by frequency-multiplexed reflectometry. (The high-frequency PCB sample holder for this experiment is commercially available from QDevil[251].) In this experiment, one contact lead of each sensor is wirebonded to an SMD resonator (with a unique inductance) on the PCB sample holder, and all four resonators are capacitively coupled to one reflectometry channel of the cryostat. The measured reflectometry signal (Fig. 38(b)) shows four dips sufficiently spaced in frequency to allow qubit-resolved single-shot readout using separate carrier signals injected via the same line. This work demonstrates not only that all four qubits can be rotated simultaneously with similar speed (Fig. 38(c) shows a π rotation within 15 ns), but also that all four qubits can be read out in single-shot mode simultaneously (in Fig. 38(e), each data point is an average of 512 single-shot outcomes).

The ability to combine time-domain and frequency-domain multiplexing means that reflectometry will likely continue to play an important readout tool as qubit devices are scaled to 100-qubit processors or even beyond 1000 qubits.

2. Spin readout with superconducting on-chip microwave resonators

In Fig. 39(a), a silicon DQD is capacitively coupled to a 5.7-GHz on-chip superconducting resonator that is capacitively coupled to transmission line[136]. Transmission measurements S_{21} can distinguish singlet and triplet states with high sensitivity and temporal response, as exemplified by several single-

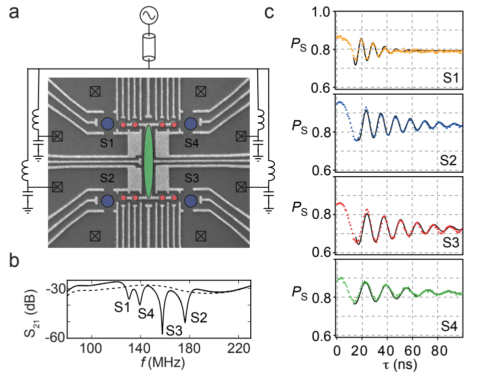

FIG. 38. (a) Four singlet-triplet qubits (red double dots) with proximal sensor dots (blue dots) implemented in a GaAs heterostructure, allowing simultaneous four-qubit operation and four-qubit single-shot readout via frequency multiplexing using a commercial PCB sample holder system[68]. (b) Each charge sensor is wirebonded to a tank circuit with unique resonance frequency, allowing simultaneous readout of all four sensors (S1-4) via frequency multiplexing. (c) Simultaneous exchange rotations of all four qubits induced by suitable detuning pulses (not shown). Each data point represents the average of many single-shot outcomes obtained for each qubit. Federico Fedele, Anasua Chatterjee, Saeed Fallahi, Geoffrey C. Gardner, Michael J. Manfra, and Ferdinand Kuemmeth, PRX Quantum 2, 040306, 2021; licensed under a Creative Commons Attribution (CC BY) license.

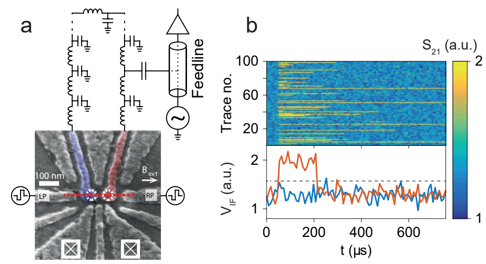

FIG. 39. (a) A silicon double quantum dot (dashed white circles) is capacitively coupled to an on-chip superconducting resonator (shown here as a series of LC elements), which is monitored via a transmission line. Detuning pulses applied to LP and RP configure the double dot in its readout position where the charge associated with spin-singlet states can tunnel while spin-triplet states are Pauli blocked. (b) The tunnel and dispersive capacitance associated with the singlet state yield an enhancement of the transmission amplitude $|S_{21}|$, corresponding to a single-shot readout fidelity >98% in 6 μs. Reproduced with permission from Nat. Nanotechnol. 14, 742–746 (2019). Copyright (2019) by Springer Nature.

shot readout traces in Fig. 39(b). In this experiment, a random spin configuration is repeatedly initialized and measured after 50 μs. Singlet and triplet states are then distinguished by a different response in the resonator transmission. In the top panel, blue pixels are associated with triplet statesand yellow pixels are associated with singlet states. Two individual line-cuts in the bottom panel illustrate the difference in the resonator response. In this example, the resonator quality factor (2600) yields a maximum bandwith of 2 MHz. In conjunction with an estimated spin relaxation time of 0.16 ms, this allowed single-shot read-out of the two-electron spin state with an average fidelity of >98% with an integration time of 6 μs.

Because the carrier frequency of 5.7 GHz exceeds the inter-dot tunnel coupling (2 GHz), the system is not in the adiabatic limit during readout, i.e. in addition to the quantum capacitance associated with the curvature of the dispersion relation, there are significant contributions from the tunnelling capacitance. See Refs.[252,253] to understand the coupling between the spin of the electrons in the DQDs and the photons in the resonator.

IX. RAPID DETECTION OF IMPORTANT QUANTUM PHENOMENA

So far, our examples have focused on the technical aspects of high-frequency reflectometry, and were chosen to illustrate important variations and optimizations rather then the breadth of physical insights that can be gained with this technique. In this section, we describe different condensed-matter experiments that have already benefited from this powerful measurement tool. Our selection is by no means exhaustive, and intends to inspire new applications in diverse subject areas.

A. Noise-protected superconducting qubits

The coupling between superconducting qubits and superconducting microwave resonators plays a key role in current quantum processors for enabling coherent two-qubit gates and efficient qubit readout. A key challenge is maintaining high control and readout fidelities while increasing the number of qubits. As an alternative to conventional superconducting qubits (such as Xmons, transmons, etc.[255]), new superconducting circuits are being studied that combine inductors, capacitors, and Josephson junctions in such a way that the resulting two-level system is more robust to environmental noise. The reduced error rates associated with such qubits may then possibly simplify the scaling towards larger qubit arrays. The key idea behind such noise-protected superconducting qubits is to simultaneously suppress qubit relaxation and qubit dephasing by creating special symmetries in the effective circuit ("error correction by hardware engineering")[254,256–259]. For qubits protected by the topologies of the underlying system Hamiltonian, see the following section on

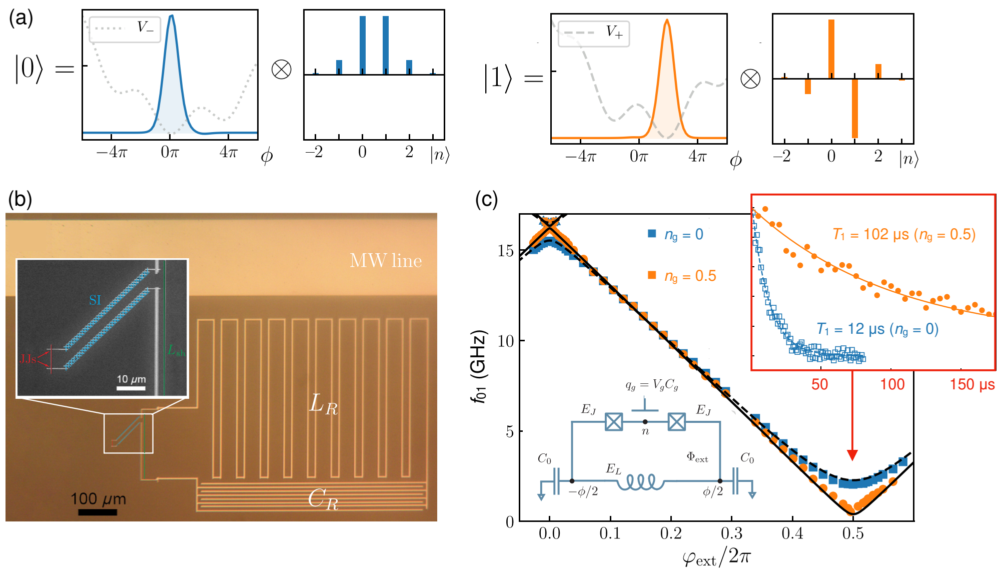

FIG. 40. A protected superconducting qubit, here implemented as a bifluxon qubit[254]. (a) For a suitable symmetric operating point, the two qubit states $|0\rangle$ and $|1\rangle$ become nearly degenerate in energy. Visualization of their flux-like and and charge-like wavefunctions shows the origin of their protection: the flux-like parts (in the basis of the phase difference ϕ across the superinductor, see inset of (c)) are localized in different minima of the fluxonium potential V, and the charge-like parts are symmetric ($|0\rangle$) and antisymmetric ($|1\rangle$) (in the basis of number of Cooper pairs on the Cooper-pair box, n). (b) Experimental implementation of the bifluxon qubit (inset), readout resonator (L_R, C_R), and microstrip transmission line (MW), all fabricated in a single multi-angle Al-evaporation process. The Cooper-pair box (red in inset) is defined by two small Josephson junctions, whereas the superinductor (SI) is implemented as an array of 122 larger Josephson junctions (blue in inset). During one cooldown of such a chip multiple qubits can be read out via the same microwave line, by using different resonance frequencies for each readout resonator. (c) Experimental signatures of the protection include a decrease of the qubit splitting, f_{01}, as the symmetry point is approached ($\varphi_{\rm ext} = \pi, n_g = 0.5$), and an increase of the qubit relaxation time T_1 (red inset). To operate this qubit and take measurements like this, the gate voltage is pulsed away from $n_g = 0.5$ to temporarily break the protection of the qubit and make it interact with the control and readout signals (not shown). Konstantin Kalashnikov, Wen Ting Hsieh, Wenyuan Zhang, Wen-Sen Lu, Plamen Kamenov, Agustin Di Paolo, Alexandre Blais, Michael E. Gershenson, and Matthew Bell, PRX Quantum 1, 010307, 2020; licensed under a Creative Commons Attribution (CC BY) license.

Majorana qubits. The hope of error correction on the hardware level is to eventually engineer circuits comprising frustrated chains of Josephson junctions[260,261] such that not only quantum memory is protected, but also gate operations[262,263].

To achieve a good quantum memory, both bit-flip errors (qubit relaxation) and phase errors (qubit dephasing) need to be suppressed. While energy relaxation can be suppressed by decreasing the wavefunction overlap between the two qubit states (for example by *localizing* qubit states in distinct minima of the qubit potential, as in the "heavy fluxonium" qubit[264]), and dephasing can be exponentially suppressed by *delocalizing* the qubit wavefunction (for example in charge space, as in the "transmon" qubit[265]), the simultaneous suppression of both errors requires more complicated "few-body" systems such as the 0-π qubit[263]. In such qubits, multiple Josephson junctions are connected by superconducting loops in such a way that two nearly degenerate ground states emerge that are localized in distinct minima of a superconducting phase difference, namely at zero phase and at π. The exponentially small qubit splitting combined with a robustness to weak local perturbations should make 0-π qubits highly resistant to decoherence arising from local noise. Theoretically, such qubits also offer routes towards topologically protected gate operations, although this has not yet been demonstrated experimentally.

Experimentally, the characterization of protected qubits is complicated by its very protection: near its (protective) symmetry point, not only does the qubit splitting become impractically small (preventing the typical microwave techniques such as two-tone spectroscopy), but also its coupling to the control pulses (thereby preventing straightforward Hahn echo experiments to study dephasing characteristics, for example). To maintain the ability to control and read out such qubits, they have been intentionally mistuned from the protected symmetry such that noise protection can be quantified[257,258]. (In the pioneering devices in Ref. 256, the asymmetry naturally arose from imperfections in the Josephson rhombus arrays.)

An interesting alternative to 0-π qubits protected by the parity of Cooper pairs (as in Refs. 257 and 258), are 0-π qubits protected by the parity of flux quanta, as in the bifluxon qubit[254]. Here, a superconducting loop comprises a Cooper-pair box and a superinductor[266], suppressing tunneling of flux quanta between the outside and inside of the loop (and errors that would be generated by such tunneling) for a particular charge tuning of the Cooper-pair box. In Figure 40, the gate-induced charge of the Cooper-pair box, n_g, is controlled by a gate voltage, and the applied flux through the loop (Φ_ext, controlled by an external magnetic field) induces a phase winding φ_ext along the loop. At $\varphi_\mathrm{ext} = \pi$, the qubit splitting, f_{01}, is observed to drop dramatically at the symmetric operating point $n_\mathrm{g} = 0.5$ (Fig. 40(c)), while the qubit relaxation time, T_1, increases significantly (red inset). The underlying protection at that symmetry point can be understood by visualizing the wavefunctions of the qubit states as tensor products of a flux-like and charge-like part (Fig. 40(a)), and noting that the flux-like part of $|0\rangle$ is localized in a different minimum than $|1\rangle$ while the charge-like parts are symmetric ($|0\rangle$) and anti-symmetric ($|1\rangle$) (when expressed in the basis of number of Cooper pairs $|n\rangle$ on the Cooper-pair box).

The readout of the bifluxon qubit shown in Figure 40 is performed by inductively coupling a readout resonator (consisting of L_R and C_R elements as shown on the micrograph) to a microwave transmission line (MW line). The properties of the readout resonator change if the state of the qubit changes. The Cooper-pair box (red in the inset) is connected via two Josephson junctions to a superinductor (blue), which is implemented as an array of 122 larger Josephson junctions. The bifluxon qubit, readout resonator, and microstrip transmission lines are fabricated in a single multiangle electron-beam deposition of aluminum through a liftoff mask. In the transmission measurements, the microwave signals travel along the microstrip line and couple to the readout resonators of up to five different bifluxon qubits located on the same chip. By using different resonant frequencies of the readout resonators, the qubits can be individually addressed and characterized in the same cooldown. In this case, frequency-multiplexing is not essential to the operation of the device, but is simply an experimental trick to increase the chances of finding one device with suitable device characteristics (symmetry of the two small Josephson junctions, in this case).

B. Topological superconductivity and Majorana devices

One keenly studied sub-field of condensed-matter physics is that of topological materials[269,270], whose coherence and time-dependent properties are largely unexplored despite their potential applications in inherently fault-tolerant quantum computation. To date most experiments on topological systems, such as those seeking non-abelian Majorana bound states in nanowires or 2DEGs, focus on transport signatures, even though topologically-protected quantum computing[271] will require time-domain control such as braiding and single-shot parity measurements. Several considerations drive the development of fast parity-to-charge detectors: first, readout times can be as low as microseconds, thereby potentially mitigating quasiparticle poisoning of Majorana modes that occurs on longer time scales. Second, quantum non-demolition measurements become possible with high SNR, which is crucial for measurement-based quantum computation based on topological superconductivity. Third, no matter how long the coherence times of protected qubits ultimately may be, in order to operate many qubit cycles within reasonable timescales, fast qubit readout of charge or current will be beneficial.

If a topological superconductor hosting two physically separated Majorana zero modes is sufficiently small, then the Coulomb charging energy associated with such a “Majorana island" can be utilized to create two degenerate ground states that differ in their total occupation number by one electron. (This is in contrast to trivial superconducting islands, where the addition or removal of one electron would require an energy related to the superconducting gap.) Liang Fu realized that the injection of an electron into one Majorana mode, and simultaneous extraction of an electron from the other mode, constitutes a non-local phase-coherent electron transfer[272]. This prediction of Majorana-assisted electron teleportation inspired numerous other proposals that suggest *conductance measurements* and *charge sensing* of Majorana islands as a tool to study non-local and non-abelian properties of Majorana modes. For example, in the proposal by David Aasen et al., superconducting double-dot devices in which the various tunnel couplings (i.e. Josephson couplings and Majorana couplings) can be controlled by gate voltages play a central role, allowing parity-to-charge conversion for charge sensing experiments that are targeted towards the detection of Majorana fusion rules (which are unique to non-Abelian anyons) and towards the coherent operation of a prototype topological qubit[273]. Not surprisingly, the ability of reflectometry to reveal conductance changes or charge changes of quantum devices is therefore relevant for studying topological superconductivity.

For example, Majorana readout based on conductance measurements has been proposed for so-called Majorana box qubits. The simplest box qubit consists of an island of topological superconductor hosting four Majorana bound states at four different locations[274]. Two of them are coupled via controllable tunnel barriers to a semiconducting region, such that they can participate in conductance measurements. Because the combination of two Majorana operators (γ_i) constitutes one fermionic operator, the even parity state of the four-Majorana box is two-fold degenerate, thereby encoding one qubit. Importantly, it can be arranged such that the transmission phase of the two Majorana states that participate in transport depends on the state of the qubit. Interferometric measurement of the device conductance would therefore allow *readout* of the state of the box qubit. The functionalities can be extended to qubit *control* by hosting six Majorana bound states on the topological island, and by connecting three of them to gate-controlled semiconducting quantum dots. Conductance measurements that involve pairs of these three Ma-

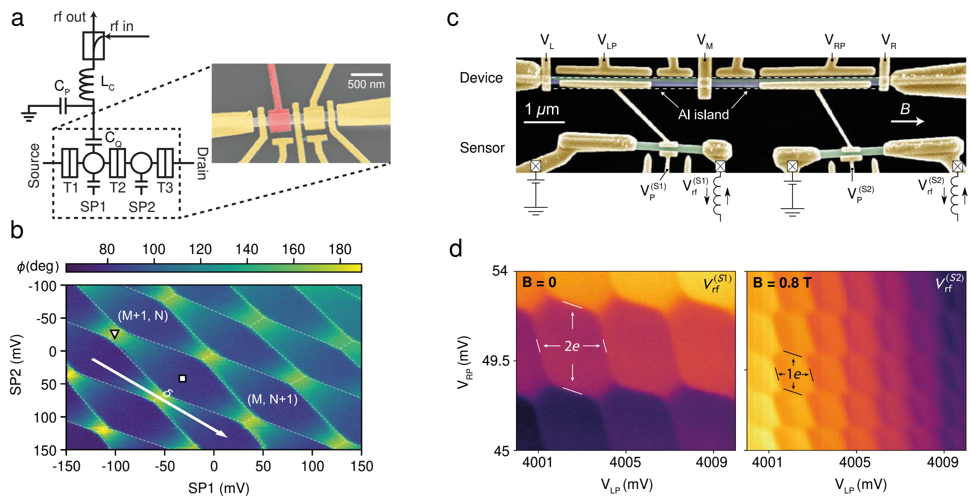

FIG. 41. Nanowire devices with high-frequency reflectometry readout to investigate Majorana modes. (a) SEM of an InAs nanowire double dot to demonstrate rapid detection of interdot tunneling (here without superconductivity and without Majorana modes)[267]. One of the quantum dots is capacitively coupled (via the red gate electrode) to a 0.4-GHz superconducting resonator (L_C, C_P) that is probed by reflectometry. Interdot tunneling (modeled by C_Q) results in a substantial shift of the resonance frequency, and therefore of reflected carrier phase ϕ. (b) Charge stability diagram measured by sweeping the two plunger gates, SP1 vs SP2. Tunneling at charge degeneracy (▽) can be distinguished from Coulomb blockade (□) by sampling the reflected carrier phase ϕ for a short time (in this work, achieving a SNR of 2 within 1 μs for a carrier power of -109 dBm and 5 GHz interdot tunneling). Damaz de Jong, Jasper van Veen, Luca Binci, Amrita Singh, Peter Krogstrup, Leo P. Kouwenhoven, Wolfgang Pfaff, and John D. Watson, Phys. Rev. Applied 11, 044061, 2019; licensed under a Creative Commons Attribution (CC BY) license. (c) Superconducting double dot fabricated from a hybrid InAs/Al nanowire (Device) suitable for investigating Majorana modes[80]. The charge occupation is measured by two InAs nanowire quantum dots (Sensor) that are monitored using different reflectometry frequencies (40 and 60 MHz in this work), each yielding a reflectometry signal (namely $V_{rf}^{(S1)}$ and $V_{rf}^{(S2)}$ in panel d). (d) Charge stability diagram measured at $B = 0$ and $B = 0.8$ T via the rf response of the right and left sensor respectively, for weak interdot tunneling. By studying the transition from $2e$-periodic Coulomb valleys at $B = 0$ to $1e$-periodic Coulomb valleys at finite field, one can in principle measure the interaction energy within Majorana pairs[268]. Reproduced with permission from Phys. Rev. Applied 11, 064011 (2019). Copyright 2019 American Physical Society.

jorana states would then implement readout of different Pauli operators ($\hat{x} = i\gamma_1\gamma_2$, $\hat{y} = i\gamma_3\gamma_1$, $\hat{z} = i\gamma_2\gamma_3$). Although never realized in practice, such gate-controlled measurements in the time domain would resemble, from an operational viewpoint, certain gate-controlled experiments in the field of spin qubits, with rf reflectometry providing useful tools for accurately and quickly detecting conductance changes.

Motivated by the intriguing roles of Josephson couplings and Majorana couplings between topological superconductors, readout schemes that potentially detect the associated dispersive shifts of rf resonators or superconducting microwave cavities have been proposed. In the specific case of reflectometry-based readout, Ref.[162] considers a popular scheme for Majorana readout, where zero modes (γ_1 and γ_2) are coupled to an auxiliary quantum dot. This setup can be used to read out the joint parity of the two Majorana zero modes by tunnel coupling to an auxiliary quantum dot. Calculations of the parity-dependent capacitances of the coupled system (which depend on the on-site energy of the readout dot and the complex-valued but tunable tunnel coupling between the dot and γ_i) and of the ensuing reflectances are given in Ref.[162], along with the estimated readout fidelity.

Experimentally, rf readout has been applied to Majorana-type devices. Examples in this direction include measurements of the tunneling rates in InAs nanowire devices, which are an early test bed to search for Majorana bound states. Another example is the development of superconducting resonators that can withstand magnetic fields in the range of 1-2 T where Majorana bound states occur.

Two studies carried out in InAs nanowires are shown in Fig. 41. The first study[267] (Fig. 41 (a-b)) utilises dispersive charge sensing, relying on a quantum dot charge sensor controlled with a top gate connected to a standard off-chip lumped-element resonant circuit. The resulting dispersive shift of the resonance frequency was significant (≈1 MHz, of the order of the resonator linewidth), corresponding to a detected phase shift of the reflectometry signal of nearly 180 degrees. The experimental demonstration to resolve the tunneling-dependent quantum capacitance C_Q paves the way to detecting coherent Majorana couplings between topological islands.

A second study[80] (Fig. 41 (c-d)) used a proximal nanowire charge sensor instead of gate-based reflectometry, with high readout SNR reported up to 1 T. In this study, the evolution of Coulomb blockade regions could be studied without a current flow through the device. There was a transition from $2e$ periodicity at zero magnetic field to $1e$ periodicity at finite axial magnetic fields, as experimentally observed in Fig. 41(d). When accompanied by the hard superconducting gap remaining, this change in periodicity has been theorized as an indicator for transitioning between trivial and topological superconductivity.

Lastly, depending on the bound state occupation, the fermion parity of a nanowire Josephson junction can be even or odd. Dynamic polarization of this even/odd parity and its single-shot detection has been very recently demonstrated, but for Andreev bound states, with up to 94% fidelity, with measurements performed via a superconducting LC resonator[275].

While these experiments show that fast and high-SNR measurements based on reflectometry potentially allow the identification of topological properties, they have not yet been applied to complex experiments such as braiding or the demonstration of fractional statistics.

C. Noise experiments

Electrical noise itself is a valuable source of information associated with different physical phenomena[50,277]. Shot noise, which results from the discreteness of charge carriers, leads to current fluctuations with spectral density $S_{II}^{\mathrm{N}} = F2qI$ (see Eq. (51)), where I is the average current and q is the charge q of the particles (or quasiparticles) carrying that current. By measuring S_{II}^{N} in a situation in which the Fano factor F is known, the charge q can be deduced. Usually the current is carried by electrons with charge $q = e$, but in some correlated states the excitations are quasiparticles with a fractional charge. A particularly clear example is the $\nu = 1/3$ fractional quantum Hall state, for which the carrier charge is[276,278] $q = e/3$

The experiment that confirmed this fact measured the shot noise generated by a tunnel barrier between two regions of two-dimensional electron gas in the fractional quantum Hall state. The tunnel barrier acts as a broadband noise source. It is measured using a cryogenic voltage amplifier as in Fig. 42(a). The current noise is transduced to a voltage noise by the real part of the amplifier input impedance in parallel with the sample impedance, together represented by the resistor R_{C}. As with the rf-SET, the bandwidth of the measurement is limited by the capacitance C_{line} of the transmission line, meaning that if the amplifier is directly connected to the noise source, it can only detect current noise up to a frequency $\sim 1/R_{\mathrm{C}}C_{\mathrm{line}}$, which would be ~ 30 kHz in this experiment. In this frequency range, pink noise due to background charges usually overwhelms the shot noise of interest, making precise measurements impossible. This problem is circumvented by inserting an inductor in parallel with the line capacitance, thus forming a resonant tank circuit and shifting the range of frequencies over which the experiment is sensitive up to the tank circuit's resonant frequency, which in this case is ~ 4 MHz. The sensitive bandwidth is unchanged. Comparing the shot noise measured in this way with Eq. (51) implies a quasiparticle charge $q = e/3$[276].

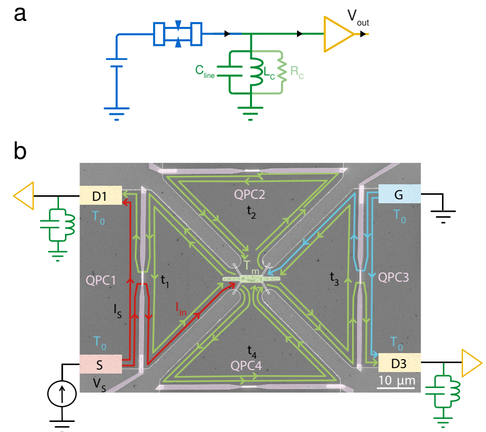

FIG. 42. (a) Schematic of a shot noise measurement circuit[276]. The tank circuit is formed from the parasitic transmission line capacitance C_{line}, the resistance Rc of the device in parallel with the real part of the amplifier input impedance, and an added inductor L_{C}. In this circuit, the amplifier is sensitive to device noise within a bandwidth of order $1/R_{\mathrm{C}}C_{\mathrm{line}}$ centered on the frequency $f_{\mathrm{r}} = 1/2\pi L_{\mathrm{C}}C_{\mathrm{line}}$. By measuring the voltage noise integrated across this bandwidth, the spectral density $S_{II}(f_{\mathrm{r}})$ can be inferred. (b) An SEM micrograph of a four-arm device fabricated in GaAs, with a small floating contact lead at its center (green; the depleting gates underneath are not visible), a quantum point contact (QPC) in each arm (an air-bridge shorts the two sides of the split-gate) and source (S1), drains (D1, D2) and ground (G) contacts. The device is placed in the quantum Hall regime with filling factor $\nu = 2$ by setting the required magnetic field. QPC2 and QPC4 are fully pinched off while QPC1 and QPC3 transmit only the outmost ballistic chiral quantum Hall edge mode (t_i is the transmission coefficient of QPC$_i$). The Source current (I_{S}, red) impinges on QPC1, which transmits I_{in} that is absorbed in the floating contact. Edge modes (green) at temperature T_{m}, leave the floating contact into the four arms (in arms 2 and 4 they are fully reflected). Cold edge modes, at temperature T_0 (blue) arrive from the grounded contacts. LC circuits at each drain transmit the signal at $f_{\mathrm{r}} = 740$ kHz with a bandwidth $\Delta f = 10-30$ kHz. Panel (b) Reproduced with permission from Nature 545, 75–79 (2017). Copyright 2017 Springer Nature.

While measuring shot noise gives information about the charge carriers in a device, measuring thermal noise gives information about their temperature. This means that noise measurements can be used to study how heat flows in quantum devices. One example is the measurement of quantised heat transport by anyonic carriers[279]. As shown in Fig. 42(b), resonant circuits at the drain electrodes of a 2DEG gated by two QPCs, QPC1 and QPC2, are used to filter the chiral ballistic

1D edge modes that transmit the carriers under high magnetic field. These edge modes are at an equilibrium temperature T_N, where the power dissipated in the central floating contact is equal to the power carried by phonons and the chiral edge modes. Since the phononic heat contribution is negligible compared to the strongly-interacting electronic contribution for $T < 35$ mK, the temperature T_N can be determined from thermal noise measurements in one of the arms. These thermal noise measurements, carried out as above, use cold amplifiers to measure thermal voltage fluctuations.

D. Micro- and nanomechanical resonators

Due to their small size and mass, nanomechanical resonators have high mechanical resonance frequencies f_m of the order of hundreds of MHz. It is therefore natural to turn to radio-frequency measurement techniques to measure their motion. Moreover, radio-frequency measurements can provide additional information; an example is the demonstration of coherent mechanical oscillations in carbon nanotubes using IQ demodulation[194,285]. Nanomechanical resonators made of carbon nanotubes, graphene or aluminium sheets find exciting applications in sensing[286,287] and qubit readout[156,288]. The measurement of the mechanical vibrations of carbon nanotubes and nanowires have been used to reveal fundamental properties that can be difficult to probe with transport[289–291]. Current challenges for exploring the foundations of quantum mechanics[292] include measuring mechanical resonators in their quantum ground states of motion[293] or generating a macroscopic quantum superposition of states[294,295]. Some recent proposals also suggest using QDs coupled to a mechanical oscillator as mechanical qubits[296].

Gate reflectometry can be used to monitor the motion of nanomechanical resonators by sensing the change of capacitance between the mechanical resonator and a metallic gate electrode connected to the rf cavity. The sample is illuminated by an input signal at frequency f_in via the gate electrode. The reflected signal contains sidebands at frequencies

$$f_\mathrm{out} = f_\mathrm{in} \pm f_\mathrm{m}. \tag{163}$$

that transduce the displacement of the sample. This techniques works well with large devices, such as metallised SiN membranes[297], for which the capacitance varies considerably with the motion.

It is more challenging to measure smaller devices (such as carbon nanotubes or aluminium nanosheets) where the variation of capacitance with the displacement is small compared to the static capacitance. One solution is to operate on resonance with the mechanical resonator $f_\mathrm{in} \approx f_\mathrm{m}$ while applying a static voltage between the mechanical resonator and a gate electrode[280]. In this case, the mechanical resonator impedance can be expressed using the van Dyke–Butterworth[282] model as a static capacitance C_g in parallel with an LCR circuit[280] (L_m, C_m and R_m) (Fig. 43(a)) with equivalent impedance:

$$\frac{1}{Z_\mathrm{m}} = j\omega C_\mathrm{g} + \frac{1}{j\omega L_\mathrm{m} + \frac{1}{j\omega C_\mathrm{m}} + R_\mathrm{m}}. \tag{164}$$

When f_in is out of resonance with the mechanical resonance frequency, Z_m is large and dominates by $1/j\omega C_\mathrm{g}$. On resonance, the impedance drops to $Z_\mathrm{m}^{-1} \approx R_\mathrm{m}$ allowing detection of the motion. This technique has been employed to detect the motion of an aluminium drum[280] and of carbon nanotubes[281], although it requires tuning the frequency of the rf resonator to $f_\mathrm{r} \approx f_\mathrm{m}$ which can be achieved with *in-situ* tuneable cicuits (see Section V A 2).

In gated semiconducting mechanical resonators, the motion can be transduced into a current modulation I_d emitted by the device. This current is measured with a cryogenic amplifier, similar to the shot noise measurements described in Section IX C, using LCR circuits with resonance frequency f_r. In the *two source method*[283,285,290], the mechanical resonator is biased with an ac voltage at frequency $f_\mathrm{in} = f_\mathrm{r} \pm f_\mathrm{m}$ while the mechanical motion is excited by a second source at frequency f_m (Fig. 43(b)). These two frequencies mix such that the current noise spectrum I_d has a sideband at f_r that is transmitted by the LCR resonator. Alternatively, the LCR circuit can be tuned into resonance with the mechanical resonance frequency $f_\mathrm{r} \approx f_\mathrm{m}$ using *in-situ* tunable elements[194,284] (Fig. 43(c)).

E. Fast thermometry

Already in the early days of dilution refrigerator experiments, it was noticed that high-frequency measurements provide practical solutions for the challenging task of implementing reliable subkelvin thermometry. For example, Johnson noise thermometry utilizes the fluctuation-dissipation theorem, on the principle that the voltage fluctuations of a resistor (i.e. the mean square noise voltage within some suitable bandwidth) are proportional to the resistor's temperature. At low temperatures, the minuscule voltage fluctuations of a resistor can be elegantly converted to frequency fluctuations using the ac Josephson effect (the factor $2e/h$ corresponds to an attractive conversion factor of ≈ 484 MHz/μV), yielding reliable thermometry in the 10 mK range with a measurement noise temperature (response time) of 0.05 mK (50 ms) as early as 1973[300]. While this technique is not based on reflectometry, it loosely fits into the category of high-frequency emission measurements (in this case, via a 19 MHz tank circuit connected to a SQUID amplifier). Another early high-frequency technique (important for microkelvin applications) involves the detection of ^{125}Pt nuclear spin susceptibilities (which follow a Curie law) using pulsed nuclear magnetic resonance techniques, allowing not only determination of nuclar spin temperatures, but also (via the Korringa law) the temperature of the electrons[301].

More recently, efforts have been made to study the effective temperature and time scales associated with different degrees of freedom in small systems (phonon temperature in mechanical resonators, electron temperature in isolated quantum devices, photon temperatures in microwave cavities, etc.). Quantum devices that involve superconductor–insulator–normal metal (SIN) junctions are of particular interest, as they allow fundamental insights (interplay of high

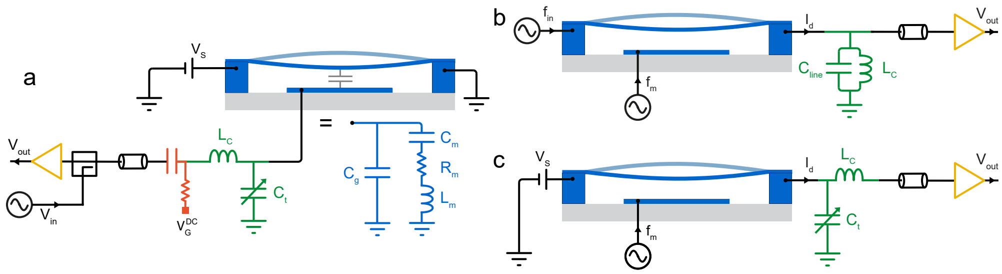

FIG. 43. (a) Schematic of the measurement of the motion of a carbon nanotube mechanical resonator using gate reflectometry[280,281]. An LC resonator made of an inductance L_C and a tunable capacitance C_t is attached to the gate of the device. The nanomechanical resonator is represented using the van Dyke–Butterworth model[282] by a static capacitor C_g in parallel with an RLC circuit with equivalent elements C_m, R_m and L_m. (b) Schematic of the measurement of the motion of a carbon nanotube mechanical resonator with the two source method. In this example[283] the LC resonator comprises an inductor $L_C = 66$ μH in parallel with the capacitance of the line $C_{line} = 242$ pF to transmit the current noise I_d generated motion of the mechanical resonator. (c) Schematic of the measurement of the motion of a carbon nanotube mechanical resonator[284] using a tuneable capacitance $C_t = 3.82$ pF and an inductor $L_C = 223$ nH to bring the LC resonator in resonance with the mechanical motion to capture the current noise I_d generated directly at the mechanical resonance frequency.

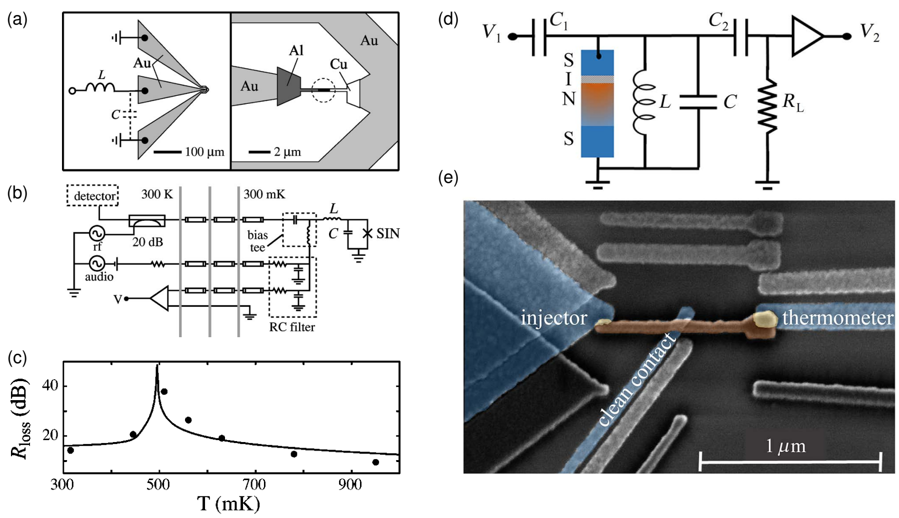

FIG. 44. Fast and nanoscale thermometry and calorimetry. (a) To demonstrate nanoscale radio-frequency thermometry, an LC resonator is loaded by a temperature-sensitive Al-oxide-Cu SIN junction (dashed circle). (b) Bias tees allow the application of ac bias voltages, to keep the junction at a temperature-dependent operating point on its IV characteristics, while the remaining reflectometry setup in this work was kept at room temperature. (c) The temperature dependence of the junction's operating point yields the matching condition for the LC tank circuit, evident here by a peak in the reflectometry return loss at 510 mK. Near matching, the demodulated reflectometry signal is sensitive to temperature changes. (d) SINS junction, in which the proximitized normal metal electrode gives rise to a zero-bias conductance anomaly that makes this thermometer useful for ultrasensitive calorimetry[298]. Importantly, this junction can be read out with reflectometry without the need to apply large (and invasive) bias voltages. (e) Implementation of the proximitized normal electrode by establishing a clean contact between the copper electrode (orange) and an aluminum electrode (blue). The overlapping region (yellow) with another aluminum electrode (thermometer) constitutes the SIN junction. The tunnel junction on the left (injector) was used to inject heat on the copper island, thereby manipulating its temperature in a well controlled manner. Panels (a),(b),(c) reproduced from[299], with the permission of AIP Publishing. Panels (d),(e) Reproduced with permission from Phys. Rev. Applied 10, 054048 (2018). Copyright 2018 American Physical Society.

thermal conductance associated with normal metals with low thermal conductance associated with superconductors) as well as technological applications (such as SINIS on-chip coolers[302]).

Figure 44(a) shows a nanoscale SIN junction (implemented by the aluminum - aluminum oxide - copper junction in the dashed circle, which was created by a multi-angle shadow evaporation technique) that is wirebonded to an inductor $L_C =$ 390 nH[299]. In conjunction with the stray capacitance $C_P =$ 0.6 pF of the bond wire, it forms a 338 MHz resonator that goes through matching as the SIN junction is cooled and temporarily reaches the matching resistance of 20 kΩ. As a consequence, the return loss (measured by reflectometry, and plotted in Fig. 44(c) shows a pronounced peak near 500 mK. The effective temperature (bandwidth) of this high-bandwidth "reflectometry thermometer" was 0.3 mK/Hz$^{1/2}$ (10 MHz), but adjustments to the choice of circuit parameters and improvements to device and reflectometry setup allow application to other temperature ranges and to thermodynamic and calorimetric studies of mesoscopic nanostructures and far-infrared detectors. To put these numbers into the context of calorimetry, Ref. 298 notes that a temperature noise of 10 μK/Hz$^{1/2}$ would be desired to detect the heat quantum associated with, say, a 1-K microwave photon. An improved modification is shown in Fig. 44(d), where the normal metal contact has been replaced by a proximitized normal metal[298]. In contrast to the SIN junction, this results in a zero-bias conductance feature in the IV characteristics of the junction, thereby obliterating the need for large biasing voltages (which constitute a source of heating). Accordingly, this thermometer was demonstrated to function at temperatures as low as 25 mK, with a sensitivity and noise performance almost sufficient to detect heat quanta relevant for superconducting qubit circuits (1-K photon conversions).

For semiconducting quantum devices, primary thermometry (measured via reflectometry) is possible by employing that the cyclic electron tunneling between a discrete state in a QD and an electron reservoir depends on the thermal distribution function of the reservoir. By embedding the plunger gate electrode of a quantum dot in an rf resonator, the reflectometry carrier induces cyclic tunneling and dispersively senses the tunnelling response[123]. Interestingly, in certain regimes, the width of the tunneling capacitance along the detuning of the dot (with respect to the Fermi level of the reservoir) depends only on temperature, thereby making this a primary thermometer for the electron reservoir (if the detuning lever arm is known). This lever arm is usually measured using a source-drain bias across the thermometer device, but it can also be calibrated by measuring the width of the tunneling peak at known temperature. This allows the temperature to be measured, even when the circuit is galvanically isolated[303]. Alternatively, the thermal distribution of the reservoir can be deduced by conductance measurement of the quantum dot from which the temperature is deduced. This process can be considerably accelerated using rf-readout of the QD resistance[304].

F. Sensing the semiconductor environment

In semiconducting devices with reduced dimensionality for the effective carriers, physical intuition from bulk systems has been shown again and again to break down with the emergence of quantum phenomena. For the kinetic energies, a drastic modification of the density of states by spatial quantization appears already in the simplest, non-interacting treatment of single-particle states (such as van Hove singularities in quasi 1D systems). For the electrostatic potentials, distinctly different length scales associated with electrostatic screening appear. For example, in 1D systems, the familiar exponential decay of potentials in 2D interfaces, or depletion lengths, are replaced by very long-range (logarithmic) tails in the charge distribution that affect the physics and engineering of p-n junctions, n-i junctions, and metal-semiconductor heterojunctions (Schottky barriers)[305,306]. Moreover, the categorical classification of any 3D fundamental particle as either a boson or a fermion (originating from the strictly integer and half-integer eigenvalues associated with rotational symmetry in 3-dimensional space) no longer holds for emergent quasiparticles in 2D and 1D systems. Here, the reduced spatial symmetries allow other exchange statistics, including abelian and non-abelian exchange statistics associated with *anyons* that are neither bosons nor fermions. For instance, in 2D systems, capacitance measurements play an important role for establishing localization of normally or fractionally charged quasiparticles in GaAs quantum Hall systems[307–309], and electron-hole puddles[310] and correlated instulators[311] in graphene structures.

In 1D systems, electron interaction gives rise to such exotic phenomena as spin–charge separation and the emergence of correlated-electron insulators and Wigner crystals (facilitated by the ineffective screening of the long range Coulomb interaction in 1D), which have been traditionally been measured by transport[312–315] but are also conducive to charge sensing[316].

Not surprisingly, reflectometry of semiconductors using dispersive gate sensing reveals information complementary to traditional transport measurements. For example, conductance measurements of quantum point contacts[27,317] often show a mysterious anomaly at $0.7 \times 2e^2/h$ that is now thought to comprise interaction and scattering effects in the presence of a smeared van Hove singularity in the local density of states at the bottom of the lowest one-dimensional subband[318] or perhaps Kondo correlations[319].

When applying dispersive gate sensing to similar quantum point devices, a surprising richness of features appeared in gate voltage space that persists even below the threshold for non-zero conductance[320]. In Fig. 45(c), we show a clever use of frequency multiplexing that allows reflectometry of various gate electrodes (and contact leads) of a top-gated GaAs heterostructure. This way, the reflectometry features of various gate electrodes could be compared for the same chip (an example for the reflectometry signal from gate G5 is shown in panel (c). The appearance of many (quasiperiodic) oscillations with varying slope in gate-voltage space were attributed not to physics associated with the region of the quantum point contacts (which dominates the signal in transport

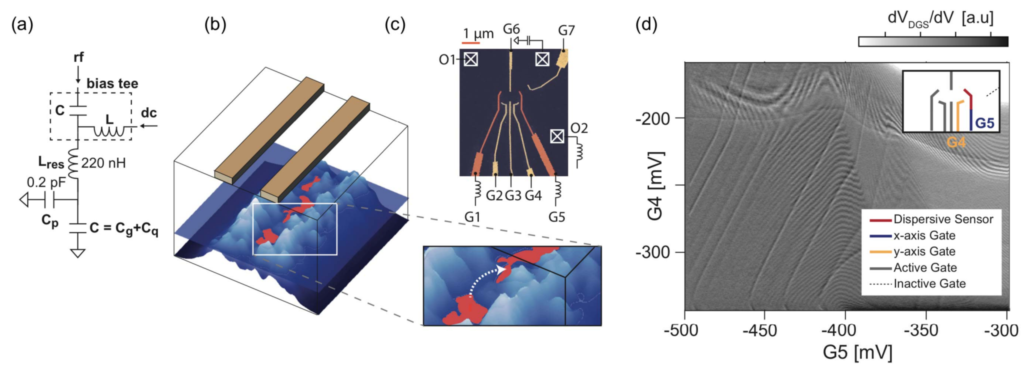

FIG. 45. Gate-sensing of charge pockets in the semiconductor environment of GaAs QPC devices. (a) Schematic of the reflectometry circuit, indicating the the rf response is sensitive to geometrical capacitances (C_g, set by the geometry of gate electrodes) and quantum capacitances (C_q, sensitive to the density of states in the semiconductor). (b) Visualization of electrostatic disorder potentials (blue) affecting the localization of the 2DEG in charge pockets (red areas). (c) Charge-pocket phenomena occuring near different gate electrodes (and not necessarily contributing to traditional conductance measurements of the different QPCs of this device) can be detected by performing frequency-multiplexed reflectometry of different gate electrodes, for example G1 and G5. (d) Example of the G5 reflectometry signal as a function of gate voltages applied to G5 and G4. To increase the visibility of quasi-periodic Coulomb oscillations with varying slopes and periods, associated with different charge puddles, the derivative of the demodulated voltage (wrt gate-voltage G4) is plotted. The precise pattern of Coulomb-blockade oscillations was sensitive to the exact voltages applied to neighboring gate electrodes (not shown). Reproduced with permission from Phys. Rev. Applied 11, 064027 (2019). Copyright 2019 American Physical Society.

measurements), but to regions near the extended gate electrodes that, in the presence of spatial disorder in the potential landscape, form charge puddles. Follow-up work suggests that reflectometry features in the pinched-off regime (i.e. zero QPC conductance) may also have contributions from asymmetric capacitive couplings between the reflectometry gate and the source and drain reservoirs, whereas the non-zero conductance staircase associated with QPC behaviour can in fact show up clearly in reflectometry[100].

G. SQUID magnetometer

Superconducting quantum interference devices (SQUIDs) are used as extremely sensitive magnetometers, among other applications, in quantum sensing and quantum technologies. For example, SQUIDs are employed to measure cosmic radiation[321] or as particle detectors[322].

SQUIDs falls into two categories[323]: the dc SQUID and the rf SQUID. dc SQUIDs are made of two junctions in parallel in a superconducting loop. When the dc SQUID pick-up a small magnetic flux it generates a screening current along the loop that maintains the total flux to a multiple of the flux quantum $\Phi_0 = h/2e$. As we have already seen, dc SQUIDs can be employed as ultra-low noise amplifiers.

We are interested here in the second type: the radio-frequency SQUID (rf SQUID). These are made of only one Josephson junction in a superconducting loop that is inductively coupled to a LC resonator formed by an inductance and a capacitance in parallel (Fig. 46). Because they are made

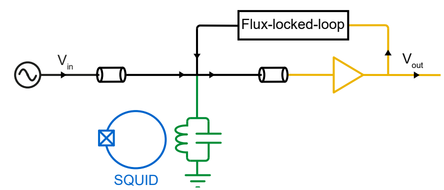

FIG. 46. rf SQUID setup inspired by Ref. 323. The rf SQUID, formed by a superconducting loop with one single Josephson junction, is inductively coupled to an LC resonator represented by a capacitance and an inductor. The readout in this setup is a transmission-type measurement, with an input signal V_{in} sent to the LC resonator and the rf SQUID, and with an amplified transmitted signal V_{out}. A flux-locked-loop stabilises the rf SQUID to maintain an optimised sensitivity.

of only one Josephson junction, rf SQUIDs are easier to fabricate. But their sensitivity is limited by the readout setup which is a motivation for further optimisation[323].

The readout of an rf SQUID is a transmission-type measurement with the LC resonator inductively coupled to the SQUID (Fig. 46). A radio-frequency signal V_{in} is sent to the LC resonator and the SQUID while the transmitted signal is amplified to become the output signal V_{out}. The magnetic flux picked up by the SQUID changes the phase across the Josephson junction, which then modifies the impedance of the SQUID and the resonator. This translates into the transmitted signal phase and amplitude. The rf SQUID measurement setup generally integrates a flux-locked-loop feedback system to maintain the SQUID at its sweet spot where its sensitivity is best. This is especially important when the bandwidth of the LC resonator is low.

We distinguish two types of rf SQUID, based on device parameters which influence the readout method, depending on $\beta_{\mathrm{rf}} = 2\pi L I_0/\Phi_0$[323] where L is the loop inductance and I_0 is the critical current of the Josephson junction. If $\beta_{\mathrm{rf}} > 1$ the SQUID is hysteretic and the transmission measurement is dissipative. The radio-frequency signal causes the Josephson junctions to switch periodically between two quantum states causing dissipation of the signal. This dissipation reduces the quality factor of the *LC* resonator and affects the amplitude of the transmitted signal, similar to a resistance measurement. This switch causes intrinsic noise that limits the sensitivity of a hysteretic rf SQUID.

If $\beta_{\mathrm{rf}} < 1$, the SQUID is non-hysteretic and the measurement is dispersive. The inductor of the tank circuit is parametrically coupled to the SQUID. The magnetic flux in the SQUID loop modifies the total inductance of the circuit, which changes its resonance frequency. This regime gives less intrinsic noise than the hysteretic SQUID.

X. CONCLUSION AND OUTLOOK

After two decades of developments, the high-speed electrical readout of quantum devices is allowing us to advance quantum computing and several other fields of research. In this Review, we focused on reflectometry circuits to perform high-speed sensitive measurements of quantum devices. In the development of radio-frequency readout techniques, circuit quantum electrodynamics and its application to the readout of superconducting qubits has been a source of inspiration[324].

One of the main driving forces for the advancement of radio-frequency technologies has been the rise of charge and spin qubits. The need for fast, sensitive and scalable readout of charge and spin states has promoted the development of single-shot readout techniques, the integration of superconducting components and the search for circuit multiplexing approaches described in this review. Careful engineering of the rf circuits made the difference. The optimisation of matching circuits, amplifier chains and PCB designs and materials are a few of the strategies discussed.

Fast measurements are not only directed at the readout of charge and spin states, but also to the tuning and characterisation of quantum devices[79,196,325]. Video-mode measurements demonstrate the potential of rf circuits for tuning quantum dot devices. The limiting factor is no longer the speed of the measurements but the ability of humans to analyse and interpret the data. The integration of machine learning techniques is allowing us to tackle such limitations[326–328].

Rf readout has also allowed for sensitive measurements of temperature and motion at the nanoscale, with applications such as the thermalisation of quantum circuits and other aspects of non-equilibrium and quantum thermodynamics. The gate capacitance of a nanowire transistor was measured, with high precision, using an LC resonator[329]. It is also used to sense the semiconductor environment of quantum devices, investigate Majoranas and dark matter, and probe other phenomena in the solid state. We expect rf-based techniques to enable yet new types of experiments. The use of pulsed magnetic fields[330,331] is an example of a technique that asks for the fast readout capabilities that rf reflectometry can offer. Rf readout could also be a key tool for the exploration of different mechanisms of electron transfer. Kondo physics, commonly probed by transport measurements, was found to be 'transparent' in a cavity quantum electrodynamic architecture[332]. In the same way, rf techniques can be used to explore many-body correlations.

We hope this review is a guide for students and researchers to explore the full potential of rf readout. Our optimisation guidelines, focused not only on rf components but also on the specifics of high-frequency lines, noise floors and amplifier chains, provide a starting point to advance rf reflectometry and to use it to further a broad variety of research fields.

ACKNOWLEDGMENTS

DJR acknowledges Microsoft Corporation and the ARC Centre of Excellence for Engineered Quantum Systems. FK acknowledges the Danish National Research Foundation, Independent Research Fund Denmark, Novo Nordisk Foundation grant No. NNF20OC0060019, and the European Commission (grant agreements 951852 and 856526). MFGZ acknowledges support from Quantum Motion Technologies, the European Commission (grant agreement 951852), the Innovate UK Industry Strategy Challenge Fund, and the UKRI via a Future Leaders Fellowship (grant number MR/V023284/1). EAL acknowledges the ERC (grant agreement 818751), the EU H2020 European Microkelvin Platform (grant agreement 824109), the Joy Welch Educational Charitable Trust. We thank the UK Science and Technology Facilities Council (STFC) for funding this work through support for the Quantum Sensors for the Hidden Sector (QSHS) collaboration under grants ST/T006102/1, ST/T006242/1, ST/T006145/1, ST/T006277/1, ST/T006625/1, ST/T006811/1, ST/T006102/1 and ST/T006099/1. NA acknowledges the Royal Society (URF R1 191150), an EPSRC Platform Grant (EP/R029229/1), grant number FQXi-IAF19-01 from the Foundational Questions Institute Fund, a donor advised fund of Silicon Valley Community Foundation, and the ERC (grant agreement 948932).

Competing Interests

The authors have no conflict of interest to declare.

Correspondence

Correspondence and requests for materials should be addressed to Edward A. Laird at e.a.laird@lancaster.ac.uk, M.

Fernando Gonzalez-Zalba at fernando@quantummotion.tech, and/or Natalia Ares at natalia.ares@eng.ox.ac.uk.

[1] P. Lafarge, H. Pothier, E. R. Williams, D. Esteve, C. Urbina, and M. H. Devoret, "Direct observation of macroscopic charge quantization," Zeitschrift für Physik B Condensed Matter **85**, 327–332 (1991).
[2] T. A. Fulton and G. J. Dolan, "Observation of single-electron charging effects in small tunnel junctions," Physical review letters **59**, 109 (1987).
[3] E. Visscher, J. Lindeman, S. Verbrugh, P. Hadley, J. Mooij, and W. Van Der Vleuten, "Broadband single-electron tunneling transistor," Applied Physics Letters **68**, 2014–2016 (1996).
[4] J. Pettersson, P. Wahlgren, P. Delsing, D. Haviland, T. Claeson, N. Rorsman, and H. Zirath, "Extending the high-frequency limit of a single-electron transistor by on-chip impedance transformation," Physical Review B **53**, R13272 (1996).
[5] B. Starmark, P. Delsing, D. Haviland, and T. Claeson, "Noise measurements of single electron transistors using a transimpedance amplifier," Applied superconductivity **6**, 837–841 (1999).
[6] R. Schoelkopf, P. Wahlgren, A. Kozhevnikov, P. Delsing, and D. Prober, "The radio-frequency single-electron transistor (RF-SET): A fast and ultrasensitive electrometer," Science **280**, 1238 (1998).
[7] D. J. Ibberson, L. A. Ibberson, G. Smithson, J. A. Haigh, S. Barraud, and M. F. Gonzalez-Zalba, "Low-temperature tunable radio-frequency resonator for sensitive dispersive readout of nanoelectronic devices," Applied Physics Letters **114**, 123501 (2019).
[8] D. Loss and D. P. DiVincenzo, "Quantum computation with quantum dots," Physical Review A **57**, 120 (1998).
[9] A. G. Fowler, M. Mariantoni, J. M. Martinis, and A. N. Cleland, "Surface codes: Towards practical large-scale quantum computation," Phys. Rev. A **86**, 032324 (2012).
[10] A. Blais, A. L. Grimsmo, S. M. Girvin, and A. Wallraff, "Circuit quantum electrodynamics," Rev. Mod. Phys. **93**, 025005 (2021).
[11] D. M. Pozar, *Microwave Engineering* (John Wiley and Sons, 2012).
[12] (), its doom may not be final. By inserting Josephson junctions into a coplanar stripline to increase its inductance[179,333], the characteristic impedance can be increased to $Z_0 \approx 1$ kΩ. Transmission lines exploiting the quantum Hall effect have been proposed as a way to make Z_0 even larger[334].
[13] (), one way to see this is to imagine that while the resonator is illuminated at frequency $f_{\rm in}$, one of its parameters is modulated at frequency $f_{\rm m}$. The current through the resonator, which without modulation would vary at the illumination frequency, is modulated by the changing impedance and therefore acquires sidebands at frequency $f_{\rm in} \pm f_{\rm m}$ (and possibly also at higher multiples of $f_{\rm m}$). The reflected signal V_- arises from the radiation of these sidebands into the transmission line. However, if the sidebands fall outside the resonance frequency window, i.e. $f_{\rm m} \gtrsim B_f/2$, they couple only weakly to the transmission line and the reflected signal is not modulated. A way to circumvent this problem, if you want to measure a modulation whose frequency is known but greater than the resonator bandwith, is to illuminate at $f_{\rm in} + f_{\rm m}$ so that the sideband appears inside the window[335].
[14] (), since the power is proportional to $|\Gamma|^2$, the half power bandwidth can be found at $1/\sqrt{2}$ of the maximum Γ or magnitude when plotted in linear units[11].
[15] K. Lehnert, K. Bladh, L. Spietz, D. Gunnarsson, D. Schuster, P. Delsing, and R. Schoelkopf, "Measurement of the excited-state lifetime of a microelectronic circuit," Physical review letters **90**, 027002 (2003).
[16] J. Elzerman, R. Hanson, J. Greidanus, L. W. Van Beveren, S. De Franceschi, L. Vandersypen, S. Tarucha, and L. Kouwenhoven, "Few-electron quantum dot circuit with integrated charge read out," Physical Review B **67**, 161308 (2003).
[17] L. DiCarlo, H. Lynch, A. Johnson, L. Childress, K. Crockett, C. Marcus, M. Hanson, and A. Gossard, "Differential charge sensing and charge delocalization in a tunable double quantum dot," Physical review letters **92**, 226801 (2004).
[18] L. Vandersypen, J. Elzerman, R. Schouten, L. Willems van Beveren, R. Hanson, and L. Kouwenhoven, "Real-time detection of single-electron tunneling using a quantum point contact," Applied Physics Letters **85**, 4394–4396 (2004).
[19] S. Gustavsson, R. Leturcq, B. Simovič, R. Schleser, T. Ihn, P. Studerus, K. Ensslin, D. Driscoll, and A. Gossard, "Counting statistics of single electron transport in a quantum dot," Physical review letters **96**, 076605 (2006).
[20] T. Wagner, P. Talkner, J. C. Bayer, E. P. Rugeramigabo, P. Hänggi, and R. J. Haug, "Quantum stochastic resonance in an ac-driven single-electron quantum dot," Nature Physics **15**, 330–334 (2019).
[21] J. M. Elzerman, R. Hanson, L. H. Willems Van Beveren, B. Witkamp, L. M. K. Vandersypen, and L. P. Kouwenhoven, "Single-shot read-out of an individual electron spin in a quantum dot." Nature **430**, 431–5 (2004).
[22] A. Johnson, J. Petta, J. Taylor, A. Yacoby, M. Lukin, C. Marcus, M. Hanson, and A. Gossard, "Triplet–singlet spin relaxation via nuclei in a double quantum dot," Nature **435**, 925–928 (2005).
[23] J. R. Petta, A. C. Johnson, J. M. Taylor, E. A. Laird, A. Yacoby, M. D. Lukin, C. M. Marcus, M. P. Hanson, and A. C. Gossard, "Coherent manipulation of coupled electron spins in semiconductor quantum dots," Science **309**, 2180–2184 (2005).
[24] S. Amasha, K. MacLean, I. P. Radu, D. M. Zumbühl, M. A. Kastner, M. P. Hanson, and A. C. Gossard, "Electrical control of spin relaxation in a quantum dot," Physical Review Letters **100**, 046803 (2008).
[25] E. A. Laird, J. M. Taylor, D. P. DiVincenzo, C. M. Marcus, M. P. Hanson, and A. C. Gossard, "Coherent spin manipulation in an exchange-only qubit," Physical Review B **82**, 075403 (2010).
[26] S. Datta, *Electronic transport in mesoscopic systems* (Cambridge university press, 1997).
[27] B. Van Wees, H. Van Houten, C. Beenakker, J. G. Williamson, L. Kouwenhoven, D. Van der Marel, and C. Foxon, "Quantized conductance of point contacts in a two-dimensional electron gas," Physical Review Letters **60**, 848 (1988).
[28] M. Field, C. Smith, M. Pepper, D. Ritchie, J. Frost, G. Jones, and D. Hasko, "Measurements of coulomb blockade with a noninvasive voltage probe," Physical Review Letters **70**, 1311 (1993).
[29] M. Cassidy, A. Dzurak, R. Clark, K. Petersson, I. Farrer, D. Ritchie, and C. Smith, "Single shot charge detection using a radio-frequency quantum point contact," Applied Physics Letters **91**, 222104 (2007).
[30] A. Aassime, G. Johansson, G. Wendin, R. Schoelkopf, and P. Delsing, "Radio-frequency single-electron transistor as readout device for qubits: Charge sensitivity and backaction," Physical Review Letters **86**, 3376 (2001).
[31] M. Veldhorst, C. Yang, J. Hwang, W. Huang, J. Dehollain, J. Muhonen, S. Simmons, A. Laucht, F. Hudson, K. M. Itoh, M. Andrea, and D. A., "A two-qubit logic gate in silicon," Nature **526**, 410–414 (2015).
[32] M. House, T. Kobayashi, B. Weber, S. Hile, T. Watson, J. Van Der Heijden, S. Rogge, and M. Simmons, "Radio frequency measurements of tunnel couplings and singlet–triplet spin states in Si:P quantum dots," Nature communications **6**, 1–6 (2015).
[33] M. A. Kastner, "The single-electron transistor," Rev. Mod. Phys. **64**, 849–858 (1992).
[34] R. Hanson, L. P. Kouwenhoven, J. R. Petta, S. Tarucha, and L. M. Vandersypen, "Spins in few-electron quantum dots," Reviews of Modern Physics **79**, 1217 (2007).
[35] C. W. Beenakker, "Theory of coulomb-blockade oscillations in the conductance of a quantum dot," Physical Review B **44**, 1646 (1991).
[36] Y. Hu, H. O. Churchill, D. J. Reilly, J. Xiang, C. M. Lieber, and C. M. Marcus, "A Ge/Si heterostructure nanowire-based double quantum dot with integrated charge sensor," Nature nanotechnology **2**, 622–625 (2007).
[37] H. O. H. Churchill, A. J. Bestwick, J. W. Harlow, F. Kuemmeth, D. Marcos, C. H. Stwertka, S. K. Watson, and C. M. Marcus, "Electron–nuclear interaction in ^{13}**C** nanotube double quantum dots," Nature Physics **5**, 321–326 (2009).
[38] H. O. H. Churchill, F. Kuemmeth, J. W. Harlow, A. J. Bestwick, E. I. Rashba, K. Flensberg, C. H. Stwertka, T. Taychatanapat, S. K. Watson, and C. M. Marcus, "Relaxation and dephasing in a two-electron ^{13}**C** nanotube double quantum dot," Phys. Rev. Lett. **102**, 166802 (2009).
[39] Y. Hu, F. Kuemmeth, C. M. Lieber, and C. M. Marcus, "Hole spin relaxation in Ge–Si core–shell nanowire qubits," Nature nanotechnology **7**, 47 (2012).
[40] A. P. Higginbotham, F. Kuemmeth, M. P. Hanson, A. C. Gossard, and C. M. Marcus, "Coherent operations and screening in multielectron spin qubits," Physical review letters **112**, 026801 (2014).
[41] A. Kurzmann, H. Overweg, M. Eich, A. Pally, P. Rickhaus, R. Pisoni, Y. Lee, K. Watanabe, T. Taniguchi, T. Ihn, and K. Ensslin, "Charge de-

tection in gate-defined bilayer graphene quantum dots," Nano letters **19**, 5216–5221 (2019).

[42] M. H. Devoret and R. J. Schoelkopf, "Amplifying quantum signals with the single-electron transistor," Nature **406**, 1039–1046 (2000).

[43] C. Barthel, M. Kjærgaard, J. Medford, M. Stopa, C. M. Marcus, M. Hanson, and A. C. Gossard, "Fast sensing of double-dot charge arrangement and spin state with a radio-frequency sensor quantum dot," Physical Review B **81**, 161308 (2010).

[44] S. J. Angus, A. J. Ferguson, A. S. Dzurak, and R. G. Clark, "Gate-defined quantum dots in intrinsic silicon," Nano Letters **7**, 2051–2055 (2007), angus, Susan J. Ferguson, Andrew J. Dzurak, Andrew S. Clark, Robert G.

[45] M. F. Gonzalez-Zalba, D. Heiss, G. Podd, and A. J. Ferguson, "Tunable aluminium-gated single electron transistor on a doped silicon-on-insulator etched nanowire," Applied Physics Letters **101**, 103504–103504–4 (2012).

[46] T. Nakajima, Y. Kojima, Y. Uehara, A. Noiri, K. Takeda, T. Kobayashi, and S. Tarucha, "Real-time feedback control of charge sensing for quantum dot qubits," Physical Review Applied **15**, L031003 (2021).

[47] (), all spectral densities in this Review are one-sided. Most experimentalists follow this convention, but a two-sided convention is widespread in theory-land[185]. To make a double-sided spectral density single-sided, multiply it by two; more details are given in the Supplementary Information.

[48] B. Starmark, T. Henning, T. Claeson, P. Delsing, and A. Korotkov, "Gain dependence of the noise in the single electron transistor," Journal of applied physics **86**, 2132–2136 (1999).

[49] D. J. Mar, R. M. Westervelt, and P. F. Hopkins, "Cryogenic field-effect transistor with single electronic charge sensitivity," Applied Physics Letters **64**, 631–633 (1994).

[50] Y. M. Blanter and M. Büttiker, "Shot noise in mesoscopic conductors," Physics reports **336**, 1–166 (2000).

[51] (), expressions for the Fano factor in different kinds of device are given in Ref. 50. The most important is

$$F = \frac{\sum_n T_n(1-T_n)}{\sum_n T_n}, \tag{165}$$

which applies when non-interacting electrons tunnel through a barrier, each of whose conductance channels has an energy-independent transmission T_n.

[52] A. N. Korotkov and M. A. Paalanen, "Charge sensitivity of radio frequency single-electron transistor," Applied physics letters **74**, 4052–4054 (1999).

[53] A. B. Zorin, "Quantum-limited electrometer based on single cooper pair tunneling," Phys. Rev. Lett. **76**, 4408–4411 (1996).

[54] M. J. Curry, M. Rudolph, T. D. England, A. M. Mounce, R. M. Jock, C. Bureau-Oxton, P. Harvey-Collard, P. A. Sharma, J. M. Anderson, D. M. Campbell, J. R. Wendt, D. R. Ward, S. M. Carr, M. P. Lilly, and M. S. Carroll, "Single-shot readout performance of two heterojunction-bipolar-transistor amplification circuits at millikelvin temperatures," Scientific Reports **9**, 16976 (2019).

[55] H. Qin and D. A. Williams, "Radio-frequency point-contact electrometer," Applied physics letters **88**, 203506 (2006).

[56] D. Reilly, C. Marcus, M. Hanson, and A. Gossard, "Fast single-charge sensing with a rf quantum point contact," Applied Physics Letters **91**, 162101 (2007).

[57] T. Müller, K. Vollenweider, T. Ihn, R. Schleser, M. Sigrist, K. Ensslin, M. Reinwald, and W. Wegscheider, "A radio frequency quantum point contact charge read-out," in *AIP Conference Proceedings*, Vol. 893 (American Institute of Physics, 2007) pp. 1113–1114.

[58] J. Mason, B. Djurkovic, J. Kycia, L. Gaudreau, S. Studenikin, A. Kam, and A. Sachrajda, "A high speed radio-frequency quantum point contact charge detector for time resolved readout applications of spin qubits," Physica E: Low-dimensional Systems and Nanostructures **42**, 813–816 (2010).

[59] T. Müller, B. Küng, S. Hellmüller, P. Studerus, K. Ensslin, T. Ihn, M. Reinwald, and W. Wegscheider, "An in situ tunable radio-frequency quantum point contact," Applied Physics Letters **97**, 202104 (2010).

[60] T. Müller, J. Güttinger, D. Bischoff, S. Hellmüller, K. Ensslin, and T. Ihn, "Fast detection of single-charge tunneling to a graphene quantum dot in a multi-level regime," Applied Physics Letters **101**, 012104 (2012).

[61] T. Müller, T. Choi, S. Hellmüller, K. Ensslin, T. Ihn, and S. Schön, "A circuit analysis of an in situ tunable radio-frequency quantum point contact," Review of Scientific Instruments **84**, 083902 (2013).

[62] T. Fujisawa and Y. Hirayama, "Charge noise analysis of an AlGaAs/GaAs quantum dot using transmission-type radio-frequency single-electron transistor technique," Applied Physics Letters **77**, 543–545 (2000).

[63] H. Brenning, S. Kafanov, T. Duty, S. Kubatkin, and P. Delsing, "An ultrasensitive radio-frequency single-electron transistor working up to 4.2 k," Journal of Applied Physics **100**, 114321 (2006).

[64] S. Angus, A. Ferguson, A. Dzurak, and R. Clark, "A silicon radio-frequency single electron transistor," Applied Physics Letters **92**, 112103 (2008).

[65] T. Otsuka, S. Amaha, T. Nakajima, M. R. Delbecq, J. Yoneda, K. Takeda, R. Sugawara, G. Allison, A. Ludwig, A. D. Wieck, and S. Tarcha, "Fast probe of local electronic states in nanostructures utilizing a single-lead quantum dot," Scientific reports **5**, 14616 (2015).

[66] M. House, I. Bartlett, P. Pakkiam, M. Koch, E. Peretz, J. Van Der Heijden, T. Kobayashi, S. Rogge, and M. Simmons, "High-sensitivity charge detection with a single-lead quantum dot for scalable quantum computation," Physical Review Applied **6**, 044016 (2016).

[67] (), in this example, the matching condition occurs when the QPC is pinched off ($G_{\mathrm{QPC}} = 0$) due to the relatively high dielectric losses (low R_{C}). As we shall see in Section V, when trying to maximise sensitivity to changes in device resistance, low R_{C} is detrimental and matching should preferentially be achieved in the bias condition under which the device is mostly used.

[68] F. Fedele, A. Chatterjee, S. Fallahi, G. C. Gardner, M. J. Manfra, and F. Kuemmeth, "Simultaneous operations in a two-dimensional array of singlet-triplet qubits," PRX Quantum **2**, 040306 (2021).

[69] A. C. Johnson, J. Petta, C. Marcus, M. Hanson, and A. Gossard, "Singlet-triplet spin blockade and charge sensing in a few-electron double quantum dot," Physical Review B **72**, 165308 (2005).

[70] W. Lu, Z. Ji, L. Pfeiffer, K. West, and A. Rimberg, "Real-time detection of electron tunnelling in a quantum dot," Nature **423**, 422–425 (2003).

[71] J. D. Mason, L. Gaudreau, S. A. Studenikin, A. Kam, B. Djurkovic, A. S. Sachrajda, and J. B. Kycia, "A high speed radio-frequency quantum point contact charge detector for time resolved readout applications of spin qubits," Physica E: Low-dimensional Systems and Nanostructures **42**, 813 – 816 (2010), 18th International Conference on Electron Properties of Two-Dimensional Systems.

[72] C. Barthel, D. Reilly, C. M. Marcus, M. Hanson, and A. Gossard, "Rapid single-shot measurement of a singlet-triplet qubit," Physical Review Letters **103**, 160503 (2009).

[73] K. Takeda, J. Kamioka, T. Otsuka, J. Yoneda, T. Nakajima, M. R. Delbecq, S. Amaha, G. Allison, T. Kodera, S. Oda, and S. Tarucha, "A fault-tolerant addressable spin qubit in a natural silicon quantum dot," Science advances **2**, e1600694 (2016).

[74] E. J. Connors, J. Nelson, and J. M. Nichol, "Rapid high-fidelity spin-state readout in Si/Si-Ge quantum dots via rf reflectometry," Phys. Rev. Applied **13**, 024019 (2020).

[75] T. Nakajima, A. Noiri, J. Yoneda, M. R. Delbecq, P. Stano, T. Otsuka, K. Takeda, S. Amaha, G. Allison, K. Kawasaki, A. Ludwig, D. A. Wieck, D. Loss, and S. Tarucha, "Quantum non-demolition measurement of an electron spin qubit," Nature nanotechnology **14**, 555–560 (2019).

[76] T. Nakajima, M. R. Delbecq, T. Otsuka, P. Stano, S. Amaha, J. Yoneda, A. Noiri, K. Kawasaki, K. Takeda, G. Allison, A. Ludwig, A. D. Wieck, D. Loss, and S. Tarucha, "Robust Single-Shot Spin Measurement with 99.5% Fidelity in a Quantum Dot Array," Physical Review Letters **119**, 017701 (2017).

[77] J. Yoneda, K. Takeda, T. Otsuka, T. Nakajima, M. R. Delbecq, G. Allison, T. Honda, T. Kodera, S. Oda, Y. Hoshi, N. Usami, M. K. Itoh, and S. Tarucha, "A quantum-dot spin qubit with coherence limited by charge noise and fidelity higher than 99.9%," Nature nanotechnology **13**, 102–106 (2018).

[78] M. Jung, M. Schroer, K. Petersson, and J. R. Petta, "Radio frequency charge sensing in inas nanowire double quantum dots," Applied Physics Letters **100**, 253508 (2012).

[79] J. Stehlik, Y.-Y. Liu, C. Quintana, C. Eichler, T. Hartke, and J. R. Petta, "Fast charge sensing of a cavity-coupled double quantum dot using a josephson parametric amplifier," Physical Review Applied **4**, 014018 (2015).

[80] D. Razmadze, D. Sabonis, F. K. Malinowski, G. C. Ménard, S. Pauka, H. Nguyen, D. M. van Zanten, E. C. O′Farrell, J. Suter, P. Krogstrup,

F. Kuemmeth, and C. M. Marcus, "Radio-frequency methods for majorana-based quantum devices: Fast charge sensing and phase-diagram mapping," Phys. Rev. Applied **11**, 064011 (2019).

[81]F. Persson, *Fast dynamics and measurements of single-charge devices* (Chalmers University of Technology, 2010).

[82]M. Gonzalez-Zalba, S. Barraud, A. Ferguson, and A. Betz, "Probing the limits of gate-based charge sensing," Nature communications **6**, 1–8 (2015).

[83]F. Persson, C. Wilson, M. Sandberg, G. Johansson, and P. Delsing, "Excess dissipation in a single-electron box: The sisyphus resistance," Nano letters **10**, 953–957 (2010).

[84]C. Ciccarelli and A. Ferguson, "Impedance of the single-electron transistor at radio-frequencies," New Journal of Physics **13**, 093015 (2011).

[85]K. Petersson, C. Smith, D. Anderson, P. Atkinson, G. Jones, and D. Ritchie, "Charge and spin state readout of a double quantum dot coupled to a resonator," Nano letters **10**, 2789–2793 (2010).

[86]C. Volk, A.-M. J. Zwerver, U. Mukhopadhyay, P. T. Eendebak, C. J. van Diepen, J. P. Dehollain, T. Hensgens, T. Fujita, C. Reichl, W. Wegscheider, and L. M. K. Vandersypen, "Loading a quantum-dot based "qubyte" register," npj Quantum Information **5**, 1–8 (2019).

[87]A. Mills, D. Zajac, M. Gullans, F. Schupp, T. Hazard, and J. Petta, "Shuttling a single charge across a one-dimensional array of silicon quantum dots," Nature communications **10**, 1–6 (2019).

[88]P.-A. Mortemousque, E. Chanrion, B. Jadot, H. Flentje, A. Ludwig, A. D. Wieck, M. Urdampilleta, C. Bäuerle, and T. Meunier, "Coherent control of individual electron spins in a two-dimensional quantum dot array," Nature Nanotechnology **16**, 296–301 (2021).

[89]J. Colless, A. Mahoney, J. Hornibrook, A. Doherty, H. Lu, A. Gossard, and D. Reilly, "Dispersive readout of a few-electron double quantum dot with fast rf gate sensors," Physical review letters **110**, 046805 (2013).

[90]S. Chorley, J. Wabnig, Z. Penfold-Fitch, K. Petersson, J. Frake, C. Smith, and M. Buitelaar, "Measuring the complex admittance of a carbon nanotube double quantum dot," Physical review letters **108**, 036802 (2012).

[91]S. Luryi, "Quantum capacitance devices," Applied Physics Letters **52**, 501–503 (1988), https://doi.org/10.1063/1.99649.

[92]M. Büttiker, H. Thomas, and A. Prêtre, "Mesoscopic capacitors," Physics Letters A **180**, 364–369 (1993).

[93]J. A. Sulpizio, *Quantum Transport in One-Dimensional Nanostructures* (Stanford University, 2011).

[94]J. P. Eisenstein, L. N. Pfeiffer, and K. W. West, "Compressibility of the two-dimensional electron gas: Measurements of the zero-field exchange energy and fractional quantum hall gap," Phys. Rev. B **50**, 1760–1778 (1994).

[95]J. Xia, F. Chen, J. Li, and N. Tao, "Measurement of the quantum capacitance of graphene," Nature nanotechnology **4**, 505–509 (2009).

[96]E. A. Henriksen and J. P. Eisenstein, "Measurement of the electronic compressibility of bilayer graphene," Phys. Rev. B **82**, 041412 (2010).

[97]S. Dröscher, P. Roulleau, F. Molitor, P. Studerus, C. Stampfer, K. Ensslin, and T. Ihn, "Quantum capacitance and density of states of graphene," Applied physics letters **96**, 152104 (2010).

[98]S. L. Tomarken, Y. Cao, A. Demir, K. Watanabe, T. Taniguchi, P. Jarillo-Herrero, and R. C. Ashoori, "Electronic compressibility of magic-angle graphene superlattices," Phys. Rev. Lett. **123**, 046601 (2019).

[99]S. Ilani, L. A. Donev, M. Kindermann, and P. L. McEuen, "Measurement of the quantum capacitance of interacting electrons in carbon nanotubes," Nature Physics **2**, 687–691 (2006).

[100]M. Jarratt, S. Waddy, A. Jouan, A. Mahoney, G. Gardner, S. Fallahi, M. Manfra, and D. Reilly, "Detection of the quantum capacitance of a point contact via dispersive gate sensing," Physical Review Applied **14**, 064021 (2020).

[101]T. Lundberg, J. Li, L. Hutin, B. Bertrand, D. J. Ibberson, C.-M. Lee, D. J. Niegemann, M. Urdampilleta, N. Stelmashenko, T. Meunier, J. W. A. Robinson, L. Ibberson, M. Vinet, Y.-M. Niquet, and M. F. Gonzalez-Zalba, "Spin quintet in a silicon double quantum dot: Spin blockade and relaxation," Phys. Rev. X **10**, 041010 (2020).

[102]J. Duan, J. S. Lehtinen, M. A. Fogarty, S. Schaal, M. M. L. Lam, A. Ronzani, A. Shchepetov, P. Koppinen, M. Prunnila, F. Gonzalez-Zalba, and J. J. L. Morton, "Dispersive readout of reconfigurable ambipolar quantum dots in a silicon-on-insulator nanowire," Applied Physics Letters **118**, 164002 (2021).

[103]M. Esterli, R. Otxoa, and M. Gonzalez-Zalba, "Small-signal equivalent circuit for double quantum dots at low-frequencies," Applied Physics Letters **114**, 253505 (2019).

[104]R. Mizuta, R. M. Otxoa, A. C. Betz, and M. F. Gonzalez-Zalba, "Quantum and tunneling capacitance in charge and spin qubits," Phys. Rev. B **95**, 045414 (2017).

[105]I. Ahmed and M. F. Gonzalez-Zalba, "Radio-frequency capacitive gate-based charge sensing for semiconductor quantum dots," in *Micro and Nano Machined Electrometers*, edited by Y. Zhu (Springer Singapore, Singapore, 2020) pp. 83–128.

[106]R. Ashoori, H. Stormer, J. Weiner, L. Pfeiffer, S. Pearton, K. Baldwin, and K. West, "Single-electron capacitance spectroscopy of discrete quantum levels," Physical review letters **68**, 3088 (1992).

[107]R. Ashoori, H. Stormer, J. Weiner, L. Pfeiffer, K. Baldwin, and K. West, "N-electron ground state energies of a quantum dot in magnetic field," Physical review letters **71**, 613 (1993).

[108]M. F. Gonzalez-Zalba, S. N. Shevchenko, S. Barraud, J. R. Johansson, A. J. Ferguson, F. Nori, and A. C. Betz, "Gate-sensing coherent charge oscillations in a silicon field-effect transistor," Nano letters **16**, 1614–1619 (2016).

[109]S. N. Shevchenko, S. Ashhab, and F. Nori, "Landau-zener-stückelberg interferometry," Physics Reports **492**, 1 – 30 (2010).

[110]R. M. Otxoa, A. Chatterjee, S. N. Shevchenko, S. Barraud, F. Nori, and M. F. Gonzalez-Zalba, "Quantum interference capacitor based on double-passage landau-zener-stückelberg-majorana interferometry," Phys. Rev. B **100**, 205425 (2019).

[111]M. Urdampilleta, A. Chatterjee, C. C. Lo, T. Kobayashi, J. Mansir, S. Barraud, A. C. Betz, S. Rogge, M. F. Gonzalez-Zalba, and J. J. Morton, "Charge dynamics and spin blockade in a hybrid double quantum dot in silicon," Physical Review X **5**, 031024 (2015).

[112]A. West, B. Hensen, A. Jouan, T. Tanttu, C. H. Yang, A. Rossi, M. F. Gonzalez-Zalba, F. E. Hudson, A. Morello, D. J. Reilly, and A. S. Dzurak, "Gate-based single-shot readout of spins in silicon," Nature Nanotechnology **14**, 437 (2019).

[113](), we note that in Eq. (88), the capacitances appear in parallel as opposed to the example of the mesoscopic capacitor where the capacitances appear in series (see Eq. (68)). This is a result of the different geometry of the two examples, where the DQD system contains additional capacitances to the charge reservoirs.

[114]K.-H. Ahn and P. Mohanty, "Quantum friction of micromechanical resonators at low temperatures," Physical review letters **90**, 085504 (2003).

[115]M. Grajcar, S. Van der Ploeg, A. Izmalkov, E. Il'ichev, H.-G. Meyer, A. Fedorov, A. Shnirman, and G. Schön, "Sisyphus cooling and amplification by a superconducting qubit," Nature physics **4**, 612–616 (2008).

[116]M. Sillanpää, T. Lehtinen, A. Paila, Y. Makhlin, and P. Hakonen, "Continuous-time monitoring of landau-zener interference in a cooper-pair box," Phys. Rev. Lett. **96**, 187002 (2006).

[117]F. Persson, C. M. Wilson, M. Sandberg, and P. Delsing, "Fast readout of a single cooper-pair box using its quantum capacitance," Phys. Rev. B **82**, 134533 (2010).

[118]E. Chanrion, D. J. Niegemann, B. Bertrand, C. Spence, B. Jadot, J. Li, P.-A. Mortemousque, L. Hutin, R. Maurand, X. Jehl, M. Sanquer, S. De Franceschi, C. Bäuerle, F. Balestro, Y.-M. Niquet, M. Vinet, T. Meunier, and M. Urdampilleta, "Charge detection in an array of CMOS quantum dots," Physical Review Applied **14**, 024066 (2020).

[119]F. Ansaloni, A. Chatterjee, H. Bohuslavskyi, B. Bertrand, L. Hutin, M. Vinet, and F. Kuemmeth, "Single-electron operations in a foundry-fabricated array of quantum dots," Nature communications **11**, 1–7 (2020).

[120]H. Bohuslavskyi, F. Ansaloni, A. Chatterjee, F. Fedele, T. Rasmussen, B. Brovang, J. Li, L. Hutin, B. Venitucci, B. Bertrand, M. Vinet, Y.-M. Niquet, and F. Kuemmeth, "Reflectometry of charge transitions in a silicon quadruple dot," arXiv preprint arXiv:2012.04791 (2020).

[121]J. Duan, M. A. Fogarty, J. Williams, L. Hutin, M. Vinet, and J. J. Morton, "Remote capacitive sensing in two-dimensional quantum-dot arrays," Nano Letters **20**, 7123–7128 (2020).

[122]V. N. Ciriano-Tejel, M. A. Fogarty, S. Schaal, L. Hutin, B. Bertrand, L. Ibberson, M. F. Gonzalez-Zalba, J. Li, Y.-M. Niquet, M. Vinet, and J. J. Morton, "Spin Readout of a CMOS Quantum Dot by Gate Reflectometry and Spin-Dependent Tunneling," PRX Quantum **2**, 010353 (2021).

[123] I. Ahmed, A. Chatterjee, S. Barraud, J. J. Morton, J. A. Haigh, and M. F. Gonzalez-Zalba, "Primary thermometry of a single reservoir using cyclic electron tunneling to a quantum dot," Communications Physics **1**, 1–7 (2018).

[124] L. Hutin, B. Bertrand, E. Chanrion, H. Bohuslavskyi, F. Ansaloni, T.-Y. Yang, J. Michniewicz, D. J. Niegemann, C. Spence, T. Lundberg, A. Chatterjee, A. Crippa, J. Li, R. Maurand, X. Jehl, M. Sanquer, M. F. Gonzalez-Zalba, F. Kuemmeth, Y.-M. Niquet, S. De Franceschi, M. Urdampilleta, T. Meunier, and M. Vinet, "Gate reflectometry for probing charge and spin states in linear Si MOS split-gate arrays," in *2019 IEEE International Electron Devices Meeting (IEDM)* (2019) pp. 37.7.1–37.7.4.

[125] R. Thalineau, S. Hermelin, A. D. Wieck, C. Bäuerle, L. Saminadayar, and T. Meunier, "A few-electron quadruple quantum dot in a closed loop," Applied Physics Letters **101**, 103102 (2012).

[126] H. Flentje, B. Bertrand, P.-A. Mortemousque, V. Thiney, A. Ludwig, A. D. Wieck, C. Bäuerle, and T. Meunier, "A linear triple quantum dot system in isolated configuration," Applied Physics Letters **110**, 233101 (2017).

[127] U. Mukhopadhyay, J. P. Dehollain, C. Reichl, W. Wegscheider, and L. M. Vandersypen, "A 2× 2 quantum dot array with controllable inter-dot tunnel couplings," Applied Physics Letters **112**, 183505 (2018).

[128] W. Gilbert, A. Saraiva, W. H. Lim, C. H. Yang, A. Laucht, B. Bertrand, N. Rambal, L. Hutin, C. C. Escott, M. Vinet, and A. S. Dzurak, "Single-Electron Operation of a Silicon-CMOS 2 x 2 Quantum Dot Array with Integrated Charge Sensing," Nano Letters **20**, 7882–7888 (2020), pMID: 33108202, https://doi.org/10.1021/acs.nanolett.0c02397.

[129] P.-A. Mortemousque, E. Chanrion, B. Jadot, H. Flentje, A. Ludwig, A. D. Wieck, M. Urdampilleta, C. Bäuerle, and T. Meunier, "Coherent control of individual electron spins in a two-dimensional quantum dot array," Nature Nanotechnology , 1–6 (2020).

[130] W. I. L. Lawrie, H. G. J. Eenink, N. W. Hendrickx, J. M. Boter, L. Petit, S. V. Amitonov, M. Lodari, B. Paquelet Wuetz, C. Volk, S. G. J. Philips, G. Droulers, N. Kalhor, F. van Riggelen, D. Brousse, A. Sammak, L. M. K. Vandersypen, G. Scappucci, and M. Veldhorst, "Quantum dot arrays in silicon and germanium," Applied Physics Letters **116**, 080501 (2020), https://doi.org/10.1063/5.0002013.

[131] F. Van Riggelen, N. Hendrickx, W. Lawrie, M. Russ, A. Sammak, G. Scappucci, and M. Veldhorst, "A two-dimensional array of single-hole quantum dots," Applied Physics Letters **118**, 044002 (2021).

[132] M. F. Gonzalez-Zalba, A. Saraiva, M. J. Calderon, D. Heiss, B. Koiller, and A. J. Ferguson, "An exchange-coupled donor molecule in silicon," Nano Letters **14**, 5672–5676 (2014).

[133] A. Crippa, R. Maurand, D. Kotekar-Patil, A. Corna, H. Bohuslavskyi, A. O. Orlov, P. Fay, R. Laviéville, S. Barraud, M. Vinet, M. Sanquer, S. De Franceschi, and X. Jehl, "Level spectrum and charge relaxation in a silicon double quantum dot probed by dual-gate reflectometry," Nano letters **17**, 1001–1006 (2017).

[134] I. Ahmed, J. A. Haigh, S. Schaal, S. Barraud, Y. Zhu, C.-m. Lee, M. Amado, J. W. A. Robinson, A. Rossi, J. J. L. Morton, and M. F. Gonzalez-Zalba, "Radio-frequency capacitive gate-based sensing," Phys. Rev. Applied **10**, 014018 (2018).

[135] P. Pakkiam, A. Timofeev, M. House, M. Hogg, T. Kobayashi, M. Koch, S. Rogge, and M. Y. Simmons, "Single-shot single-gate rf spin readout in silicon," Physical Review X **8**, 041032 (2018).

[136] G. Zheng, N. Samkharadze, M. L. Noordam, N. Kalhor, D. Brousse, A. Sammak, G. Scappucci, and L. M. Vandersypen, "Rapid gate-based spin read-out in silicon using an on-chip resonator," Nature nanotechnology **14**, 742–746 (2019).

[137] S. Schaal, I. Ahmed, J. A. Haigh, L. Hutin, B. Bertrand, S. Barraud, M. Vinet, C.-M. Lee, N. Stelmashenko, J. W. A. Robinson, J. Y. Qiu, S. Hacohen-Gourgy, I. Siddiqi, M. F. Gonzalez-Zalba, and J. J. L. Morton, "Fast gate-based readout of silicon quantum dots using josephson parametric amplification," Phys. Rev. Lett. **124**, 067701 (2020).

[138] D. J. Ibberson, T. Lundberg, J. A. Haigh, L. Hutin, B. Bertrand, S. Barraud, C.-M. Lee, N. A. Stelmashenko, G. A. Oakes, L. Cochrane, J. W. Robinson, M. Vinet, M. F. Gonzalez-Zalba, and L. A. Ibberson, "Large Dispersive Interaction between a CMOS Double Quantum Dot and Microwave Photons," PRX Quantum **2**, 020315 (2021).

[139] M. Urdampilleta, D. J. Niegemann, E. Chanrion, B. Jadot, C. Spence, P. A. Mortemousque, C. Bäuerle, L. Hutin, B. Bertrand, S. Barraud, R. Maurand, M. Sanquer, X. Jehl, S. De Franceschi, M. Vinet, and T. Meunier, "Gate-based high fidelity spin readout in a CMOS device," Nature Nanotechnology **14**, 737 (2019).

[140] G. Oakes, V. Ciriano-Tejel, D. Wise, M. Fogarty, T. Lundberg, C. Lainé, S. Schaal, F. Martins, D. Ibberson, L. Hutin, B. Bertrand, N. Stelmashenko, J. Robinson, L. Ibberson, A. Hashim, I. Siddiqi, A. Lee, M. Vinet, C. Smith, J. Morton, and M. Gonzalez-Zalba, "Fast high-fidelity single-shot readout of spins in silicon using a single-electron box," arXiv preprint arXiv:2203.06608 (2022).

[141] L. Cochrane, A. A. Seshia, and M. Zalba, "Intrinsic noise of the single electron box," arXiv preprint arXiv:2209.15086 (2022).

[142] L. Taskinen, R. Starrett, T. Martin, A. Micolich, A. Hamilton, M. Simmons, D. Ritchie, and M. Pepper, "Radio-frequency reflectometry on large gated two-dimensional systems," Review of Scientific Instruments **79**, 123901 (2008).

[143] J. Hornibrook, J. Colless, A. Mahoney, X. Croot, S. Blanvillain, H. Lu, A. Gossard, and D. Reilly, "Frequency multiplexing for readout of spin qubits," Applied Physics Letters **104**, 103108 (2014).

[144] N. Ares, F. J. Schupp, A. Mavalankar, G. Rogers, J. Griffiths, G. A. C. Jones, I. Farrer, D. A. Ritchie, C. G. Smith, A. Cottet, G. A. D. Briggs, and E. A. Laird, "Sensitive radio-frequency measurements of a quantum dot by tuning to perfect impedance matching," Phys. Rev. Applied **5**, 034011 (2016).

[145] S. Hellmüller, M. Pikulski, T. Müller, B. Küng, G. Puebla-Hellmann, A. Wallraff, M. Beck, K. Ensslin, and T. Ihn, "Optimization of sample-chip design for stub-matched radio-frequency reflectometry measurements," Applied Physics Letters **101**, 042112 (2012).

[146] A. Betz, R. Wacquez, M. Vinet, X. Jehl, A. Saraiva, M. Sanquer, A. Ferguson, and M. Gonzalez-Zalba, "Dispersively detected pauli spin-blockade in a silicon nanowire field-effect transistor," Nano letters **15**, 4622–4627 (2015).

[147] (), the expressions for the relaxation and dephasing rates from which Eqs. (103) and (106) follow are:

$$\Gamma_1 = \frac{1}{T_1} = \frac{1}{2\hbar^2}\left|\langle 0_\mathrm{q}|\frac{\partial H}{\partial \lambda}|1_\mathrm{q}\rangle\right|^2 S_{\lambda\lambda}\left(\frac{\omega_\mathrm{q}}{2\pi}\right) \tag{166}$$

$$\Gamma_2 = \frac{1}{T_\phi} = \frac{1}{4}\left(\frac{\partial \omega_\mathrm{q}}{\partial \lambda}\right)^2 S_{\lambda\lambda}(0) \tag{167}$$

where $|0_\mathrm{q}\rangle$ and $|1_\mathrm{q}\rangle$ are the qubit eigenstates, ω_q is its angular frequency, and $\lambda(t)$ is a noisy environmental parameter. Equation (167) applies to a Ramsey-type dephasing measurement, provided that the spectral density is approximately constant at low frequency, i.e. that its cutoff frequency is higher than the inverse measurement duration. Often T_ϕ is called T_2^*. These equations can be derived using the method of Ref. 336. A nice pedagogical motivation appears in Ref. 324, although the expression corresponding to Eq. (167) contains a mistake; it appears correctly in Ref. 337.

[148] A. N. Korotkov, "Intrinsic noise of the single-electron transistor," Phys. Rev. B **49**, 10381–10392 (1994).

[149] W. Xue, Z. Ji, F. Pan, J. Stettenheim, M. Blencowe, and A. Rimberg, "Measurement of quantum noise in a single-electron transistor near the quantum limit," Nature Physics **5**, 660–664 (2009).

[150] M. A. Sillanpää, L. Roschier, and P. J. Hakonen, "Charge sensitivity of the inductive single-electron transistor," Applied Physics Letters **87**, 092502 (2005).

[151] T. Lundberg, D. J. Ibberson, J. Li, L. Hutin, J. C. Abadillo-Uriel, M. Filippone, B. Bertrand, A. Nunnenkamp, C.-M. Lee, N. Stelmashenko, J. W. A. Robinson, M. Vinet, L. Ibberson, Y.-M. Niquet, and M. F. Gonzalez-Zalba, "Non-reciprocal pauli spin blockade in a silicon double quantum dot," (2021), arXiv:2110.09842 [cond-mat.mes-hall].

[152] A. Megrant, C. Neill, R. Barends, B. Chiaro, Y. Chen, L. Feigl, J. Kelly, E. Lucero, M. Mariantoni, P. J. J. O'Malley, D. Sank, A. Vainsencher, J. Wenner, T. C. White, Y. Yin, J. Zhao, C. J. Palmstrøm, J. M. Martinis, and A. N. Cleland, "Planar superconducting resonators with internal quality factors above one million," Applied Physics Letters **100**, 113510 (2012), https://doi.org/10.1063/1.3693409.

[153] A. Bruno, G. De Lange, S. Asaad, K. Van Der Enden, N. Langford, and L. DiCarlo, "Reducing intrinsic loss in superconducting resonators by surface treatment and deep etching of silicon substrates," Applied Physics Letters **106**, 182601 (2015).

[154] K. D. Petersson, L. W. McFaul, M. D. Schroer, M. Jung, J. M. Taylor, A. A. Houck, and J. R. Petta, "Circuit quantum electrodynamics with a

spin qubit," Nature **490**, 380–383 (2012).

[155] J. Viennot, M. Dartiailh, A. Cottet, and T. Kontos, "Coherent coupling of a single spin to microwave cavity photons," Science **349**, 408–411 (2015).

[156] M. LaHaye, J. Suh, P. Echternach, K. C. Schwab, and M. L. Roukes, "Nanomechanical measurements of a superconducting qubit," Nature **459**, 960–964 (2009).

[157] T. Palomaki, J. Teufel, R. Simmonds, and K. W. Lehnert, "Entangling mechanical motion with microwave fields," Science **342**, 710–713 (2013).

[158] A. Reed, K. Mayer, J. Teufel, L. Burkhart, W. Pfaff, M. Reagor, L. Sletten, X. Ma, R. Schoelkopf, E. Knill, and K. W. Lehnert, "Faithful conversion of propagating quantum information to mechanical motion," Nature Physics **13**, 1163–1167 (2017).

[159] S. Blien, P. Steger, N. Hüttner, R. Graaf, and A. K. Hüttel, "Quantum capacitance mediated carbon nanotube optomechanics," Nature communications **11**, 1–6 (2020).

[160] A. Laucht, F. Hohls, N. Ubbelohde, M. F. Gonzalez-Zalba, D. J. Reilly, S. Stobbe, T. Schröder, P. Scarlino, J. V. Koski, A. Dzurak, Y. Chih-Hwan, J. Yoneda, F. Kuemmeth, H. Bluhm, J. Pla, C. Hill, J. Salfi, A. Oiwa, J. T. Muhonen, E. Verhagen, M. D. LaHaye, H. Kim Hyun, D. Tsen, Adam W andCulcer, A. Geresdi, J. A. Mol, V. Mohan, K. J. Prashant, and B. Jonathan, "Roadmap on quantum nanotechnologies," Nanotechnology **32**, 162003 (2021).

[161] A. Betz, S. Barraud, Q. Wilmart, B. Placais, X. Jehl, M. Sanquer, and M. Gonzalez-Zalba, "High-frequency characterization of thermionic charge transport in silicon-on-insulator nanowire transistors," Applied Physics Letters **104**, 043106 (2014).

[162] V. D. Maman, M. Gonzalez-Zalba, and A. Pályi, "Charge noise and overdrive errors in dispersive readout of charge, spin, and majorana qubits," Physical Review Applied **14** (2020), 10.1103/PhysRevApplied.14.064024.

[163] G. Johansson, L. Tornberg, and C. Wilson, "Fast quantum limited readout of a superconducting qubit using a slow oscillator," Physical Review B **74**, 100504 (2006).

[164] Y.-Y. Liu, S. Philips, L. Orona, N. Samkharadze, T. McJunkin, E. MacQuarrie, M. Eriksson, L. Vandersypen, and A. Yacoby, "Radio-frequency reflectometry in silicon-based quantum dots," Physical Review Applied **16**, 014057 (2021).

[165] A. Noiri, K. Takeda, J. Yoneda, T. Nakajima, T. Kodera, and S. Tarucha, "Radio-frequency-detected fast charge sensing in undoped silicon quantum dots," Nano Letters **20**, 947–952 (2020).

[166] C. Volk, A. Chatterjee, F. Ansaloni, C. M. Marcus, and F. Kuemmeth, "Fast charge sensing of Si/SiGe quantum dots via a high-frequency accumulation gate," Nano Letters **19**, 5628–5633 (2019).

[167] A. Rossi, R. Zhao, A. Dzurak, and M. Gonzalez-Zalba, "Dispersive readout of a silicon quantum dot with an accumulation-mode gate sensor," Applied Physics Letters **110**, 212101 (2017).

[168] A. West, B. Hensen, A. Jouan, T. Tanttu, C.-H. Yang, A. Rossi, M. F. Gonzalez-Zalba, F. Hudson, A. Morello, D. J. Reilly, and A. S. Dzurak, "Gate-based single-shot readout of spins in silicon," Nature nanotechnology **14**, 437–441 (2019).

[169] A. Aassime, D. Gunnarsson, K. Bladh, P. Delsing, and R. Schoelkopf, "Radio-frequency single-electron transistor: Toward the shot-noise limit," Applied Physics Letters **79**, 4031–4033 (2001).

[170] H. Brenning, S. Kafanov, T. Duty, S. Kubatkin, and P. Delsing, "An ultrasensitive radio-frequency single-electron transistor working up to 4.2 k," Journal of Applied Physics **100**, 114321–114324 (2006).

[171] (), the resolution bandwidth is the width of each frequency bin in the numerically calculated power spectrum. A resolution bandwith Δ_f admits the same amount of white noise as an average over an integration time $\tau_{\rm int} = 1/2\Delta_f$, as proved in Supplementary Section S3.B.3.

[172] M. A. Saifi and L. Cross, "Dielectric properties of strontium titanate at low temperature," Physical Review B **2**, 677 (1970).

[173] T. Sakudo and H. Unoki, "Dielectric Properties of $SrTiO_3$ at Low Temperatures," Phys. Rev. Lett. **26**, 851–853 (1971).

[174] R. Neville, B. Hoeneisen, and C. Mead, "Permittivity of strontium titanate," Journal of Applied Physics **43**, 2124–2131 (1972).

[175] S. Rowley, L. Spalek, R. Smith, M. Dean, M. Itoh, J. Scott, G. Lonzarich, and S. Saxena, "Ferroelectric quantum criticality," Nature Physics **10**, 367–372 (2014).

[176] D. Davidovikj, M. Manca, H. S. J. van der Zant, A. D. Caviglia, and G. A. Steele, "Quantum paraelectricity probed by superconducting resonators," Phys. Rev. B **95**, 214513 (2017).

[177] P. Apostolidis, B. J. Villis, J. F. Chittock-Wood, A. Baumgartner, V. Vesterinen, S. Simbierowicz, J. Hassel, and M. R. Buitelaar, "Quantum paraelectric varactors for radio-frequency measurements at mK temperatures," arXiv (2020), arXiv:2007.03588.

[178] R. G. Geyer, B. Riddle, J. Krupka, and L. A. Boatner, "Microwave dielectric properties of single-crystal quantum paraelectrics KTaO3 and SrTiO3 at cryogenic temperatures," Journal of Applied Physics **97**, 104111 (2005), https://doi.org/10.1063/1.1905789.

[179] C. Altimiras, O. Parlavecchio, P. Joyez, D. Vion, P. Roche, D. Esteve, and F. Portier, "Tunable microwave impedance matching to a high impedance source using a Josephson metamaterial," Applied Physics Letters **103**, 212601 (2013).

[180] G. Zheng, N. Samkharadze, M. L. Noordam, N. Kalhor, D. Brousse, A. Sammak, G. Scappucci, and L. M. Vandersypen, "Rapid gate-based spin read-out in silicon using an on-chip resonator," Nature Nanotechnology **14**, 742–746 (2019).

[181] N. Didier, J. Bourassa, and A. Blais, "Fast quantum nondemolition readout by parametric modulation of longitudinal qubit-oscillator interaction," Phys. Rev. Lett. **115**, 203601 (2015).

[182] (), "Classical" in this context means that the matched resistor's thermal noise is given by the Rayleigh-Jeans approximation $S_{VV}^{\rm N} = k_{\rm B}TZ_0$, i.e. by Eq. (142) instead of Eq. (141). This is only true if $k_{\rm B}T \gg hf$, which does not always hold inside a dilution refrigerator. Despite this fact, most recent authors[185,188] take Eq. (136) to define $T_{\rm N}$ at all frequencies, which is also what we do in this review.
A consequence of this choice is that the noise temperature seen when measuring a matched resistor is not its physical temperature T, but is instead

$$T_{\rm N} = \frac{1}{k_{\rm B}} \frac{hf}{e^{hf/k_{\rm B}T} - 1} \tag{168}$$

as plotted in Fig. 30. Some authors[183] prefer to define noise temperature by insisting that the noise temperature is equal to the resistor's physical temperature; this leads to a noise temperature

$$T_{\rm N}' = \frac{1}{k_{\rm B}} \frac{hf}{\ln\left(\frac{hf}{k_{\rm B}T_{\rm N}} + 1\right)} \tag{169}$$

where $T_{\rm N}$ is our conventional noise temperature defined by Eq. (136). With this choice, the SQL becomes

$$T_{\rm N}' \geq \frac{1}{k_{\rm B}} \frac{hf}{\ln 3} \tag{170}$$

instead of Eq. (143).

[183] C. M. Caves, "Quantum limits on noise in linear amplifiers," Physical Review D **26**, 1817 (1982).

[184] M. A. Castellanos-Beltran, K. D. Irwin, G. C. Hilton, L. R. Vale, and K. W. Lehnert, "Amplification and squeezing of quantum noise with a tunable Josephson metamaterial," Nature Physics **4**, 929–931 (2008).

[185] A. A. Clerk, M. H. Devoret, S. M. Girvin, F. Marquardt, and R. J. Schoelkopf, "Introduction to quantum noise, measurement, and amplification," Reviews of Modern Physics **82**, 1155–1208 (2010).

[186] (), in other words, the fidelity is

$$\mathscr{F} \equiv 1 - \frac{P(\text{‘0’}|1) + P(\text{‘1’}|0)}{2}, \tag{171}$$

where $P(\text{‘0’}|1)$ is the probability to label the state as '0' when the true state is 1, and vice versa. A related quantity is the visibility[21,72], defined as

$$\mathscr{V} \equiv 1 - (P(\text{‘0’}|1) + P(\text{‘1’}|0)) \tag{172}$$
$$= 2\mathscr{F} - 1. \tag{173}$$

Occasionally one sees $\mathscr{V}$ called the fidelity[338,339].
In terms of the signal-to-noise ratio $\text{SNR} \equiv \frac{\text{Peak spacing}}{\text{Standard deviation}}$, the fidelity is

$$\mathscr{F} = \frac{1}{2}\left(1 + \text{erf}\left(\frac{\text{SNR}}{2\sqrt{2}}\right)\right), \tag{174}$$

provided that the peaks in a histogram such as Fig. 24(e-f) are Gaussian and that the qubit does not decay during measurement[338].

[187] (), sometimes SNR is defined as the ratio of signal and noise power, instead of amplitude. With this definition, the SNR plotted in 24(g) is squared.

[188] P. Horowitz and W. Hill, *The Art of Electronics*, 3rd ed. (Cambridge Univ. Press, 2015).

[189] R. Navid, C. Jungemann, T. H. Lee, and R. W. Dutton, "Close-in phase noise in integrated oscillators," in *Proc. SPIE 5473, Noise in Communication* (2004).

[190] S. Weinreb, J. Bardin, H. Mani, and G. Jones, "Matched wideband low-noise amplifiers for radio astronomy," Review of Scientific Instruments **80**, 044702 (2009).

[191] J. Schleeh, G. Alestig, J. Halonen, A. Malmros, B. Nilsson, P. A. Nilsson, J. P. Starski, N. Wadefalk, H. Zirath, and J. Grahn, "Ultralow-power cryogenic InP HEMT with minimum noise temperature of 1 K at 6 GHz," IEEE Electron Device Letters **33**, 664–666 (2012).

[192] M. Mück and R. McDermott, "Radio-frequency amplifiers based on dc SQUIDs," Supercond. Sci. Technol. **23**, 093001 (2010).

[193] (), the name 'dc SQUID' means that the SQUID has more than one junction and therefore shows interference when current-biased at zero frequency. Even when the device is operated at radio frequency, do not confuse it with an 'rf SQUID', which is a loop with only one junction[323].

[194] Y. Wen, N. Ares, F. Schupp, T. Pei, G. Briggs, and E. Laird, "A coherent nanomechanical oscillator driven by single-electron tunnelling," Nature physics **16**, 75–82 (2020).

[195] N. A. Court, D. J. Reilly, T. M. Buehler, R. P. Starrett, and R. G. Clark, "Toward a quantum-limited charge detector," in *Smart Structures, Devices, and Systems II*, Vol. 5649 (International Society for Optics and Photonics, 2005) pp. 311–315.

[196] F. Schupp, F. Vigneau, Y. Wen, A. Mavalankar, J. Griffiths, G. Jones, I. Farrer, D. Ritchie, C. Smith, L. Camenzind, L. Yu, D. M. Zumbühl, G. A. D. Briggs, N. Ares, and E. A. Laird, "Sensitive radiofrequency readout of quantum dots using an ultra-low-noise squid amplifier," Journal of Applied Physics **127**, 244503 (2020).

[197] J. Aumentado, "Superconducting parametric amplifiers," IEEE Microwave Magazine **21**, 45–59 (2020).

[198] M. A. Castellanos-Beltran and K. W. Lehnert, "Widely tunable parametric amplifier based on a superconducting quantum interference device array resonator," Applied Physics Letters **91** (2007), 10.1063/1.2773988, 0706.2373.

[199] T. Yamamoto, K. Inomata, M. Watanabe, K. Matsuba, T. Miyazaki, W. D. Oliver, Y. Nakamura, and J. S. Tsai, "Flux-driven Josephson parametric amplifier," Applied Physics Letters **93**, 91–94 (2008).

[200] This type of operation, in which the pump is at twice the signal frequency, is called degenerate parametric amplification. This is not the only way to operate a parametric amplifier, but it is the most intuitive.

[201] M. H. Devoret, A. Wallraff, and J. M. Martinis, "Superconducting qubits: A short review," arXiv preprint cond-mat/0411174 (2004).

[202] (), this equation follows from the Josephson equations and the definition $V = L\frac{dI}{dt}$. Some authors[198,340] prefer to define the inductance L' by $V = \frac{d}{dt}(L'I)$, which leads to $L'_J = \frac{\hbar}{2eI_0}\frac{\sin^{-1}(I/I_0)}{I/I_0}$. This is equivalent to Eq. (147) when $I \ll I_0$.

[203] S. Schaal, I. Ahmed, J. A. Haigh, L. Hutin, B. Bertrand, S. Barraud, M. Vinet, C. M. Lee, N. Stelmashenko, J. W. Robinson, J. Y. Qiu, S. Hacohen-Gourgy, I. Siddiqi, M. F. Gonzalez-Zalba, and J. J. L. Morton, "Fast Gate-Based Readout of Silicon Quantum Dots Using Josephson Parametric Amplification," Phys. Rev. Lett. **124**, 67701 (2020).

[204] C. Macklin, K. O'Brien, D. Hover, M. E. Schwartz, V. Bolkhovsky, X. Zhang, W. D. Oliver, and I. Siddiqi, "A near – quantum-limited Josephson traveling-wave parametric amplifier," Science **350**, 307 (2015).

[205] M. Mück, J. B. Kycia, and J. Clarke, "Superconducting quantum interference device as a near-quantum-limited amplifier at 0.5 GHz," Appl. Phys. Lett. **78**, 967 (2001).

[206] S. J. Asztalos, G. Carosi, C. Hagmann, D. Kinion, K. Van Bibber, M. Hotz, L. J. Rosenberg, G. Rybka, J. Hoskins, J. Hwang, P. Sikivie, D. B. Tanner, R. Bradley, and J. Clarke, "SQUID-based microwave cavity search for dark-matter axions," Phys. Rev. Lett. **104**, 041301 (2010).

[207] S. Simbierowicz, V. Vesterinen, L. Grönberg, J. Lehtinen, M. Prunnila, and J. Hassel, "A flux-driven Josephson parametric amplifier for sub-GHz frequencies fabricated with side-wall passivated spacer junction technology," Supercond. Sci. Technol. **31**, 105001 (2018).

[208] A. Bienfait, P. Campagne-Ibarcq, A. H. Kiilerich, X. Zhou, S. Probst, J. J. Pla, T. Schenkel, D. Vion, D. Esteve, J. J. Morton, K. Moelmer, and P. Bertet, "Magnetic resonance with squeezed microwaves," Physical Review X **7**, 041011 (2017).

[209] A. Eddins, S. Schreppler, D. M. Toyli, L. S. Martin, S. Hacohen-Gourgy, L. C. Govia, H. Ribeiro, A. A. Clerk, and I. Siddiqi, "Stroboscopic Qubit Measurement with Squeezed Illumination," Physical Review Letters **120**, 40505 (2018).

[210] M. Malnou, D. A. Palken, B. M. Brubaker, L. R. Vale, G. C. Hilton, and K. W. Lehnert, "Squeezed Vacuum Used to Accelerate the Search for a Weak Classical Signal," Physical Review X **9**, 21023 (2019).

[211] K. M. Backes, D. A. Palken, S. A. Kenany, B. M. Brubaker, S. B. Cahn, A. Droster, G. C. Hilton, S. Ghosh, H. Jackson, S. K. Lamoreaux, A. F. Leder, K. W. Lehnert, S. M. Lewis, M. Malnou, R. H. Maruyama, N. M. Rapidis, M. Simanovskaia, S. Singh, D. H. Speller, I. Urdinaran, L. R. Vale, E. C. van Assendelft, K. van Bibber, and H. Wang, "A quantum enhanced search for dark matter axions," Nature **590**, 238 (2021).

[212] A. T. Jones, C. P. Scheller, J. R. Prance, Y. B. Kalyoncu, D. M. Zumbühl, and R. P. Haley, "Progress in Cooling Nanoelectronic Devices to Ultra-Low Temperatures," Journal of Low Temperature Physics **201**, 772–802 (2020).

[213] M. Malnou, M. R. Vissers, J. D. Wheeler, J. Aumentado, J. Hubmayr, J. N. Ullom, and J. Gao, "A three-wave mixing kinetic inductance traveling-wave amplifier with near-quantum-limited noise performance," PRX Quantum **2**, 010302 (2021).

[214] F. Luthi, T. Stavenga, O. W. Enzing, A. Bruno, C. Dickel, N. K. Langford, M. A. Rol, T. S. Jespersen, J. Nygård, P. Krogstrup, and L. DiCarlo, "Evolution of Nanowire Transmon Qubits and Their Coherence in a Magnetic Field," Physical Review Letters **120**, 100502 (2018).

[215] J. G. Kroll, W. Uilhoorn, K. L. van der Enden, D. de Jong, K. Watanabe, T. Taniguchi, S. Goswami, M. C. Cassidy, and L. P. Kouwenhoven, "Magnetic field compatible circuit quantum electrodynamics with graphene Josephson junctions," Nature Communications **9**, 4615 (2018).

[216] C. F. Ockeloen-Korppi, E. Damskägg, J.-M. Pirkkalainen, T. T. Heikkilä, F. Massel, and M. A. Sillanpää, "Noiseless Quantum Measurement and Squeezing of Microwave Fields Utilizing Mechanical Vibrations," Physical Review Letters **118**, 103601 (2017).

[217] L. Cochrane, T. Lundberg, D. J. Ibberson, L. A. Ibberson, L. Hutin, B. Bertrand, N. Stelmashenko, J. W. A. Robinson, M. Vinet, A. A. Seshia, and M. F. Gonzalez-Zalba, "Parametric amplifiers based on quantum dots," Phys. Rev. Lett. **128**, 197701 (2022).

[218] A. Eddins, J. M. Kreikebaum, D. M. Toyli, E. M. Levenson-Falk, A. Dove, W. P. Livingston, B. A. Levitan, L. C. Govia, A. A. Clerk, and I. Siddiqi, "High-Efficiency Measurement of an Artificial Atom Embedded in a Parametric Amplifier," Physical Review X **9**, 11004 (2019).

[219] D. Reilly, "Challenges in scaling-up the control interface of a quantum computer," in *2019 IEEE International Electron Devices Meeting (IEDM)* (IEEE, 2019) pp. 31–7.

[220] A. Ruffino, T.-Y. Yang, J. Michniewicz, Y. Peng, E. Charbon, and M. F. Gonzalez-Zalba, "A cryo-cmos chip that integrates silicon quantum dots and multiplexed dispersive readout electronics," Nature Electronics **5**, 53–59 (2022).

[221] T. M. Buehler, D. J. Reilly, R. P. Starrett, N. A. Court, A. R. Hamilton, A. S. Dzurak, and R. G. Clark, "Development and operation of the twin radio frequency single electron transistor for cross-correlated charge detection," Journal of Applied Physics **96**, 4508–4513 (2004), https://doi.org/10.1063/1.1786671.

[222] J. Kroll, F. Borsoi, K. van der Enden, W. Uilhoorn, D. de Jong, M. Quintero-Pérez, D. van Woerkom, A. Bruno, S. Plissard, D. Car, E. Bakkers, M. Cassidy, and L. Kouwenhoven, "Magnetic-field-resilient superconducting coplanar-waveguide resonators for hybrid circuit quantum electrodynamics experiments," Phys. Rev. Applied **11**, 064053 (2019).

[223] T. Daniel, *Sank. Fast, Accurate State Measurement in Superconducting Qubits*, Ph.D. thesis, PhD thesis, University of California Santa Barbara (2014).

[224] J. Hornibrook, J. Colless, I. C. Lamb, S. Pauka, H. Lu, A. Gossard, J. Watson, G. Gardner, S. Fallahi, M. Manfra, and R. D. J., "Cryogenic control architecture for large-scale quantum computing," Physical Review Applied **3**, 024010 (2015).

[225] S. Schaal, S. Barraud, J. J. L. Morton, and M. F. Gonzalez-Zalba, "Conditional Dispersive Readout of a CMOS Single-Electron Memory Cell," Phys. Rev. Applied **9**, 054016 (2018).

[226] S. Schaal, A. Rossi, V. N. Ciriano-Tejel, T.-Y. Yang, S. Barraud, J. J. Morton, and M. F. Gonzalez-Zalba, "A CMOS dynamic random access architecture for radio-frequency readout of quantum devices," Nature Electronics **2**, 236–242 (2019).
[227] M. C. Jarratt, J. Hornibrook, X. Croot, J. Watson, G. Gardner, S. Fallahi, M. Manfra, and D. Reilly, "Time division multiplexing of semiconductor qubits," in *APS March Meeting Abstracts*, Vol. 2017 (2017) pp. E52–012.
[228] S. Pauka, K. Das, J. Hornibrook, G. Gardner, M. Manfra, M. Cassidy, and D. Reilly, "Characterizing quantum devices at scale with custom cryo-CMOS," Physical Review Applied **13**, 054072 (2020).
[229] A. Mahoney, J. Colless, S. Pauka, J. Hornibrook, J. Watson, G. Gardner, M. Manfra, A. Doherty, and D. Reilly, "On-chip microwave quantum hall circulator," Physical Review X **7**, 011007 (2017).
[230] A. C. Mahoney, J. I. Colless, L. Peeters, S. J. Pauka, E. J. Fox, X. Kou, L. Pan, K. L. Wang, D. Goldhaber-Gordon, and D. J. Reilly, "Zero-field edge plasmons in a magnetic topological insulator," Nature communications **8**, 1–7 (2017).
[231] A. J. Annunziata, D. F. Santavicca, L. Frunzio, G. Catelani, M. J. Rooks, A. Frydman, and D. E. Prober, "Tunable superconducting nanoinductors," Nanotechnology **21** (2010), 10.1088/0957-4484/21/44/445202.
[232] B. Prabowo, G. Zheng, M. Mehrpoo, B. Patra, P. Harvey-Collard, J. Dijkema, A. Sammak, G. Scappucci, E. Charbon, F. Sebastiano, L. M. K. Vandersypen, and M. Babaie, "13.3 A 6-to-8GHz 0.17mW/Qubit Cryo-CMOS Receiver for Multiple Spin Qubit Readout in 40nm CMOS Technology," (2021) pp. 212–214.
[233] A. Ruffino, Y. Peng, T. Y. Yang, J. Michniewicz, M. F. Gonzalez-Zalba, and E. Charbon, "13.2 A Fully-Integrated 40-nm 5-6.5 GHz Cryo-CMOS System-on-Chip with I/Q Receiver and Frequency Synthesizer for Scalable Multiplexed Readout of Quantum Dots," (2021) pp. 210–212.
[234] K. C. Nowack, F. Koppens, Y. V. Nazarov, and L. Vandersypen, "Coherent control of a single electron spin with electric fields," Science **318**, 1430–1433 (2007).
[235] A. Chatterjee, P. Stevenson, S. De Franceschi, A. Morello, N. P. de Leon, and F. Kuemmeth, "Semiconductor qubits in practice," Nature Reviews Physics **3**, 157–177 (2021).
[236] F. A. Zwanenburg, A. S. Dzurak, A. Morello, M. Y. Simmons, L. C. L. Hollenberg, G. Klimeck, S. Rogge, S. N. Coppersmith, and M. A. Eriksson, "Silicon quantum electronics," Rev. Mod. Phys. **85**, 961–1019 (2013).
[237] S. Schaal and M. F. Gonzalez-Zalba, "Chapter eight - silicon qubit devices," in *Semiconductor Nanodevices*, Frontiers of Nanoscience, Vol. 20, edited by D. A. Ritchie (Elsevier, 2021) pp. 265–293.
[238] M. Gonzalez-Zalba, S. de Franceschi, E. Charbon, T. Meunier, M. Vinet, and A. Dzurak, "Scaling silicon-based quantum computing using cmos technology," Nature Electronics **4**, 872–884 (2021).
[239] K. Ono, D. Austing, Y. Tokura, and S. Tarucha, "Current rectification by pauli exclusion in a weakly coupled double quantum dot system," Science **297**, 1313–1317 (2002).
[240] R. Hanson, L. W. van Beveren, I. Vink, J. Elzerman, W. Naber, F. Koppens, L. Kouwenhoven, and L. Vandersypen, "Single-shot readout of electron spin states in a quantum dot using spin-dependent tunnel rates," Physical review letters **94**, 196802 (2005).
[241] L. P. Kouwenhoven, D. Austing, and S. Tarucha, "Few-electron quantum dots," Reports on Progress in Physics **64**, 701 (2001).
[242] M. Schroer, M. Jung, K. Petersson, and J. R. Petta, "Radio frequency charge parity meter," Physical review letters **109**, 166804 (2012).
[243] J. van der Heijden, T. Kobayashi, M. G. House, J. Salfi, S. Barraud, R. Laviéville, M. Y. Simmons, and S. Rogge, "Readout and control of the spin-orbit states of two coupled acceptor atoms in a silicon transistor," Science advances **4**, eaat9199 (2018).
[244] A. Crippa, R. Ezzouch, A. Aprá, A. Amisse, R. Laviéville, L. Hutin, B. Bertrand, M. Vinet, M. Urdampilleta, T. Meunier, M. Sanquer, X. Jehl, R. Maurand, and S. De Franceschi, "Gate-reflectometry dispersive readout and coherent control of a spin qubit in silicon," Nature Communications **10**, 2776 (2019).
[245] A. G. Fowler, M. Mariantoni, J. M. Martinis, and A. N. Cleland, "Surface codes: Towards practical large-scale quantum computation," Physical Review A **86**, 032324 (2012).
[246] T. F. Watson, B. Weber, Y. L. Hsueh, L. C. Hollenberg, R. Rahman, and M. Y. Simmons, "Atomically engineered electron spin lifetimes of 30 s in silicon," Science Advances **3**, e1602811 (2017).
[247] P. Pakkiam, A. V. Timofeev, M. G. House, M. R. Hogg, T. Kobayashi, M. Koch, S. Rogge, and M. Y. Simmons, "Single-shot single-gate rf spin readout in silicon," Phys. Rev. X **8**, 041032 (2018).
[248] P. Harvey-Collard, B. D'Anjou, M. Rudolph, N. Tobias Jacobson, J. Dominguez, G. A. Eyck, J. R. Wendt, T. Pluym, M. P. Lilly, W. A. Coish, M. Pioro-Ladrière, and M. S. Carroll, "High-Fidelity Single-Shot Readout for a Spin Qubit via an Enhanced Latching Mechanism," Physical Review X **8**, 021046 (2018).
[249] D. Keith, S. Gorman, L. Kranz, Y. He, J. Keizer, M. Broome, and M. Simmons, "Benchmarking high fidelity single-shot readout of semiconductor qubits," New Journal of Physics **21**, 063011 (2019).
[250] D. Keith, M. G. House, M. B. Donnelly, T. F. Watson, B. Weber, and M. Y. Simmons, "Single-shot spin readout in semiconductors near the shot-noise sensitivity limit," Phys. Rev. X **9**, 041003 (2019).
[251] High-frequency PCB sample holders are available from QDevil (www.qdevil.com) .
[252] X. Mi, J. Cady, D. Zajac, P. Deelman, and J. R. Petta, "Strong coupling of a single electron in silicon to a microwave photon," Science **355**, 156–158 (2017).
[253] N. Samkharadze, G. Zheng, N. Kalhor, D. Brousse, A. Sammak, U. Mendes, A. Blais, G. Scappucci, and L. Vandersypen, "Strong spin-photon coupling in silicon," Science **359**, 1123–1127 (2018).
[254] K. Kalashnikov, W. T. Hsieh, W. Zhang, W.-S. Lu, P. Kamenov, A. Di Paolo, A. Blais, M. E. Gershenson, and M. Bell, "Bifluxon: Fluxon-parity-protected superconducting qubit," PRX Quantum **1**, 010307 (2020).
[255] M. Kjaergaard, M. E. Schwartz, J. Braumüller, P. Krantz, J. I.-J. Wang, S. Gustavsson, and W. D. Oliver, "Superconducting qubits: Current state of play," Annual Review of Condensed Matter Physics **11**, 369–395 (2020), https://doi.org/10.1146/annurev-conmatphys-031119-050605.
[256] M. T. Bell, J. Paramanandam, L. B. Ioffe, and M. E. Gershenson, "Protected josephson rhombus chains," Phys. Rev. Lett. **112**, 167001 (2014).
[257] T. W. Larsen, M. E. Gershenson, L. Casparis, A. Kringhøj, N. J. Pearson, R. P. G. McNeil, F. Kuemmeth, P. Krogstrup, K. D. Petersson, and C. M. Marcus, "Parity-protected superconductor-semiconductor qubit," Phys. Rev. Lett. **125**, 056801 (2020).
[258] A. Gyenis, P. S. Mundada, A. Di Paolo, T. M. Hazard, X. You, D. I. Schuster, J. Koch, A. Blais, and A. A. Houck, "Experimental realization of a protected superconducting circuit derived from the 0–π qubit," PRX Quantum **2**, 010339 (2021).
[259] A. Gyenis, A. Di Paolo, J. Koch, A. Blais, A. A. Houck, and D. I. Schuster, "Moving beyond the transmon: Noise-protected superconducting quantum circuits," PRX Quantum **2**, 030101 (2021).
[260] L. B. Ioffe and M. V. Feigel'man, "Possible realization of an ideal quantum computer in josephson junction array," Phys. Rev. B **66**, 224503 (2002).
[261] B. Douçot and J. Vidal, "Pairing of cooper pairs in a fully frustrated josephson-junction chain," Phys. Rev. Lett. **88**, 227005 (2002).
[262] A. Kitaev, "Protected qubit based on a superconducting current mirror," arXiv preprint cond-mat/0609441 (2006).
[263] P. Brooks, A. Kitaev, and J. Preskill, "Protected gates for superconducting qubits," Phys. Rev. A **87**, 052306 (2013).
[264] Y.-H. Lin, L. B. Nguyen, N. Grabon, J. San Miguel, N. Pankratova, and V. E. Manucharyan, "Demonstration of protection of a superconducting qubit from energy decay," Phys. Rev. Lett. **120**, 150503 (2018).
[265] J. Koch, T. M. Yu, J. Gambetta, A. A. Houck, D. I. Schuster, J. Majer, A. Blais, M. H. Devoret, S. M. Girvin, and R. J. Schoelkopf, "Charge-insensitive qubit design derived from the cooper pair box," Phys. Rev. A **76**, 042319 (2007).
[266] M. T. Bell, L. B. Ioffe, and M. E. Gershenson, "Microwave spectroscopy of a cooper-pair transistor coupled to a lumped-element resonator," Phys. Rev. B **86**, 144512 (2012).
[267] D. De Jong, J. Van Veen, L. Binci, A. Singh, P. Krogstrup, L. P. Kouwenhoven, W. Pfaff, and J. D. Watson, "Rapid Detection of Coherent Tunneling in an InAs Nanowire Quantum Dot through Dispersive Gate Sensing," Physical Review Applied **11**, 044061 (2019).
[268] S. M. Albrecht, A. P. Higginbotham, M. Madsen, F. Kuemmeth, T. S. Jespersen, J. Nygård, P. Krogstrup, and C. Marcus, "Exponential protection of zero modes in majorana islands," Nature **531**, 206–209 (2016).
[269] Y. Ando and L. Fu, "Topological crystalline insulators and topological superconductors: From concepts to materials," Annu. Rev. Condens. Matter Phys. **6**, 361–381 (2015).

[270]N. P. Armitage, E. J. Mele, and A. Vishwanath, "Weyl and dirac semimetals in three-dimensional solids," Rev. Mod. Phys. **90**, 015001 (2018).

[271]C. Nayak, S. H. Simon, A. Stern, M. Freedman, and S. Das Sarma, "Non-abelian anyons and topological quantum computation," Rev. Mod. Phys. **80**, 1083–1159 (2008).

[272]L. Fu, "Electron teleportation via majorana bound states in a mesoscopic superconductor," Physical review letters **104**, 056402 (2010).

[273]D. Aasen, M. Hell, R. V. Mishmash, A. Higginbotham, J. Danon, M. Leijnse, T. S. Jespersen, J. A. Folk, C. M. Marcus, K. Flensberg, and J. Alicea, "Milestones toward majorana-based quantum computing," Phys. Rev. X **6**, 031016 (2016).

[274]S. Plugge, A. Rasmussen, R. Egger, and K. Flensberg, "Majorana box qubits," New Journal of Physics **19**, 012001 (2017).

[275]J. J. Wesdorp, L. Grünhaupt, A. Vaartjes, M. Pita-Vidal, A. Bargerbos, L. J. Splitthoff, P. Krogstrup, B. van Heck, and G. de Lange, "Dynamical polarization of the fermion parity in a nanowire josephson junction," arXiv preprint cond-mat/2112.01936 (2021).

[276]R. De-Picciotto, M. Reznikov, M. Heiblum, V. Umansky, G. Bunin, and D. Mahalu, "Direct observation of a fractional charge," Physica B: Condensed Matter **249**, 395–400 (1998).

[277]R. Landauer, "The noise is the signal," Nature **392**, 658–659 (1998).

[278]R. Depicciotto, M. Reznikov, M. Heiblum, V. Umansky, G. Bunin, and D. Mahalu, "Direct observation of a fractional charge," Nature **389**, 162–164 (1997).

[279]M. Banerjee, M. Heiblum, A. Rosenblatt, Y. Oreg, D. E. Feldman, A. Stern, and V. Umansky, "Observed quantization of anyonic heat flow," Nature **545**, 75–79 (2017).

[280]P. A. Truitt, J. B. Hertzberg, C. Huang, K. L. Ekinci, and K. C. Schwab, "Efficient and sensitive capacitive readout of nanomechanical resonator arrays," Nano letters **7**, 120–126 (2007).

[281]N. Ares, T. Pei, A. Mavalankar, M. Mergenthaler, J. H. Warner, G. A. D. Briggs, and E. A. Laird, "Resonant optomechanics with a vibrating carbon nanotube and a radio-frequency cavity," Physical review letters **117**, 170801 (2016).

[282]K. S. Van Dyke, "The piezo-electric resonator and its equivalent network," Proceedings of the Institute of Radio Engineers **16**, 742–764 (1928).

[283]S. De Bonis, C. Urgell, W. Yang, C. Samanta, A. Noury, J. Vergara-Cruz, Q. Dong, Y. Jin, and A. Bachtold, "Ultrasensitive displacement noise measurement of carbon nanotube mechanical resonators," Nano letters **18**, 5324–5328 (2018).

[284]Y. Wen, N. Ares, T. Pei, G. Briggs, and E. A. Laird, "Measuring carbon nanotube vibrations using a single-electron transistor as a fast linear amplifier," Applied Physics Letters **113**, 153101 (2018).

[285]C. Urgell, W. Yang, S. De Bonis, C. Samanta, M. J. Esplandiu, Q. Dong, Y. Jin, and A. Bachtold, "Cooling and self-oscillation in a nanotube electromechanical resonator," Nature Physics **16**, 32–37 (2020).

[286]J. Chaste, A. Eichler, J. Moser, G. Ceballos, R. Rurali, and A. Bachtold, "A nanomechanical mass sensor with yoctogram resolution," Nature nanotechnology **7**, 301–304 (2012).

[287]J. Moser, J. Güttinger, A. Eichler, M. J. Esplandiu, D. Liu, M. Dykman, and A. Bachtold, "Ultrasensitive force detection with a nanotube mechanical resonator," Nature nanotechnology **8**, 493–496 (2013).

[288]E. K. Irish and K. Schwab, "Quantum measurement of a coupled nanomechanical resonator–cooper-pair box system," Physical Review B **68**, 155311 (2003).

[289]C. Chen, V. V. Deshpande, M. Koshino, S. Lee, A. Gondarenko, A. H. MacDonald, P. Kim, and J. Hone, "Modulation of mechanical resonance by chemical potential oscillation in graphene," Nature Physics **12**, 240–244 (2016).

[290]I. Khivrich, A. A. Clerk, and S. Ilani, "Nanomechanical pump–probe measurements of insulating electronic states in a carbon nanotube," Nature nanotechnology **14**, 161–167 (2019).

[291]M. Kim, J. Kim, Y. Hou, D. Yu, Y.-J. Doh, B. Kim, K. W. Kim, and J. Suh, "Nanomechanical characterization of quantum interference in a topological insulator nanowire," Nature communications **10**, 1–7 (2019).

[292]M. Aspelmeyer, T. J. Kippenberg, and F. Marquardt, "Cavity optomechanics," Rev. Mod. Phys. **86**, 1391–1452 (2014).

[293]A. D. O'Connell, M. Hofheinz, M. Ansmann, R. C. Bialczak, M. Lenander, E. Lucero, M. Neeley, D. Sank, H. Wang, M. Weides, J. Wenner, J. M. Martinis, and A. N. Cleland, "Quantum ground state and single-phonon control of a mechanical resonator," Nature **464**, 697–703 (2010).

[294]K. E. Khosla, M. R. Vanner, N. Ares, and E. A. Laird, "Displacemon electromechanics: How to detect quantum interference in a nanomechanical resonator," Phys. Rev. X **8**, 021052 (2018).

[295]M. Kounalakis, Y. M. Blanter, and G. A. Steele, "Flux-mediated optomechanics with a transmon qubit in the single-photon ultrastrong-coupling regime," Physical Review Research **2**, 023335 (2020).

[296]F. Pistolesi, A. N. Cleland, and A. Bachtold, "Proposal for a nanomechanical qubit," Phys. Rev. X **11**, 031027 (2021).

[297]A. Pearson, K. Khosla, M. Mergenthaler, G. A. D. Briggs, E. Laird, and N. Ares, "Radio-frequency optomechanical characterization of a silicon nitride drum," Scientific reports **10**, 1–7 (2020).

[298]B. Karimi and J. P. Pekola, "Noninvasive thermometer based on the zero-bias anomaly of a superconducting junction for ultrasensitive calorimetry," Physical Review Applied **10**, 054048 (2018).

[299]D. Schmidt, C. Yung, and A. Cleland, "Nanoscale radio-frequency thermometry," Applied physics letters **83**, 1002–1004 (2003).

[300]R. Webb, R. P. Giffard, and J. Wheatley, "Noise thermometry at ultralow temperatures," Journal of Low Temperature Physics **13**, 383–429 (1973).

[301]M. Aalto, H. Collan, R. Gylling, and K. Nores, "A Pulsed NMR System for Nuclear Thermometry Below 2 K," Review of Scientific Instruments **44**, 1075–1082 (1973).

[302]H. Q. Nguyen, J. T. Peltonen, M. Meschke, and J. P. Pekola, "Cascade electronic refrigerator using superconducting tunnel junctions," Phys. Rev. Applied **6**, 054011 (2016).

[303]J. Chawner, S. Barraud, M. Gonzalez-Zalba, S. Holt, E. Laird, Y. A. Pashkin, and J. Prance, "Nongalvanic calibration and operation of a quantum dot thermometer," Phys. Rev. Applied **15**, 034044 (2021).

[304]F. Blanchet, Y.-C. Chang, B. Karimi, J. T. Peltonen, and J. P. Pekola, "Radio-frequency coulomb-blockade thermometry," Phys. Rev. Applied **17**, L011003 (2022).

[305]F. m. c. Léonard and J. Tersoff, "Novel length scales in nanotube devices," Phys. Rev. Lett. **83**, 5174–5177 (1999).

[306]A. A. Odintsov, "Schottky barriers in carbon nanotube heterojunctions," Phys. Rev. Lett. **85**, 150–153 (2000).

[307]S. Ilani, J. Martin, E. Teitelbaum, J. Smet, D. Mahalu, V. Umansky, and A. Yacoby, "The microscopic nature of localization in the quantum hall effect," Nature **427**, 328–332 (2004).

[308]J. Martin, S. Ilani, B. Verdene, J. Smet, V. Umansky, D. Mahalu, D. Schuh, G. Abstreiter, and A. Yacoby, "Localization of fractionally charged quasi-particles," Science **305**, 980–983 (2004).

[309]V. Venkatachalam, A. Yacoby, L. Pfeiffer, and K. West, "Local charge of the ν= 5/2 fractional quantum hall state," Nature **469**, 185–188 (2011).

[310]J. Martin, N. Akerman, G. Ulbricht, T. Lohmann, J. v. Smet, K. Von Klitzing, and A. Yacoby, "Observation of electron–hole puddles in graphene using a scanning single-electron transistor," Nature physics **4**, 144–148 (2008).

[311]Y. Cao, V. Fatemi, A. Demir, S. Fang, S. L. Tomarken, J. Y. Luo, J. D. Sanchez-Yamagishi, K. Watanabe, T. Taniguchi, E. Kaxiras, R. C. Ashoori, and P. Jarillo-Herrero, "Correlated insulator behaviour at half-filling in magic-angle graphene superlattices," Nature **556**, 80–84 (2018).

[312]M. Bockrath, D. H. Cobden, J. Lu, A. G. Rinzler, R. E. Smalley, L. Balents, and P. L. McEuen, "Luttinger-liquid behaviour in carbon nanotubes," Nature **397**, 598–601 (1999).

[313]O. Auslaender, H. Steinberg, . A. Yacoby, . Y. Tserkovnyak, B. Halperin, K. Baldwin, L. Pfeiffer, and K. West, "Spin-charge separation and localization in one dimension," Science **308**, 88–92 (2005).

[314]V. V. Deshpande, M. Bockrath, L. I. Glazman, and A. Yacoby, "Electron liquids and solids in one dimension," Nature **464**, 209–216 (2010).

[315]S. Pecker, F. Kuemmeth, A. Secchi, M. Rontani, D. Ralph, P. McEuen, and S. Ilani, "Observation and spectroscopy of a two-electron wigner molecule in an ultraclean carbon nanotube," Nature Physics **9**, 576–581 (2013).

[316]I. Shapir, A. Hamo, S. Pecker, C. Moca, Ö. Legeza, G. Zarand, and S. Ilani, "Imaging the electronic wigner crystal in one dimension," Science **364**, 870–875 (2019).

[317]D. Wharam, T. J. Thornton, R. Newbury, M. Pepper, H. Ahmed, J. Frost, D. Hasko, D. Peacock, D. Ritchie, and G. Jones, "One-dimensional transport and the quantisation of the ballistic resistance," Journal of Physics C: solid state physics **21**, L209 (1988).

[318] F. Bauer, J. Heyder, E. Schubert, D. Borowsky, D. Taubert, B. Bruognolo, D. Schuh, W. Wegscheider, J. von Delft, and S. Ludwig, "Microscopic origin of the '0.7-anomaly' in quantum point contacts," Nature **501**, 73–78 (2013).

[319] M. Iqbal, R. Levy, E. Koop, J. Dekker, J. De Jong, J. van der Velde, D. Reuter, A. Wieck, R. Aguado, Y. Meir, and C. Van Der Wal, "Odd and even kondo effects from emergent localization in quantum point contacts," Nature **501**, 79–83 (2013).

[320] X. Croot, S. Pauka, M. Jarratt, H. Lu, A. Gossard, J. Watson, G. Gardner, S. Fallahi, M. Manfra, and D. Reilly, "Gate-sensing charge pockets in the semiconductor-qubit environment," Physical Review Applied **11**, 064027 (2019).

[321] B. Dober, D. Becker, D. Bennett, S. Bryan, S. Duff, J. Gard, J. Hays-Wehle, G. Hilton, J. Hubmayr, J. Mates, C. D. Reintsema, L. R. Vale, and J. N. Ullom, "Microwave SQUID multiplexer demonstration for cosmic microwave background imagers," Applied Physics Letters **111**, 243510 (2017).

[322] S. Kempf, M. Wegner, A. Fleischmann, L. Gastaldo, F. Herrmann, M. Papst, D. Richter, and C. Enss, "Demonstration of a scalable frequency-domain readout of metallic magnetic calorimeters by means of a microwave SQUID multiplexer," AIP Advances **7**, 015007 (2017), https://doi.org/10.1063/1.4973872.

[323] J. Clarke and A. I. Braginski, *The SQUID Handbook: Vol 1 Fundamentals and Technology of SQUIDs and SQUID Systems* (Wiley-VCH, 2004).

[324] P. Krantz, M. Kjaergaard, F. Yan, T. P. Orlando, S. Gustavsson, and W. D. Oliver, "A quantum engineer's guide to superconducting qubits," Applied Physics Reviews **6**, 021318 (2019), https://doi.org/10.1063/1.5089550.

[325] D. de Jong, C. G. Prosko, D. M. A. Waardenburg, L. Han, F. K. Malinowski, P. Krogstrup, L. P. Kouwenhoven, J. V. Koski, and W. Pfaff, "Rapid microwave-only characterization and readout of quantum dots using multiplexed gigahertz-frequency resonators," Phys. Rev. Applied **16**, 014007 (2021).

[326] H. Moon, D. T. Lennon, J. Kirkpatrick, N. M. van Esbroeck, L. C. Camenzind, L. Yu, F. Vigneau, D. M. Zumbühl, G. A. D. Briggs, M. A. Osborne, D. Sejdinovic, E. Laird, and N. Ares, "Machine learning enables completely automatic tuning of a quantum device faster than human experts," Nature communications **11**, 1–10 (2020).

[327] N. M. van Esbroeck, D. T. Lennon, H. Moon, V. Nguyen, F. Vigneau, L. C. Camenzind, L. Yu, D. M. Zumbühl, G. A. D. Briggs, D. Sejdinovic, E. Laird, and N. Ares, "Quantum device fine-tuning using unsupervised embedding learning," New Journal of Physics **22**, 095003 (2020).

[328] J. P. Zwolak, T. McJunkin, S. S. Kalantre, J. Dodson, E. MacQuarrie, D. Savage, M. Lagally, S. Coppersmith, M. A. Eriksson, and J. M. Taylor, "Autotuning of double-dot devices in situ with machine learning," Phys. Rev. Applied **13**, 034075 (2020).

[329] F. K. Malinowski, L. Han, D. de Jong, J.-Y. Wang, C. G. Prosko, G. Badawy, S. Gazibegovic, Y. Liu, P. Krogstrup, E. P. Bakkers, L. P. Kouwenhoven, and J. V. Koski, "Radio-frequency c-v measurements with subattofarad sensitivity," Phys. Rev. Applied **18**, 024032 (2022).

[330] D. N. Nguyen, J. Michel, and C. H. Mielke, "Status and development of pulsed magnets at the NHMFL pulsed field facility," IEEE Transactions on Applied Superconductivity **26**, 1–5 (2016).

[331] J. Béard, J. Billette, N. Ferreira, P. Frings, J.-M. Lagarrigue, F. Lecouturier, and J.-P. Nicolin, "Design and tests of the 100-T triple coil at LNCMI," IEEE Transactions on Applied Superconductivity **28**, 1–5 (2017).

[332] M. M. Desjardins, J. J. Viennot, M. C. Dartiailh, L. E. Bruhat, M. R. Delbecq, M. Lee, M.-S. Choi, A. Cottet, and T. Kontos, "Observation of the frozen charge of a Kondo resonance," Nature **545**, 71 (2017).

[333] A. Stockklauser, P. Scarlino, J. V. Koski, S. Gasparinetti, C. K. Andersen, C. Reichl, W. Wegscheider, T. Ihn, K. Ensslin, and A. Wallraff, "Strong coupling cavity QED with gate-defined double quantum dots enabled by a high impedance resonator," Physical Review X **7**, 011030 (2017).

[334] S. Bosco, D. P. Divincenzo, and D. J. Reilly, "Transmission Lines and Metamaterials Based on Quantum Hall Plasmonics," Physical Review Applied **12**, 014030 (2019).

[335] C. A. Regal, J. D. Teufel, and K. W. Lehnert, "Measuring nanomechanical motion with a microwave cavity interferometer," Nature Physics **4**, 555–560 (2008).

[336] A. A. Clerk, "Quantum noise and quantum measurement," in *Quantum Machines: Measurement and Control of Engineered Quantum Systems*, edited by M. Devoret, B. Huard, R. Schoelkopf, and L. F. Cugliandolo (Oxford University Press, 2014).

[337] J. Bylander, S. Gustavsson, F. Yan, F. Yoshihara, K. Harrabi, G. Fitch, D. G. Cory, Y. Nakamura, J. S. Tsai, and W. D. Oliver, "Noise spectroscopy through dynamical decoupling with a superconducting flux qubit," Nature Physics **7**, 565–570 (2011).

[338] J. Gambetta, W. A. Braff, A. Wallraff, S. M. Girvin, and R. J. Schoelkopf, "Protocols for optimal readout of qubits using a continuous quantum nondemolition measurement," Physical Review A **76**, 012325 (2007).

[339] S. Touzard, A. Kou, N. E. Frattini, V. V. Sivak, S. Puri, A. Grimm, L. Frunzio, S. Shankar, and M. H. Devoret, "Gated Conditional Displacement Readout of Superconducting Qubits," Physical Review Letters **122**, 80502 (2019).

[340] M. J. Feldman, P. T. Parrish, and R. Y. Chiao, "Parametric amplification by unbiased Josephson junctions," Journal of Applied Physics **46**, 4031–4042 (1975).